

# Charmonium and bottomonium in heavy-ion collisions

R. Rapp,<sup>1</sup> D. Blaschke<sup>2,3</sup> and P. Crochet<sup>4</sup>

<sup>1</sup>Cyclotron Institute and Department of Physics & Astronomy  
Texas A&M University, College Station, Texas 77843-3366, USA

Email: rapp@comp.tamu.edu

<sup>2</sup>Institute of Theoretical Physics, University of Wrocław  
Max Born pl. 9, 50-204 Wrocław, Poland

Email: blaschke@ift.uni.wroc.pl

<sup>3</sup>Bogoliubov Laboratory of Theoretical Physics  
JINR Dubna, 141980 Dubna, Russia

<sup>4</sup>Clermont Université, Université Blaise Pascal  
CNRS/IN2P3, LPC, BP 10448, F-63000 Clermont-Ferrand, France

Email: crochet@clermont.in2p3.fr

July 20, 2010

## Abstract

We review the present status in the theoretical and phenomenological understanding of charmonium and bottomonium production in heavy-ion collisions. We start by recapitulating the basic notion of “anomalous quarkonium suppression” in heavy-ion collisions and its recent amendments involving regeneration reactions. We then survey in some detail concepts and ingredients needed for a comprehensive approach to utilize heavy quarkonia as a probe of hot and dense matter. The theoretical discussion encompasses recent lattice QCD computations of quarkonium properties in the Quark-Gluon Plasma, their interpretations using effective potential models, inelastic rate calculations and insights from analyses of electromagnetic plasmas. We illustrate the powerful techniques of thermodynamic Green functions ( $T$ -matrices) to provide a general framework for implementing microscopic properties of heavy quarkonia into a kinetic theory of suppression and regeneration reactions. The theoretical concepts are tested in applications to heavy-ion reactions at SPS, RHIC and LHC. We outline perspectives for future experiments on charmonium and bottomonium production in heavy-ion collisions over a large range in energy (FAIR, RHIC-II and LHC). These are expected to provide key insights into hadronic matter under extreme conditions using quarkonium observables.

# Contents

<b>1</b>	<b>Introduction</b>	<b>2</b>
<b>2</b>	<b>Equilibrium Properties</b>	<b>8</b>
2.1	Correlation and Spectral Functions from Lattice QCD . . . . .	9
2.2	Potential Models in the QGP . . . . .	14
2.3	Quarkonium Dissociation Reactions in the QGP . . . . .	21
2.4	Quarkonium Dissociation in Hadronic Matter . . . . .	27
2.5	Insights from Plasma Physics . . . . .	30
<b>3</b>	<b>Quarkonia in Heavy-Ion Collisions</b>	<b>38</b>
3.1	Charmonium Transport . . . . .	38
3.2	Nuclear Absorption and Initial-State Effects . . . . .	42
3.3	Applications at SPS, RHIC and LHC . . . . .	47
3.3.1	Centrality Dependence . . . . .	48
3.3.2	Transverse-Momentum Spectra and Elliptic Flow . . . . .	53
3.3.3	Rapidity Distributions . . . . .	55
3.3.4	Excitation Function . . . . .	56
3.3.5	Excited Charmonia . . . . .	57
3.3.6	Bottomonia . . . . .	58
<b>4</b>	<b>Future experiments</b>	<b>60</b>
4.1	Quarkonia in heavy-ion collisions at the RHIC-II . . . . .	61
4.1.1	Experimental conditions . . . . .	62
4.1.2	The PHENIX experiment . . . . .	62
4.1.3	The STAR experiment . . . . .	63
4.2	Quarkonia in heavy ion collisions at the LHC . . . . .	64
4.2.1	Experimental conditions . . . . .	65
4.2.2	The ALICE experiment . . . . .	65
4.2.3	The CMS experiment . . . . .	66
4.2.4	The ATLAS experiment . . . . .	68
4.3	Quarkonia in heavy-ion collisions at the SIS-300 . . . . .	68
4.3.1	Experimental conditions . . . . .	69
4.3.2	The CBM experiment . . . . .	69
<b>5</b>	<b>Summary</b>	<b>70</b>

# 1 Introduction

The properties of heavy quarkonium states (charmonium and bottomonium) in a hot and dense QCD<sup>1</sup> medium have been intensely studied for over 20 years now, both experimentally and theoretically. Current and upcoming heavy-ion collision experiments at the Relativistic Heavy-Ion Collider (RHIC, at Brookhaven National Laboratory (BNL) in New York), at the Large Hadron Collider (LHC, at the European Organization for Nuclear Research (CERN) in Geneva) and at the Facility for Antiproton and Ion Research (FAIR, at the Helmholtz Center for Heavy-Ion Research (GSI) in Darmstadt) put a large emphasis on heavy quarkonium programs in their campaigns. The interest in heavy quarkonia in medium is motivated by their unique role in the diagnostics of the highly excited medium created in ultrarelativistic heavy-ion collisions (URHICs). Early on,  $J/\psi$  suppression in URHICs was suggested as a signal of the formation of a Quark-Gluon Plasma (QGP) [1]. This idea was instrumental in triggering a corresponding experimental program at the CERN-SPS. The experimental results have been accompanied and pushed forward by a broad spectrum of theoretical work (see, e.g., Refs. [2, 3, 4, 5] for various reviews). After many years of analysis and interpretation of the SPS data [6], with a first round of RHIC results completed and with new insights from the theoretical side (including thermal lattice QCD, effective models and phenomenology), it is timely to assess the current state of affairs to help facilitate the next stage of developments. In the remainder of this introduction we will give an initial view of the physics of quarkonia in a hot and dense medium, illustrating some of the difficulties in the interpretation of (charmomium) observables in URHICs at SPS and RHIC.

As a starting point, we collect in Tabs. 1 and 2 basic properties of the bound-state spectrum of a heavy quark ( $Q=c,b$ ) and its antiquark ( $\bar{Q}$ ) in the vacuum (note that the lifetime of the top quark is too short to allow for developing a  $t\bar{t}$  bound-state spectrum). These spectra can be well understood in terms of a potential-model approach, where the underlying potential is of the so-called Cornell-type [8],

$$V_{Q\bar{Q}}(r) = -\frac{4}{3}\frac{\alpha_s}{r} + \sigma r, \quad (1)$$

consisting of a (color-) Coulomb term dominant at small  $Q$ - $\bar{Q}$  separation,  $r$ , and a linearly rising

---

<sup>1</sup>Quantum Chromodynamics, the theory of the strong force and part of the Standard Model of elementary particle physics.

State ( $nL$ )	$J^{PC}$	$m_\Psi$ [MeV]	$\Gamma_{tot}$ [MeV]	$m_\Psi - 2m_D$ [MeV]
$\eta_c$ ( $1S$ )	$0^{-+}$	$2980 \pm 1$	$27 \pm 3$	-750
$J/\psi$ ( $1S$ )	$1^{--}$	3097	$0.093 \pm 0.002$	-633
$\chi_{c0}$ ( $1P$ )	$0^{++}$	3415	$10.2 \pm 0.7$	-315
$\chi_{c1}$ ( $1P$ )	$1^{++}$	3511	$0.89 \pm 0.05$	-219
$h_c$ ( $1P$ )	$1^{+-}$	3526	$< 1$	-204
$\chi_{c2}$ ( $1P$ )	$2^{++}$	3556	$2.03 \pm 0.12$	-174
$\eta'_c$ ( $2S$ )	$0^{-+}$	$3637 \pm 4$	$14 \pm 7$	-92
$\psi'$ ( $2S$ )	$1^{--}$	3686	$0.32 \pm 0.01$	-44
$\psi''$ ( $3S$ )	$1^{--}$	$3773 \pm 3$	$27.3 \pm 1$	+43

Table 1: Selected properties of  $c\bar{c}$  mesons (generically referred to as  $\Psi$ ) in the vacuum, as extracted from the recent review of particle physics [7]. The particle name in the first column is supplemented by a nonrelativistic classification of principal quantum number ( $n$ ) and orbital angular momentum ( $L$ ), the second column gives the total spin, parity and charge-conjugation quantum numbers, the third column the meson's mass (errors below 1 MeV are not quoted), the fourth column the total decay width, and the last column the mass difference to the open-charm threshold (taken as  $2m_{D^0} \simeq 3730$  MeV).

State ( $nL$ )	$J^{PC}$	$m_\Psi$ [MeV]	$\Gamma_{tot}$ [MeV]	$m_\Psi - 2m_B$ [MeV]
$\Upsilon$ ( $1S$ )	$1^{--}$	9460	$0.054 \pm 0.001$	-1100
$\chi_{b0}$ ( $1P$ )	$0^{++}$	9859	?	-700
$\chi_{b1}$ ( $1P$ )	$1^{++}$	9893	?	-665
$\chi_{b2}$ ( $1P$ )	$2^{++}$	9912	?	-645
$\Upsilon'$ ( $2S$ )	$1^{--}$	10023	$0.032 \pm 0.003$	-535
$\chi_{b0}$ ( $2P$ )	$0^{++}$	10233	?	-325
$\chi_{b1}$ ( $2P$ )	$1^{++}$	10255	?	-305
$\chi_{b2}$ ( $2P$ )	$2^{++}$	10269	?	-290
$\Upsilon''$ ( $3S$ )	$1^{--}$	10355	$0.020 \pm 0.002$	-205
$\Upsilon'''$ ( $4S$ )	$1^{--}$	$10579 \pm 1$	$20.5 \pm 2.5$	+20

Table 2: Same as Table 1, but for low-lying  $b\bar{b}$  mesons (generically referred to as  $\Upsilon$ ) and an open-bottom threshold of  $2m_{B^\pm} \simeq 10558$  MeV (mass differences have been rounded to steps in 5 MeV).

(“confining”) term at large  $r$ . The potential description is now understood as a low-energy effective theory of Quantum Chromodynamics (QCD) utilizing an expansion in the inverse heavy-quark mass ( $1/m_Q$ ) [10, 9]. Moreover, the pertinent vacuum potential has been computed in lattice QCD [11] and found to agree well with the phenomenological Cornell potential as deduced from applications to quarkonium spectroscopy.

The good understanding of the vacuum properties of heavy quarkonia in a relatively simple framework is one of the reasons why they are believed to be a good probe of medium effects. The latter can be roughly categorized into screening effects in the two-body potential and dissociation reactions with constituents of the heat bath. Since the heavy-quark mass is large compared to the typical temperatures realized in a heavy-ion reaction, a further practical benefit emerges: heavy-quark production is believed to be largely restricted to the earliest phase of the collision, i.e., in primordial “hard” (high-momentum transfer) collisions of the incoming nucleons. On the one hand, this implies a separation of the (hard) production process from the subsequent (soft) medium effects, and, on the other hand, it provides a baseline to determine the initial abundance prior to the formation of the medium. For total charm production, this picture is consistent with current experimental information [12, 13] and also supported by theoretical estimates [14].

The above setup defines the basic framework to analyze modifications in the production of heavy quarkonia in URHICs, due to final-state interactions induced by the surrounding hot/dense medium. The first and most widely discussed probe in this context is the  $J/\psi$ . Somewhat contrary to the expectations at the time, which considered the *production* of charmonium as a primordial plasma probe [15, 16], the suggestion by Matsui and Satz [1] asserted that with increasing centrality in URHICs a suppression of the  $J/\psi$  peak in the dimuon invariant-mass spectrum should occur. As a suitable reference Drell-Yan dileptons at high mass were suggested, as a well-established “hard” process. The underlying mechanism for the dissociation of the charmonium bound-state in a dense medium was associated with the “Debye screening” of the binding potential, largely driven by a deconfinement of color charges and thus intimately connected to the formation of a QGP. This phenomenon is rather general, very similar to the dissolution of atomic bound states in electromagnetic plasmas, or to the Mott transition in semiconductors [17, 18] where under high pressure electrons become delocalized and a conduction band emerges, signaling the plasma state.

Shortly after the prediction of  $J/\psi$  suppression, the NA38 experiment at the CERN-SPS found evidence for this effect in collisions of 200 AGeV oxygen (O) projectiles with uranium (U) nuclei [19], see Fig. 1. The interpretation of this observation in terms of QGP formation was immediately challenged by

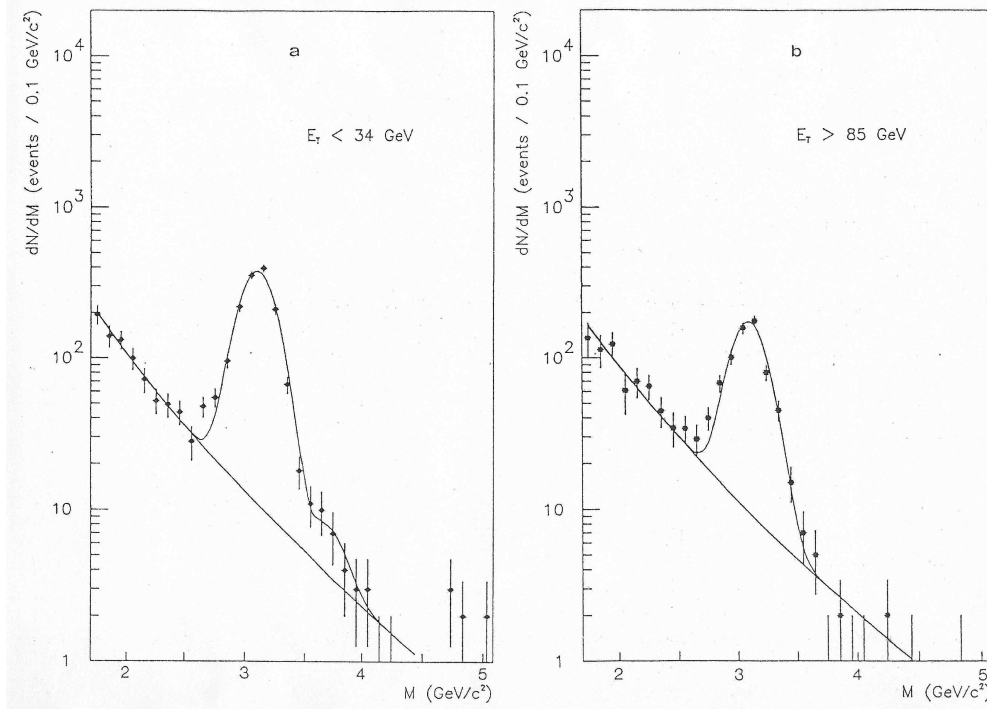


Figure 1: First observation of the  $J/\psi$  suppression effect in O(200 AGeV)-U collisions in the NA38 experiment at CERN-SPS. When comparing the invariant-mass spectrum of muon pairs produced in peripheral collisions (characterized by a small transverse energy,  $E_T < 34$  GeV; left panel) with that in central collisions (at high transverse energy,  $E_T > 85$  GeV; right panel), a reduction of the  $J/\psi$  signal relative to the Drell-Yan continuum is apparent (figures from Ref. [19]).

more conventional explanations in terms of inelastic  $J/\psi$  scattering on “primordial” target and projectile nucleons [20], and/or on secondary produced hadronic “comovers” [21, 22]. The systematic experimental analysis of the nuclear mass-number dependence of  $J/\psi$  production in proton-nucleus ( $p$ - $A$ ) collisions at CERN (NA3 [23], NA38 [19, 24]) and FNAL (E772 [25]), as well as in collision systems with light-ion projectiles (O-U, S-U, O-Cu) at CERN (NA38 [26]), indeed suggests that the  $J/\psi$  suppression in all these experiments can be understood in a unified way by primordial “nuclear absorption” of the charmonium state (with no further reinteractions before being detected via its dimuon decay). The magnitude of this suppression has been characterized by an empirical mean path length,  $L$ , of the charmonium traveling through cold nuclear matter at normal density,  $n_0 = 0.16 \text{ fm}^{-3}$ . The suppression systematics could then be quantitatively described following the simple absorption law,  $S_{\text{nuc}} = \exp(-\sigma_{\text{abs}} n_0 L)$  [27], with the nuclear absorption cross section  $\sigma_{\text{abs}}$  extracted from  $p$ - $A$  collisions<sup>2</sup>. In fact, nuclear absorption systematics could not only account for  $p$ - $A$  but also for  $A$ - $B$  collision systems, see Fig. 2, where  $L = L_A + L_B$  is a schematic measure for the combined path length through projectile and target nuclei. The QGP signal had seemingly vanished [27]!

The situation changed when the Pb beam became available at the SPS. In central Pb(158 AGeV)-Pb collisions the successor experiment of NA38, NA50, found a stronger  $J/\psi$  suppression than predicted by the extrapolation of the nuclear absorption law (based on the Glauber model) [28, 29], see Fig. 3. This deviation was dubbed “anomalous  $J/\psi$  suppression”, as opposed to the “normal suppression” caused by nuclear absorption (following the simple exponential dependence on the  $L$ -variable). A first interpretation of the anomalous suppression as a signal for QGP formation was given by Blaizot and

<sup>2</sup>A more detailed account underlying such analysis, based on the Glauber model including realistic nuclear density profiles, will be given in Sec. 3.2 of the main text.

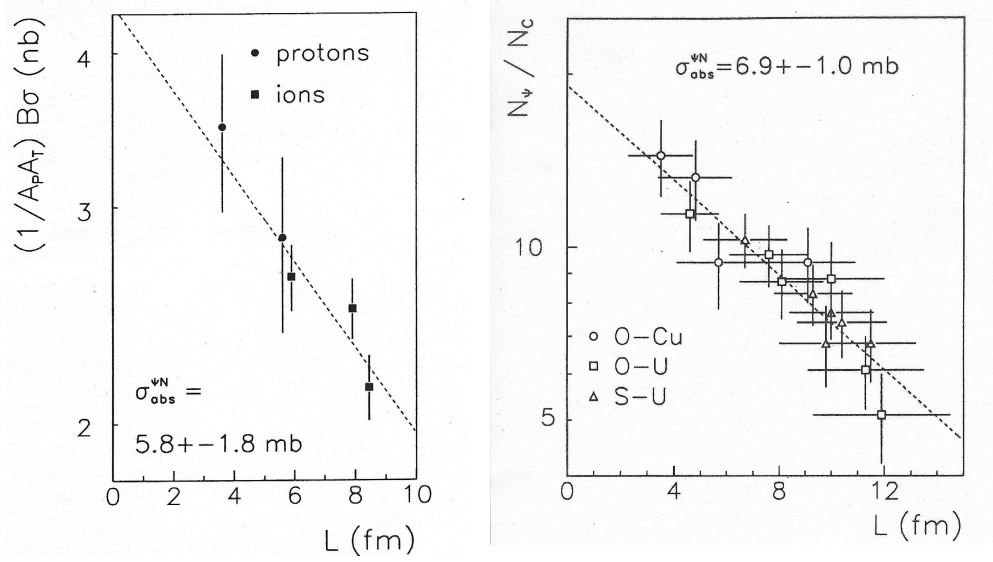


Figure 2: Early comparisons of nuclear-absorption calculations for  $J/\psi$  suppression to data in  $p$ - $A$  and  $A$ - $B$  collisions with light-ion projectiles [27]. Recent data and analyses are discussed in the main text.

Ollitrault [30] within a “threshold-suppression” scenario. It was assumed that a charm-anticharm quark pair cannot hadronize into a charmonium state when it is produced in a region where the transverse density of participant nucleons exceeds a certain “critical” value,  $n_p^{\text{crit}}$ , see Fig. 4. This scenario provided a consistent explanation of the available data in the sense that the value for  $n_p^{\text{crit}}$  (characterizing the maximal energy density of the subsequently formed medium) required to describe the suppression in Pb-Pb was larger than the maximum value  $n_p$  reached with light-ion projectiles (see also Ref. [31]).

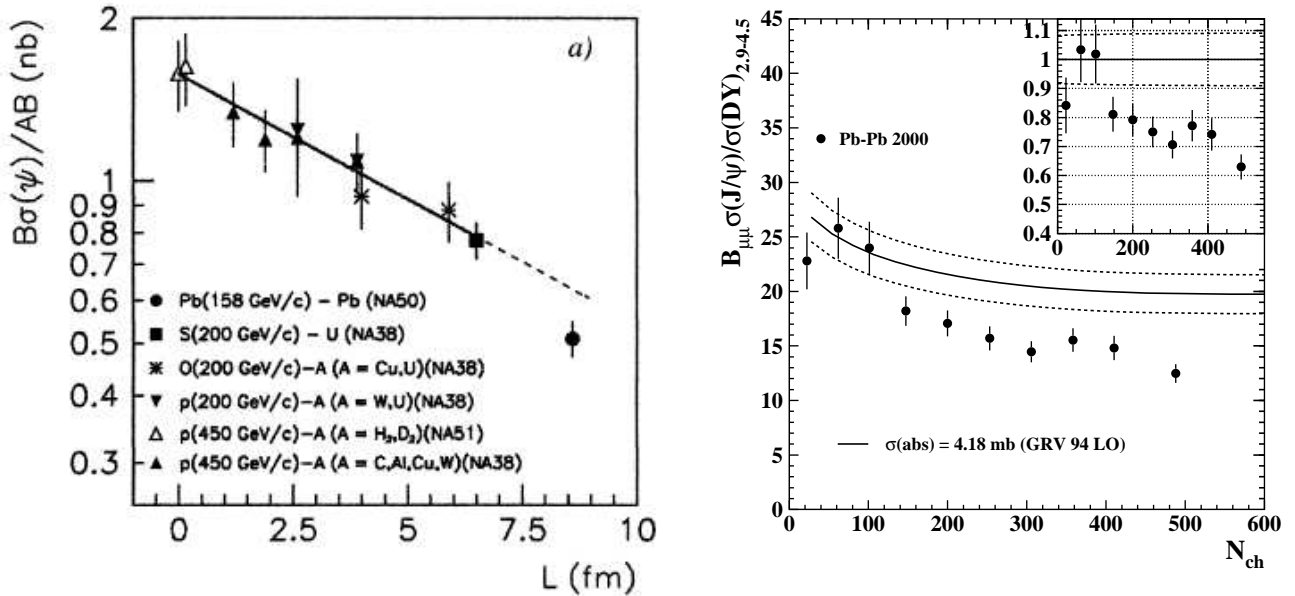


Figure 3: Anomalous  $J/\psi$  suppression in Pb(158 AGeV)-Pb collisions at the CERN-SPS measured by the NA50 experiment as a function of the Glauber variable  $L$  (left panel, from Ref. [28]) and as a function of the number of charged particles  $N_{ch}$  (right panel, from Ref. [32]).

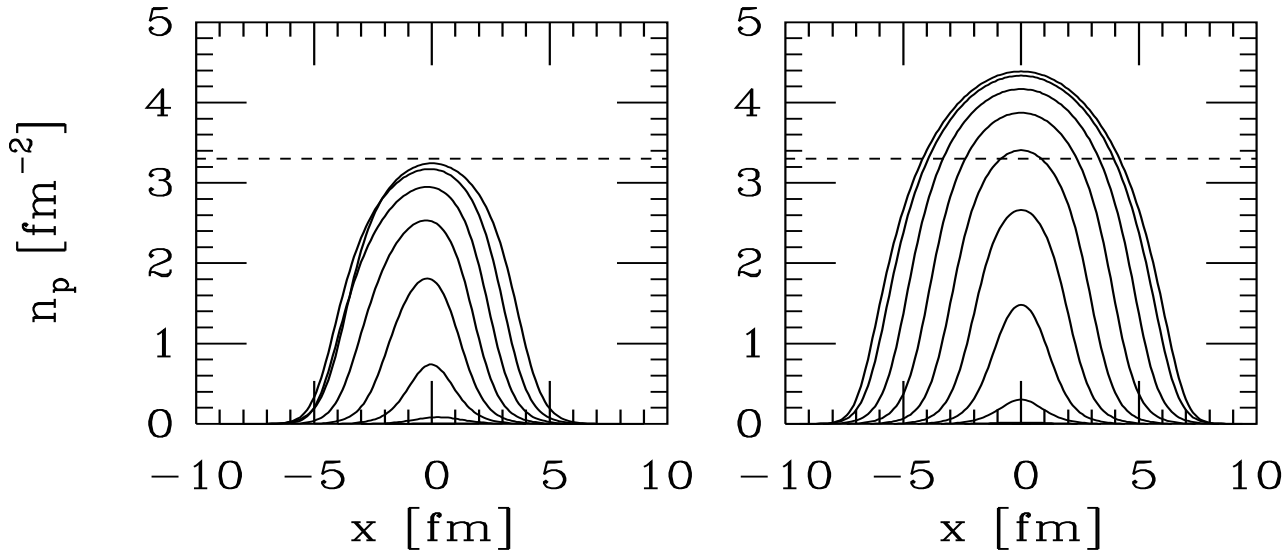


Figure 4: The transverse density of participants,  $n_p$ , in S-U (left) and Pb-Pb (right) collisions along the direction of the impact parameter vector,  $\vec{b}$ , for different values of  $b = 0, 2, 4, \dots$  fm. The dashed line indicates the adopted threshold value  $n_p^{\text{crit}} = 3.3 \text{ fm}^{-2}$  for the onset of anomalous  $J/\psi$  suppression. Figure taken from Ref. [30].

This initial interpretation was followed by a wide variety of theoretical investigations including hadronic comover dissociation, parton-induced break-up reactions in the QGP, pre-equilibrium effects, and combinations thereof. The NA50 collaboration was led to conclude that the  $J/\psi$  suppression pattern provides evidence for the deconfinement of quarks and gluons [35]<sup>3</sup>. One of the controversially discussed issues was (and still is) whether the data provide evidence for a “threshold” or “onset” behavior in terms of step-like patterns in the centrality dependence. Further clarification was hoped to be gained from studying intermediate size collision systems, as recently done by the NA60 collaboration [33, 34]. In In(158 AGeV)-In collisions, the “onset” of anomalous  $J/\psi$  suppression does not seem to follow a scaling with the Glauber variable  $L$ , but rather with the number of participants,  $N_{\text{part}}$ , in the collision. Note that  $N_{\text{part}}$ , contrary to  $L$ , is a quantity closely related to the density of secondary particles, potentially forming a QGP, see Fig. 5.

In the year 2000 the experimental program at RHIC commenced. First  $J/\psi$  data for Au-Au collisions became available in 2003 [36], while recent ones may be found in Ref. [37]. Figure 6 shows the experimental data for  $J/\psi$  production in terms of the so-called nuclear modification factor,  $R_{AA}$ , as a function of centrality. It is defined as the yield observed in heavy-ion reactions relative to the one in  $p$ - $p$  collisions scaled by the number,  $N_{\text{coll}}$ , of binary  $N$ - $N$  collisions,

$$R_{AA}(N_{\text{part}}) = \frac{N_{AA}^{J/\psi}}{\langle N_{\text{coll}} \rangle N_{pp}^{J/\psi}}. \quad (2)$$

In the absence of medium effects one expects  $R_{AA}=1$ . An anomalous suppression of charmonium production was confirmed in semi-/central Au-Au collisions, with a magnitude similar to the one observed at the SPS. This seems rather surprising in view of the factor of 10 higher collision energy at RHIC, inducing higher (initial) energy densities. However, it had been predicted [41, 42, 43, 44] that at RHIC and LHC the copious production of open charm leads to an additional source of  $J/\psi$  production, through the recombination of charm quarks (or charmed mesons) in the hot and dense medium. Calculations

<sup>3</sup>For the final NA50 results concerning  $J/\psi$  suppression, see Ref. [32].

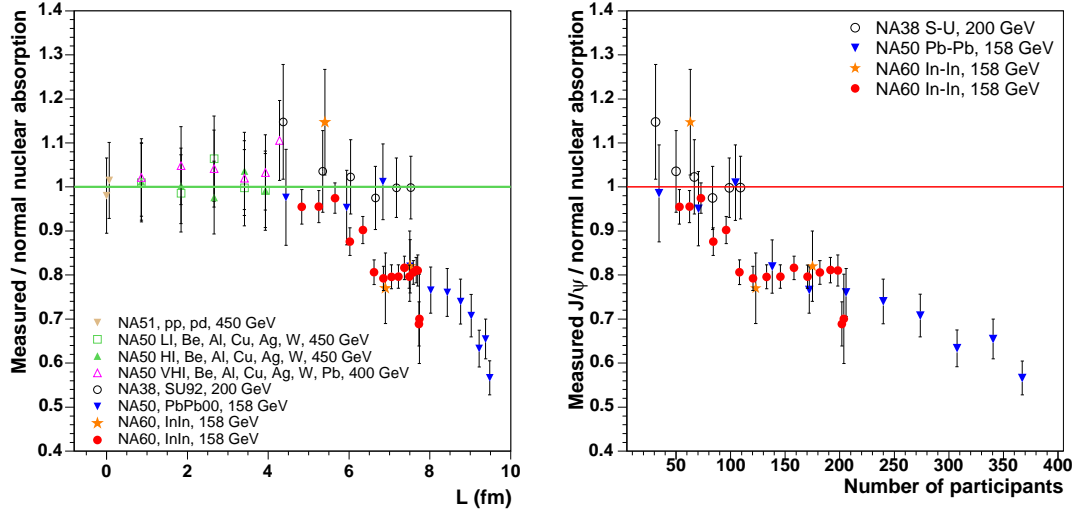


Figure 5: “Anomalous”  $J/\psi$  production (i.e., relative to expectations from normal nuclear absorption) in In(158 AGeV)-In collisions measured by the NA60 experiment compared to other projectile-target combinations at the CERN-SPS. The “threshold” for anomalous suppression appears to scale with the number of participants (right panel) rather than with the Glauber variable  $L$  (left panel); figures taken from Ref. [33].

including both suppression and regeneration mechanisms [44] had anticipated that a stronger “anomalous” suppression is largely compensated by secondary production via charm-anticharm coalescence. This is illustrated in the left panel of Fig. 6 where a comparison with reaction kinetic models for  $J/\psi$  production [38, 39] shows that a naïve extrapolation of “anomalous”  $J/\psi$  suppression in a QGP environment from SPS to RHIC fails. Additional support for a secondary component of the  $J/\psi$  yield at RHIC follows from the observation that  $J/\psi$  suppression is less pronounced at central rapidity relative to forward rapidity, since at central rapidity the regeneration effect should be larger due to a larger charm content in the medium. On the contrary, dissociation mechanisms should increase the suppression due to larger energy densities at midrapidity.

The above discussion has given a first indication of the complexity in describing and understanding the various facets figuring into quarkonium observables in heavy-ion collisions, let alone their interpretation in terms of properties of the Quark-Gluon Plasma. It is thus mandatory to identify key concepts and combine them into a comprehensive approach that allows for a systematic interpretation of experimental data under a broad range of conditions (encompassing, e.g., all available collision energies, from FAIR via SPS and RHIC to LHC). This will be the main objective of this article, by means of a critical review of existing approaches and their comparison to data. An essential ingredient to such approaches are controlled reference points, e.g., equilibrium limits for in-medium properties, or  $p$ -A collisions to separate “normal” nuclear effects from hot/dense matter effects. Our article is roughly organized according to the following decomposition of the problem:

- (1) **Equilibrium properties of quarkonia** (Sec. 2): these provide the main link between properties of the QGP and the medium created in heavy-ion collisions. The basic quantity to be determined is the thermodynamic quarkonium spectral function: its pole mass (binding energy) largely determines the equilibrium abundance (in connections with the properties of open charm/bottom), while in-/elastic reaction rates determine thermal and chemical relaxation times and are encoded in the spectral widths.
- (2) **Quarkonium transport** (Sec. 3.1), which is required to evaluate the coupling of the quarkonia to the medium by computing the evolution of their phase space distribution, starting from realistic initial conditions. In principle, this evolution progresses toward equilibration, e.g., as a function of trans-

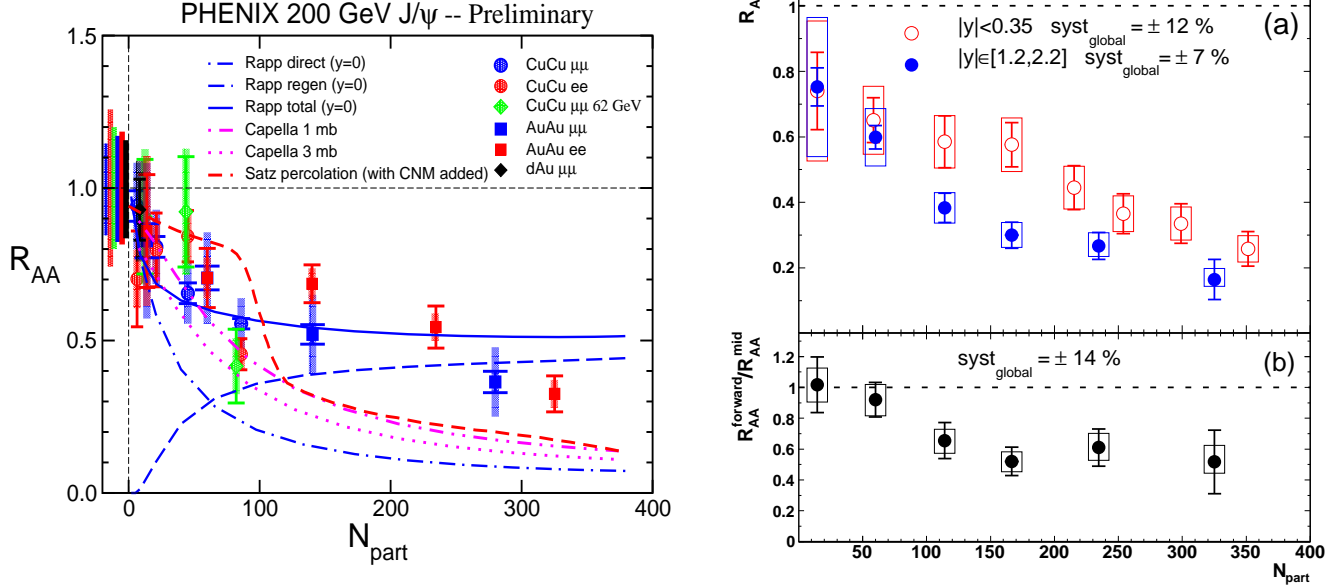


Figure 6:  $J/\psi$  production, relative to the binary-collision scaled yield in  $p$ - $p$  collisions, measured in the PHENIX experiment in  $\sqrt{s_{NN}} = 200$  GeV Au-Au collisions at RHIC. Left panel: comparison with kinetic models [38, 39] of charmonium production at central rapidity, illustrating the importance of secondary  $J/\psi$  production via charm-anticharm recombination (figure from Ref. [40]). Right panel: increase of  $J/\psi$  suppression at forward relative to central rapidity, suggestive for regeneration mechanisms (from Ref. [37]).

verse momentum. The method of choice is a transport treatment incorporating regeneration reactions to enable a relaxation toward thermal and chemical equilibrium. Since regeneration processes involve open-charm/-bottom spectra, a reliable assessment of the latter becomes mandatory.

(3) **Initial spectra and pre-equilibrium interactions** (Sec. 3.2): these determine the initial condition of the transport equation in item (i); they include modifications relative to spectra in  $p$ - $p$  collisions ( $p_T$  broadening via Cronin effect, shadowing), as well as absorption and rescattering on primordial nucleons and secondary particles in the pre-equilibrium evolution of the medium.

(4) **Observables** (Sec. 3.3): these need to be computed by combining all of the above. An additional input is a realistic modeling of the bulk medium evolution, ideally in terms of a locally thermalized medium (if applicable), e.g., within a hydrodynamic evolution, or in terms of transport models in regimes of incomplete thermalization.

In Sec. 4 we give an outlook on the capabilities of, and physics questions to be addressed with, future experiments at LHC, RHIC-II and FAIR, while Sec. 5 contains a brief summary.

## 2 Equilibrium Properties

As emphasized in the Introduction, the basic quantity encoding the equilibrium properties of a quarkonium state of given quantum number  $\alpha$ , is its spectral function,  $\rho_\alpha$ . Roughly speaking,  $\rho_\alpha(\omega)$  characterizes the spectral distribution of strength as a function of energy,  $\omega$ . Bound or resonance states manifest themselves as peaks with well defined mass,  $m_\alpha$ , and spectral width,  $\Gamma_\alpha$  (in principle, more than one state is possible for a given  $\alpha$ , e.g., in vacuum  $J/\psi$ ,  $\psi'$  etc. for  $J^{PC} = 1^{--}$ , recall Tab. 1). Note, however, that in the context of charmonium production in heavy-ion collisions, it is unlikely that spectral modifications can be directly detected in the dilepton invariant-mass spectrum of (vector-meson)

quarkonium decays<sup>4</sup>. Thus, relevant connections of the in-medium spectral properties of quarkonia to URHIC phenomenology are: (a) their masses,  $m_\Psi$ , which determine the equilibrium abundances, (b) their inelastic widths,  $\Gamma_\Psi^{\text{inel}}$ , which determine formation and destruction rates (or chemical equilibration times), (c) their dissolution temperatures,  $T_\Psi^{\text{diss}}$ , which determine the absence of formation processes for  $T > T_\Psi^{\text{diss}}$ , and, (d) their elastic widths,  $\Gamma_\Psi^{\text{el}}$ , which affect momentum spectra (and determine the kinetic equilibration times).

First-principle information on quarkonium properties can be obtained from numerical lattice-discretized computations in QCD at finite temperature. We start our discussion from this perspective by reviewing the current status of this approach in Sec. 2.1. As we will see, lattice-QCD (lQCD) simulations do not directly provide the physical spectral function, nor do they readily allow for insights into the mechanisms underlying “observable” medium effects. Effective models thus play an important role in the interpretation of lQCD results, as well as in furnishing quantitative input for applications in heavy-ion reactions. A natural starting point is the extension of the potential model, which works well for quarkonium spectroscopy in vacuum, to finite temperatures; this is discussed in Sec. 2.2, with emphasis on recent developments incorporating information and constraints from lQCD. Potential models are typically used to assess how medium effects in the 2-body interaction affect the bound-state spectrum (i.e., the location of the peaks in the spectral function). The thermodynamic  $T$ -matrix approach enables to assess both bound and continuum states. Of equal importance for phenomenological applications is the determination of inelastic reaction rates, both in the QGP and hadron gas (HG), which is elaborated in Secs. 2.3 and 2.4, respectively. The problem of in-medium quarkonia shares several features with the well-studied fermionic two-body problem in electromagnetic plasmas. Techniques developed for the latter may thus provide useful insights which we attempt to exhibit in Sec. 2.5. Regarding notation, we adopt 3 variants of the single heavy-quark (HQ) mass with the following meaning:  $m_Q^0$ : bare mass,  $m_Q$ : constant effective mass,  $m_Q^*$ : temperature-dependent effective mass.

## 2.1 Correlation and Spectral Functions from Lattice QCD

The properties of the  $Q\bar{Q}$  interaction in a given hadronic (color-singlet) channel with quantum numbers  $\alpha$  are encoded in the two-point correlation function of the pertinent current,  $j_\alpha$ . In coordinate space the correlation function (or correlator) is defined by the amplitude of creating the current at the origin, propagating it to point  $(\tau, \vec{r})$  and absorbing it,

$$G_\alpha(\tau, \vec{r}) = \langle \langle j_\alpha(\tau, \vec{r}) j_\alpha^\dagger(0, \vec{0}) \rangle \rangle . \quad (3)$$

In a heat bath of temperature  $T$  the amplitude corresponds to a thermal average over the partition function of the system. For meson correlators, the QCD currents are given by quark bilinears,  $j_\alpha = \bar{Q}\Gamma_\alpha Q$ , where  $\Gamma_\alpha$  specifies the spin-flavor channel. In momentum space the imaginary part of the (retarded) correlation function,  $G_\alpha^R(\omega, \vec{p})$ , is commonly referred to as the spectral function,

$$\rho_\alpha(\omega, p) = -2 \text{Im} G_\alpha^R(\omega, p) , \quad (4)$$

where  $\omega$  and  $p$  denote the energy and 3-momentum modulus, respectively (in the literature, the spectral function is also denoted by  $\sigma_\alpha = \rho_\alpha/2\pi$ ; to avoid redundancy in notation with the string tension and cross sections, we will not use this notation in the present article). In the timelike regime,  $\omega^2 - p^2 > 0$ ,  $\rho_\alpha$  characterizes the physical excitation spectrum in the channel  $\alpha$ , which, in principle, can be measured in experiment.

---

<sup>4</sup>E.g., the  $J/\psi$  lifetime in free space is  $\tau_{J/\psi}^{\text{vac}} = 1/\Gamma_{J/\psi}^{\text{tot, vac}} \simeq 2000 \text{ fm}/c$ , compared to a typical fireball lifetime of  $\sim 10 \text{ fm}/c$ . This means that the ratio of  $J/\psi$  decays inside to outside the medium is about 1/200. If the average in-medium  $J/\psi$  width is  $\sim 200 \text{ MeV}$ , a detection of this effect would require a mass resolution of about 1 MeV, corresponding to an unrealistic 0.03% at the  $J/\psi$  mass.

In field theory, the implementation of temperature into the partition function involves the transformation of the vacuum transition rate in real time to imaginary time. This amounts to replacing time evolutions with thermal averages. The temporal direction is thereby restricted to the interval  $[0, \beta]$  with the upper limit being identified with the inverse temperature of the system,  $\beta = 1/T$ . The evaluation of thermal expectation values of correlation functions, Eq. (3), is routinely performed in lQCD. At large  $r$ , an exponential decay of the spatial correlator renders the lowest mass state dominant,  $G_\alpha(r) \propto e^{-m_\alpha^{scr} r}$ , which can be used to extract hadronic screening masses,  $m_\alpha^{scr}$ , at finite temperature [45, 46]. For temporal correlators, usually projected onto a fixed 3-momentum,  $G(\tau, p)$ , the limited extent of the  $\tau$  interval renders an extraction of physical ground-state masses much more difficult. For a better comparison of quenched ( $N_f=0$ ) and full ( $N_f=2,3$ ) lattice QCD, it is customary to discuss temperature dependencies in units of  $T_c$  in the respective simulation. This accounts at least qualitatively for the difference in the absolute values of critical temperature by comparing the results at roughly equal parton densities (which is often the relevant quantity in the discussion of medium effects). For example, for  $T_c^{\text{quench}} \simeq 1.5 T_c^{\text{full}}$ , the factor of  $\sim 3$  larger gluon density in quenched QCD is roughly compensated by the extra quarks in  $N_f=3$  QCD. In addition, the quantitative values for the (pseudo-) critical temperatures computed in unquenched lQCD, for a given number of quark flavors, are currently beset with a systematic uncertainty of ca.  $\pm 10\text{-}15\%$  corresponding to  $T_c \simeq 180 \pm 30$  MeV [228] (the uncertainty is smaller in quenched QCD with  $T_c \simeq 270$  MeV).

As mentioned above, the information on the excitation spectrum in a given hadronic channel is encoded in the spectral function. The temporal correlator is related to the spectral function via

$$G_\alpha(\tau, p; T) = \int_0^\infty \frac{d\omega}{2\pi} \rho_\alpha(\omega, p; T) K(\omega, \tau; T) \quad (5)$$

with the finite- $T$  kernel

$$K(\omega, \tau; T) = \frac{\cosh[(\omega(\tau - 1/2T))]}{\sinh[\omega/2T]} . \quad (6)$$

The extraction of the spectral function thus requires an inverse integral transform, which, on a finite number of lattice points, is, in principle, not possible in a unique way. In Ref. [47] it has been suggested to employ the so-called Maximum Entropy Method (MEM) to perform a probabilistic reconstruction of the most likely spectral function. Subsequently, this method has been widely used to extract hadronic spectral functions from lQCD correlators [48, 49, 50, 51, 52]. A few examples in various charmonium channels are collected in Fig. 7. The general picture emerging from these calculations is that the ground state  $S$ -wave charmonia, i.e., the  $\eta_c$  ( $J^P=0^-$ ) and  $J/\psi$  ( $J^P=1^-$ ), are surviving in the QGP up to temperatures of  $\sim 2 T_c$ , while the  $P$ -wave states,  $\chi_c$  ( $J^P=0^+, 1^+, 2^+$ ), dissolve at temperatures slightly above the critical one,  $\sim 1.2 T_c$  or so. The first excited  $S$ -wave state ( $\psi'$ ), cannot be resolved numerically, but presumably dissolves earlier than the stronger bound  $\chi_c$  states, possibly even below  $T_c$ . The  $\psi'$  should therefore be quite sensitive to modifications in the hadronic phase of a heavy-ion collision. Ground-state bottomonia seem to survive to even higher temperatures,  $2.5\text{-}3 T_c$  or more [51, 53].

It is instructive to examine the underlying temporal correlators, examples of which are displayed in Fig. 8 (at vanishing 3-momentum,  $p=0$ ). To facilitate their interpretation, they have been normalized to a so-called reconstructed correlator, which is evaluated with the kernel at temperature  $T$ ,

$$G_{\text{rec}}^\alpha(\tau; T) = \int_0^\infty \frac{d\omega}{2\pi} \rho_\alpha(\omega; T^*) K(\omega, \tau; T) , \quad (7)$$

but employs a spectral function at a low temperature,  $T^*$ , where no significant medium effects are expected. The correlator ratio,

$$R_G^\alpha(\tau, T) = G_\alpha(\tau; T)/G_{\text{rec}}^\alpha(\tau; T) , \quad (8)$$

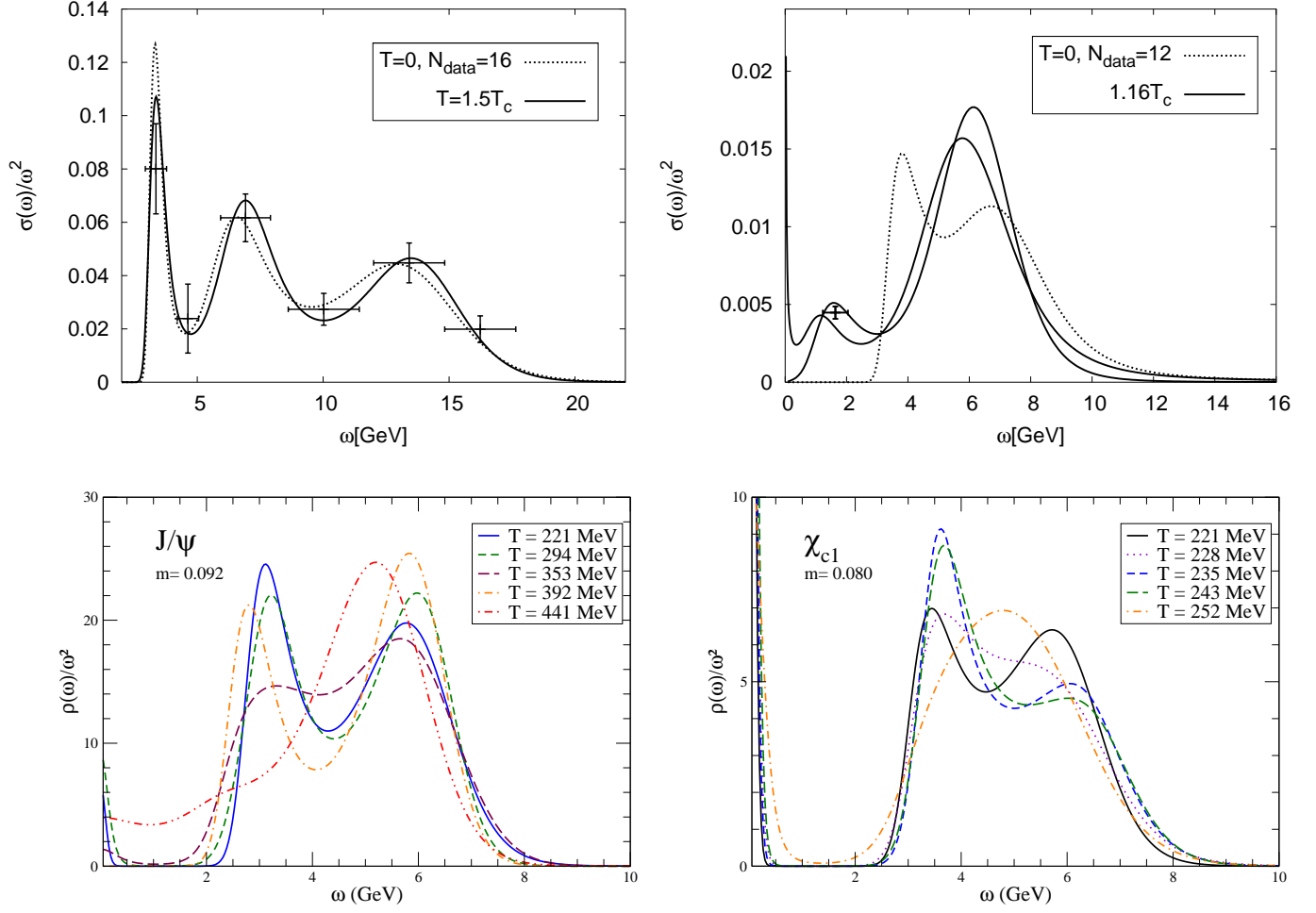


Figure 7: Charmonium spectral functions as a function of energy ( $\omega$ ) and at vanishing 3-momentum ( $p=0$ ) as evaluated from lQCD correlation functions using the maximum entropy method (MEM). Upper panels:  $\eta_c$  (left) and  $\chi_c$  (right) in quenched QCD (with  $T_c=295$  MeV), compared to their vacuum spectral functions (dotted lines) [51]; the  $S$ -wave ( $\eta_c$ ) signal at  $1.5 T_c$  is essentially unmodified compared to the vacuum, while the  $P$ -wave ( $\chi_c$ ) signal at  $1.16 T_c$  is largely distorted (the “data” points in the upper left panel, as well as the two solid lines in the right panel, indicate the uncertainty in the MEM reconstruction procedure). Lower panels:  $J/\psi$  (left) and  $\chi_c$  (right) computed in full QCD for 2 light flavors [52] (the  $y$  scale is in arbitrary units); the critical temperature in these simulations is  $T_c \simeq 210$  MeV (slightly larger than typical values in the range of 160-190 MeV); a  $J/\psi$  signal around  $\omega \simeq 3$  GeV survives up to temperatures of at least 392 MeV  $\simeq 1.9 T_c$  while the  $\chi_c$  peak is essentially smeared out at  $T=252$  MeV  $\simeq 1.2 T_c$  (the quark masses,  $m$ , quoted in the lower panels are unrenormalized input values; after renormalization, they give rise to physical zero-temperature charmonium masses within 10-15 % of the experimental values).

is then an indicator of medium effects in  $G_\alpha(\tau; T)$  through deviations from 1 (note that a normalization to  $G_\alpha(\tau; T^*)$  is not meaningful due to different  $\tau$  ranges for  $T^*$  and  $T$ ). The stability of the temporal correlator ratios, i.e., their small deviations from one, in the vector and pseudoscalar channels has been associated with the survival of the ground-state  $S$ -wave charmonia. The variations for the  $\chi_c$  (which are  $P$  waves) are much larger and set in much closer to  $T_c$  (e.g., up to 40-50% at  $T=1.2 T_c$ ). The opposite trend of the  $J/\psi$  correlators in the upper left and lower left panel could be due to the different vector components considered ( $\sum_{\mu=0-3} G_V^{\mu\mu}$  in the upper panel vs.  $\sum_{i=1-3} G_V^{ii}$  in the lower panel).

Another quantity that can be computed with good accuracy in lQCD, and which encodes information

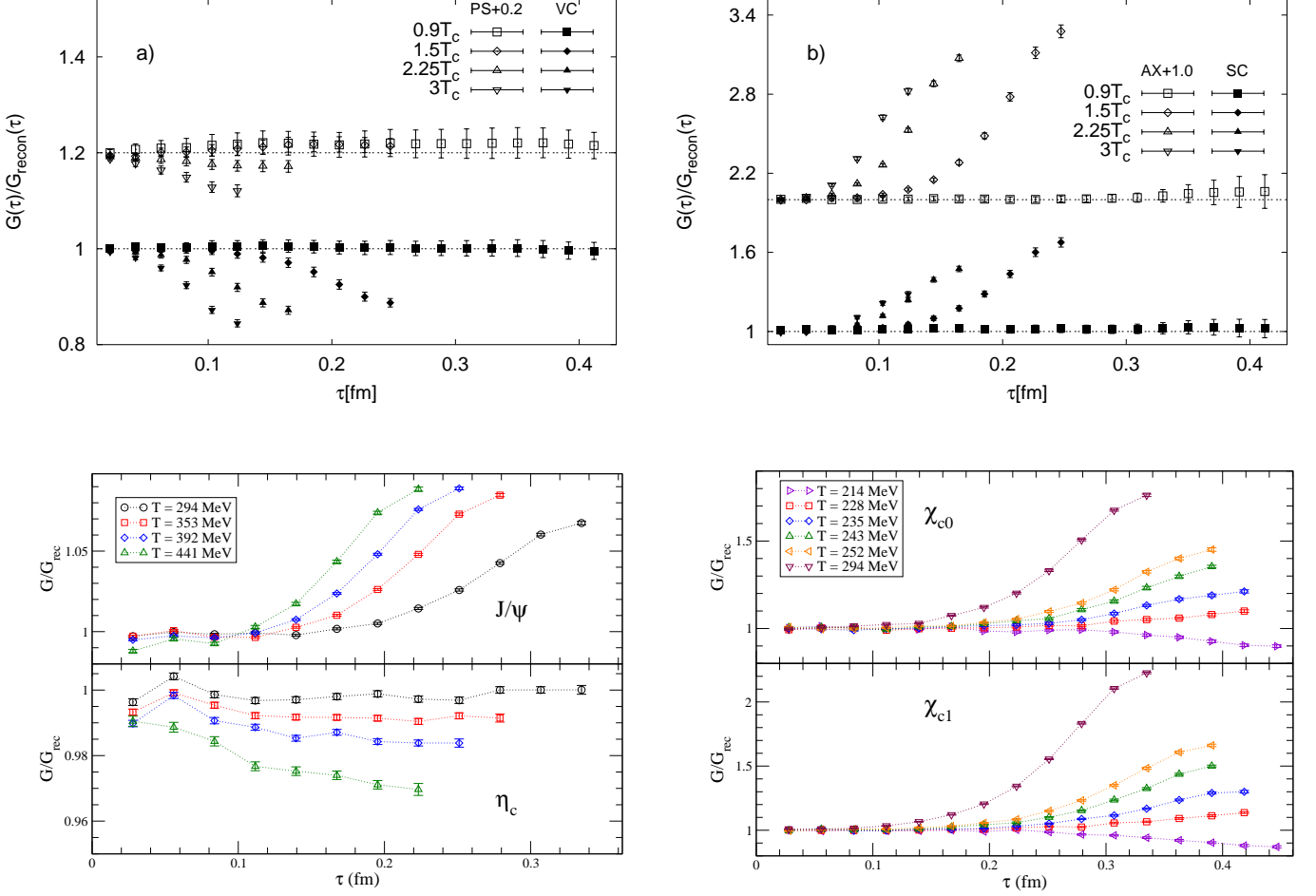


Figure 8: Temporal charmonium correlators at zero 3-momentum computed for  $VC=J/\psi$ ,  $PS=\eta_c$  (left panels) and  $SC=\chi_{c0}$ ,  $AX=\chi_{c1}$  (right panels) in quenched (upper panels) [49] and  $N_f=2$  (lower panels) [52] lattice QCD. The critical temperature in these simulations is  $T_c \simeq 270$  MeV and 210 MeV, respectively. Note the comparatively small variations in the  $S$ -waves (left panels), and the rather large increase in the  $P$ -waves (right panels) indicative for additional low-energy strength relative to the reconstructed correlator. For clarity, the  $PS$  and  $AX$  correlators in the upper panels have been offset by the indicated constant.

about charmonium properties at zero and finite  $T$ , is the free energy,  $F_{Q\bar{Q}}(r)$ , of a static pair of heavy quark and antiquark (more precisely, lQCD obtains  $F_{Q\bar{Q}}(r)$  as the difference between free energies for a thermal system with and without the  $Q\bar{Q}$  pair). In gluo-dynamics the large distance limit of the free energy,  $F_{Q\bar{Q}}^\infty \equiv F_{Q\bar{Q}}(r \rightarrow \infty)$ , can be related to the expectation value of the Polyakov loop [54],

$$e^{-F_{Q\bar{Q}}^\infty/T} = |\langle L \rangle|^2 ; \quad (9)$$

$L$  characterizes a heavy-quark (HQ) source whose expectation value is zero (finite) in the (de-) confined phase, and thus serves as an order parameter of deconfinement. At zero temperature, the free energy computed in the color-singlet channel (which we denote by a superscript “(1)”) closely follows the form expected for a phenomenological Cornell-type potential [10, 9, 11],

$$F_{Q\bar{Q}}^{(1)}(r; T=0) = -\frac{4}{3} \frac{\alpha_s}{r} + \sigma r , \quad (10)$$

recall Eq. (1)<sup>5</sup>. This finding, in connection with the development of HQ effective theories, has confirmed

<sup>5</sup>Strictly speaking, the projection of the color-averaged free energy as computed in lattice QCD, onto color-singlet

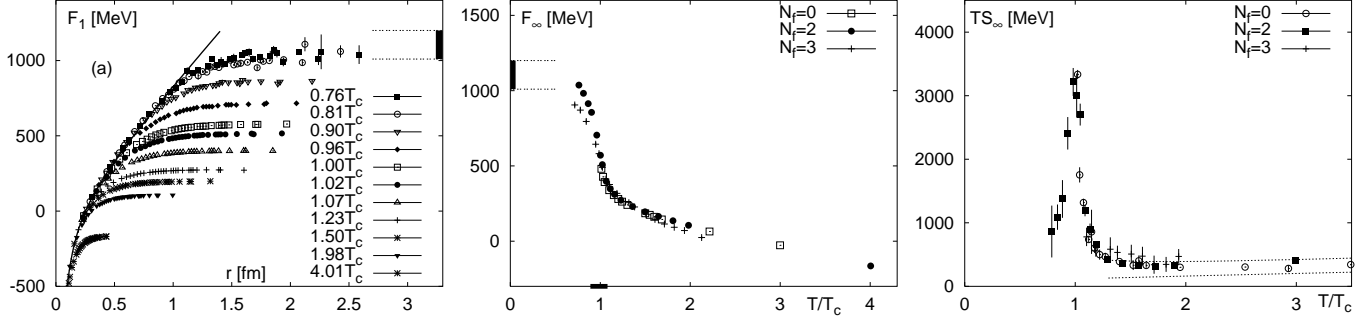


Figure 9: Left panel: free energy of a color-singlet heavy quark-antiquark pair as a function of its size for various temperatures as computed in  $N_f=2$  lattice QCD [11]; the vertical bar in the upper left part indicates the estimated string-breaking energy,  $V_{Q\bar{Q}}^{(1)}(r_{\text{sb}}) \simeq 1.1$  GeV, in vacuum. Middle panel: temperature dependence of the asymptotic value of the color-averaged free energy,  $F_{Q\bar{Q}}^\infty(T)$ , in quenched ( $N_f=0$ ) [56],  $N_f=2$  [11] and  $N_f=3$  [57] lQCD; the pertinent critical temperatures are  $T_c=270$ , 200 and 193 MeV, respectively. Right panel: entropy contribution to the color-averaged free energy at asymptotically large quark-antiquark separation corresponding to the free energies of the middle panel. The band enclosed by the dotted lines for  $T \geq 1.3T_c$  indicates a perturbative estimate of  $TS_{Q\bar{Q}}^\infty(T)$ .

a posteriori the suitability of potential models to quantitatively compute charmonium and bottomonium spectroscopy in free space based on first principles [9]. In the presence of light quarks, string breaking occurs, being characterized by  $F_{Q\bar{Q}}^{(1)}(r; T=0)$  leveling off at a finite value. This may be interpreted as an effective quark (or  $D$ -meson) mass according to  $m_c = m_c^0 + F_{Q\bar{Q}}^{(1),\infty}/2$  (with a bare quark mass of  $m_c^0 \simeq 1.2\text{--}1.3$  GeV). Numerically, with a typical string-breaking separation of  $r_{\text{sb}} \simeq 1.2$  fm, one finds  $F_{Q\bar{Q}}^{(1)}(r_{\text{sb}}; 0) \simeq 1.1$  GeV, which roughly recovers the empirical  $D$ -meson mass. At finite temperature, lQCD computations for  $F_{Q\bar{Q}}^{(1)}(r; T)$  find the expected color-Debye screening, which gradually penetrates to smaller distances as the temperature increases, cf. left panel of Fig. 9. The implications for HQ bound states (or spectral functions) are, however, quite subtle. First, at finite  $T$  the free energy receives an extra contribution due to an entropy term,

$$F_{Q\bar{Q}}(r; T) = U_{Q\bar{Q}}(r; T) - TS_{Q\bar{Q}}(r; T) . \quad (11)$$

It is currently not clear whether the internal energy,  $U_{Q\bar{Q}}(r; T)$ , or the free one,  $F_{Q\bar{Q}}(r; T)$ , is a more appropriate quantity to be identified with a finite-temperature HQ potential. Second, the temperature introduces an extra scale into the problem which needs to be properly implemented into the construction of a HQ effective theory [58, 59]. Third, the presence of the entropy term, which does not vanish at large separation  $r$ , renders the identification of an effective HQ mass more problematic, especially close to  $T_c$ , where  $TS_{Q\bar{Q}}^\infty$  becomes very large, see right panel of Fig. 9. Nevertheless, the application of potential models at finite temperature has provided valuable insights into heavy quarkonium properties at finite  $T$ . In particular, the synthesis of independent information on correlators and free energies from lQCD has enabled interesting insights, as we discuss in the following Section.

---

and -octet channels is not gauge invariant [55]. However, they can be constrained at sufficiently short distances where temperature effects are not operative, or guided by Casimir scaling relations inferred from perturbative QCD.

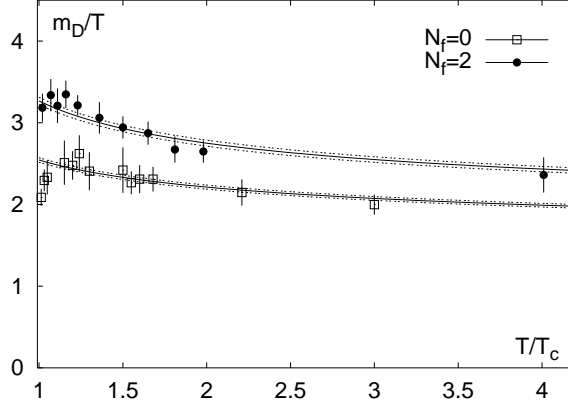


Figure 10: Nonperturbative extraction of the Debye mass ( $m_D \equiv \mu_D$ ) based on exponential fits of a screened Coulombic term to the in-medium color-singlet HQ free energy in  $N_f=2$  (solid circles) [11] and quenched ( $N_f=0$ , open squares) [61] lQCD. The bands are analytic fits using the perturbative form of the Debye mass,  $\mu_D/T = A(1 + N_f/6)^{1/2} g_{2\text{-loop}}$  with a 2-loop finite- $T$  running coupling and a multiplicative constant  $A \simeq 1.5$  to account for nonperturbative effects. Absolute units are obtained by using the pertinent critical temperatures of  $T_c \simeq 200(270)$  MeV for  $N_f=2(0)$ .

## 2.2 Potential Models in the QGP

Early applications [60] of in-medium heavy-quark potentials have employed a phenomenological ansatz to implement color-screening effects in a deconfined plasma into the Cornell potential, Eq. (1), via

$$V_{Q\bar{Q}}(r; T) = \frac{\sigma}{\mu_D(T)} (1 - e^{-\mu_D(T)r}) - \frac{4\alpha_s}{3r} e^{-\mu_D(T)r} . \quad (12)$$

The entire temperature dependence is encoded in the Debye mass,  $\mu_D(T)$  (the vacuum potential is recovered for  $\mu_D \rightarrow 0$ ). Defining the Hamiltonian as

$$\hat{H}(r; T) = 2m_Q - \frac{\vec{\nabla}^2}{m_Q} + V_{Q\bar{Q}}(r; T) , \quad (13)$$

the Schrödinger equation for the bound state problem,

$$\hat{H} \phi_{nl}(r; \mu_D) = \omega_{nl}(\mu_D) \phi_{nl}(r; \mu_D) , \quad (14)$$

has been solved for the eigen-energies,  $\omega_{nl}$ , as a function of the Debye mass. A state  $(n, l)$  was considered to be dissolved at a “critical” Debye mass,  $\mu_D^{\text{diss}}$ , if the “dissociation” energy,

$$\omega_{nl}^{\text{diss}} \equiv 2m_Q + \frac{\sigma}{\mu_D} - \omega_{nl} , \quad (15)$$

reaches zero. Note that the term  $\frac{\sigma}{\mu_D}$  corresponds to the large-separation limit of the in-medium potential, Eq. (12), cf. also the discussion in the text following Eq. (10) in the previous Section. The critical Debye masses for dissolution were found to be  $\mu_D^{\text{diss}}(n=1) \simeq 0.7(1.6)$  GeV for ground state ( $n=1$ ) charmonium (bottomonium), and  $\mu_D^{\text{diss}}(n=2) \simeq 0.35(0.6)$  GeV for the first excited states,  $\psi'$  and  $\chi_c$  ( $\Upsilon'$  and  $\chi_b$ ) [60]. Recent lQCD computations of the in-medium Debye mass based on the Coulombic term in the color-singlet free energy are displayed in Fig. 10 [11]. Comparing these to the values for  $\mu_D^{\text{diss}}$  extracted from the screened Cornell potential, Eq. (12), suggests dissociation temperatures of all charmonia at or slightly above  $T_c$ .

The next step became possible with the availability of quantitative IQCD results for heavy-quark free energies. In Ref. [62], the color-singlet free energy,  $F_{Q\bar{Q}}^{(1)}$  was used in a Schrödinger equation, and  $J/\psi$  dissolution occurred at about  $1.1 T_c$ , while  $\chi_c$  ( $\psi'$ ) were found to melt (well) below  $T_c$ . The recent IQCD spectral function results, indicative for  $J/\psi$  states surviving well above  $T_c$ , appear to challenge this conclusion (recall Fig. 7). In Ref. [63] it has been suggested to employ the internal, rather than the free, energy as an interquark potential. It was argued that  $U_{Q\bar{Q}}$  is the appropriate quantity in the limit where the typical bound state (formation or life) time is much smaller than the typical time for heat exchange with the thermal environment,  $\tau_{\text{bound}} \ll \tau_{\text{heat}}$ . In this case, the entropy term is not active and should be removed from the free energy, leading to the internal energy. While, according to Eq. (11), one has  $U_{Q\bar{Q}} > F_{Q\bar{Q}}$ , the actually used potentials become deeper upon subtraction of the asymptotic values of the internal energy (recall that the force is given by the derivative of the potential). As noted in connection with Fig. 9, the subtraction procedure is problematic in the immediate vicinity of  $T_c$ . This problem is currently the weakest link in converting IQCD results to effective heavy-quark potentials. From a pragmatic point of view, the use of  $U_{Q\bar{Q}}$  in a Schrödinger equation [63, 64, 65] improved the qualitative agreement of the potential approach with the IQCD spectral functions in that  $J/\psi$  bound states are supported up to temperatures of  $\sim 2\text{--}2.5 T_c$ , while the  $\chi_c$  dissolves at around  $1.1\text{--}1.2 T_c$ . In Ref. [66], the internal energies have been implemented into a  $T$ -matrix approach for  $Q\text{--}\bar{Q}$  (and  $q\text{--}\bar{q}$ ) interactions, which has the important advantage over the Schrödinger equation that it provides a unified description of bound and scattering states (i.e., above the nominal  $Q\text{--}\bar{Q}$  threshold). For  $S$ -wave charmonia, it was found that the lowest bound state moves into the continuum at  $\sim 2 T_c$ , after which it rapidly dissolves. However, it was also noted that the extractions of the internal energy from different IQCD calculations are not unique, thus adding to the uncertainty in the potential definition. For example, in perturbative approaches [81, 82] the free energy has been identified with the heavy-quark potential. In the vicinity of a phase transition and/or in the presence of a confining term, this notion is less obvious. In Ref. [67] it has been pointed out that, in the static limit, the thermal expectation value of the interaction part of the  $\bar{Q}Q$  Hamiltonian is precisely the internal energy of the  $\bar{Q}Q$  pair and thus the appropriate quantity to serve as in-medium two-body potential. Another alternative has been suggested in Ref. [64] in terms of a linear combination of  $F$  and  $U$ , based on the idea of subtracting the internal energy of the induced gluon cloud. Clearly, the question of extracting a two-body potential from the IQCD free energy deserves further study.

Model comparisons to lattice QCD “data” can be made more quantitative by computing the pertinent spectral functions,  $\rho_\alpha(\omega)$ , within a given approach (see, e.g., Ref. [68] for an early application in the light quark sector): the integral in Eq. (5) can then be easily carried out and compared to IQCD results for Euclidean correlation functions. In the following paragraphs we discuss such line of work within potential models. One idea is that the different binding properties resulting from assuming either  $F$  or  $U$  as potential can be distinguished by such comparisons.

The first applications of a finite- $T$  potential model for charmonia to IQCD correlators has been conducted in Ref. [69]. For the bound-state part a Schrödinger equation was solved using a screened Cornell potential, Eq. (12), as well as IQCD internal energies, with fixed heavy-quark masses. The continuum was modeled as non-interacting with a temperature dependent threshold  $s_0 = s_0(T)$ , leading to a spectral function

$$\rho_\alpha(\omega; T) = 4\pi \sum_i M_i F_i^2 \delta(\omega^2 - M_i^2) + \frac{3}{4\pi} \omega^2 \Theta(\omega - s_0) f_\alpha(\omega, s_0) \quad (16)$$

(the kinematic coefficients  $f_\alpha$  depend on the meson channel  $\alpha$ ,  $F_i$  are wave-function overlaps at  $r=0$ , and the sum over  $i$  includes all bound states for a fixed  $\alpha$ ). While some trends of the lattice correlator ratios were reproduced, a comprehensive agreement could not be achieved; similar results have been obtained in Ref. [70].

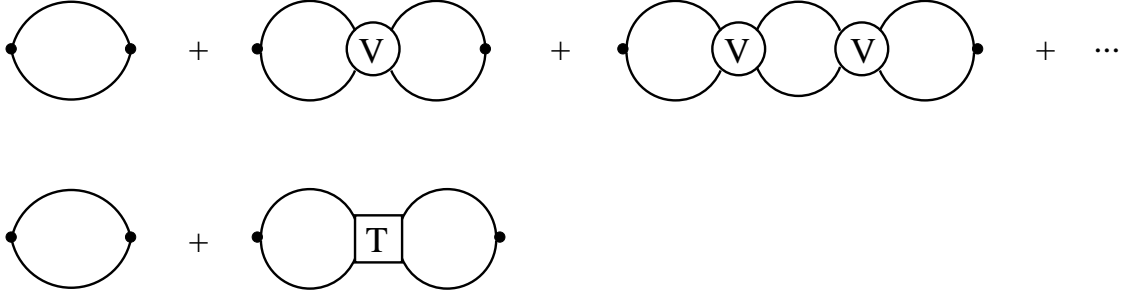


Figure 11: Diagrammatic representation of the  $Q\bar{Q}$  correlation function as obtained from resumming the HQ potential (upper panel) resulting in a folding with the  $T$ -matrix (lower panel) corresponding to Eq. (18). The solid dots represent operators projecting into different mesonic channels  $\alpha$  (giving rise to the coefficients  $a_l$  in Eqs.(19) and (20)) and the 2 connecting lines represent the non-interacting  $\bar{Q}Q$  propagator  $G_{\bar{Q}Q}$ ; figure taken from Ref. [71].

In Ref. [71] the  $T$ -matrix approach introduced in Ref. [66] has been further developed for a systematic analysis of heavy-quarkonium correlator ratios. Starting from the covariant Bethe-Salpeter equation for two-body scattering, one can apply standard reduction schemes to obtain a 3-dimensional Lippmann-Schwinger equation. After a partial-wave expansion, the latter becomes a 1-dimensional integral equation for the  $Q\bar{Q}$   $T$ -matrix which for vanishing total 3-momentum ( $p=0$ ) takes the form

$$T_l(\omega; q', q) = V_l(q', q) + \frac{2}{\pi} \int_0^\infty dk k^2 V_l(q', k) G_{\bar{Q}Q}(\omega; k) T_l(\omega; k, q) \hat{f}^{Q\bar{Q}}(\omega_k); \quad (17)$$

$G_{Q\bar{Q}}(\omega, k)$  denotes the intermediate heavy quark-antiquark propagator,  $\hat{f}^{Q\bar{Q}} = 1 - f^Q - f^{\bar{Q}}$  with  $f^{Q,\bar{Q}}$  HQ Fermi distributions, and  $q$ ,  $q'$  and  $k$  are the (off-shell) 3-momenta of the quarks in the initial, final and intermediate state, respectively. The in-medium  $T$ -matrix equation can be derived from a finite-temperature Green's function approach [72] and constitutes a consistent many-body framework to compute in-medium 1- and 2-particle correlations (it has been widely applied, e.g., in nuclear many-body theory [73], as well as in the analysis of electromagnetic plasmas, as will be discussed in Sec. 2.5). It is particularly suited for the problem at hand since the potentials can be directly identified with the ones extracted from the lattice (after Fourier transformation and partial-wave expansion with angular-momentum quantum number  $l$ ). It treats bound and scattering states on the same footing, which is mandatory for situations where bound states gradually dissolve into a continuum. At the same time, rescattering effects in the continuum, including possible resonance formation, are accounted for by a full resummation of the potential, without the need for matching procedures or  $K$  factors. The 2-particle propagator allows for the implementation of medium effects on the heavy quarks via (complex) single-particle self-energies encoding mass changes (real part) and finite widths (imaginary part). Charmonia widths are important for phenomenological applications in heavy-ion reactions and thus should be accounted for in correlator analyses. The  $T$ -matrix is directly related to the correlation function in momentum space by a double folding over external vertices, schematically given by

$$G = G^0 + G^0 T G^0 \equiv G^0 + \Delta G, \quad (18)$$

and illustrated in Fig. 11. Performing a partial wave expansion and keeping the leading terms in  $1/m_Q$  the explicit form of the correlator becomes

$$G_l^0(\omega) = \frac{2N_c}{\pi} \int k^2 dk a_l(k, k) G_{\bar{Q}Q}(\omega; k) \hat{f}^{Q\bar{Q}}(\omega_k) \quad (19)$$

$$\Delta G_l(\omega) = \frac{N_c}{\pi^3} \int k^2 dk G_{\bar{Q}Q}(\omega; k) \hat{f}^{Q\bar{Q}}(\omega_k) \int k'^2 dk' G_{\bar{Q}Q}(\omega; k') \hat{f}^{Q\bar{Q}}(\omega_{k'}) a_l(k, k') T_l(\omega, k, k'), \quad (20)$$

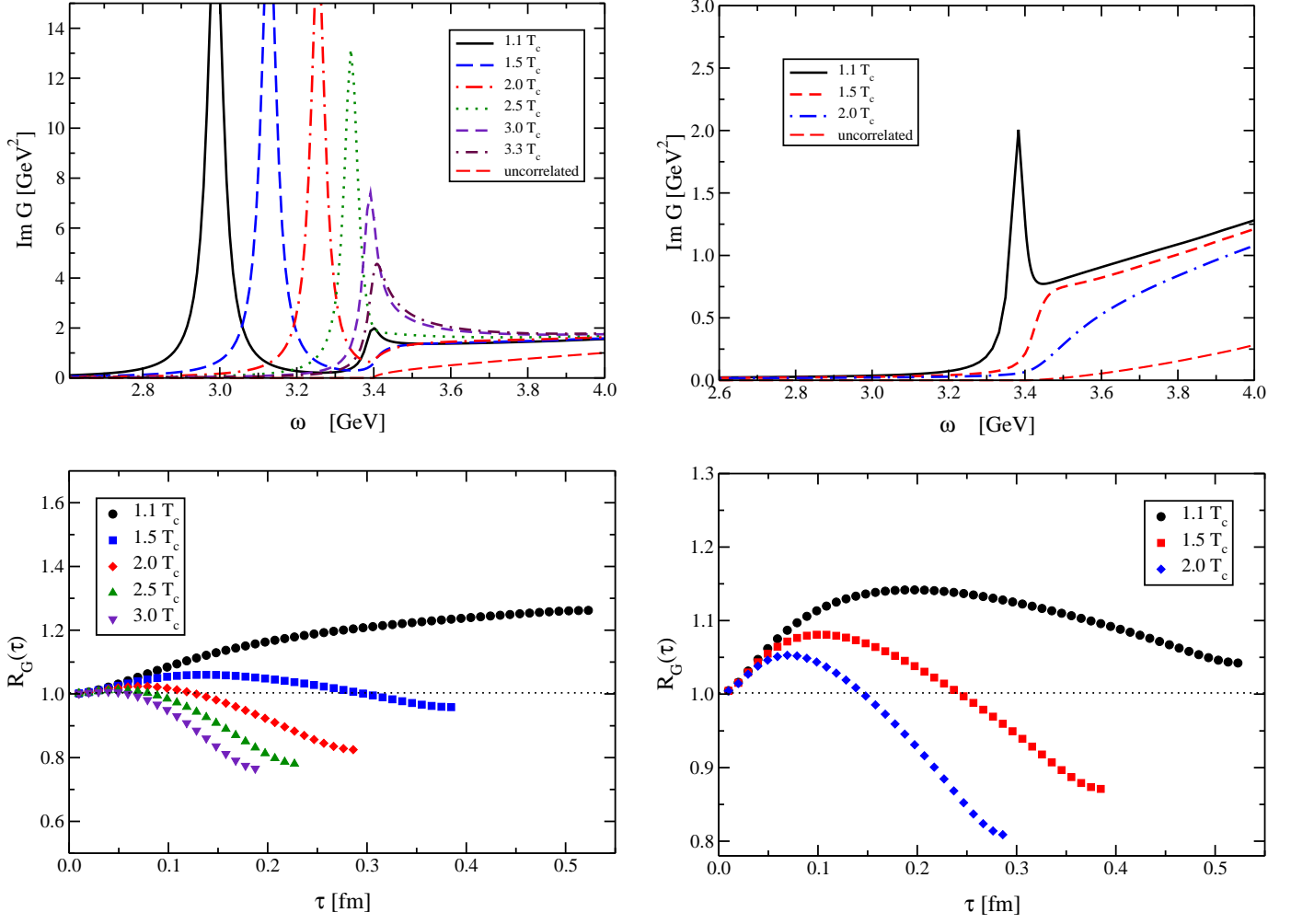


Figure 12: Charmonium spectral functions (upper panels) and pertinent Euclidean-time ( $\tau$ ) correlator ratios (lower panels), Eq. (8), within the  $T$ -matrix approach of Ref. [71] using the internal energy extracted from  $N_f=3$  lattice QCD [57] as input potential. Note that the energy range in the upper panels is smaller than in Figs. 7 and 14, to better resolve the bound-state and threshold regime. The correlator ratios are normalized using the calculated vacuum spectral function. The left panels represent  $S$ -wave states ( $J/\psi$ ,  $\eta_c$ ) while the right ones correspond to  $P$ -waves ( $\chi_{c0}$ ,  $\chi_{c1}$ ). The charm-quark mass has been fixed at  $m_c=1.7$  GeV and a small width of 20 MeV has been introduced in the  $Q$  and  $\bar{Q}$  propagator for better display of the bound-state regime.

with coefficients  $a_{0,1}(k, k')=2, 2kk'/m_Q^2$  in the  $S$ - and  $P$ -wave channels, respectively. The imaginary part of the correlator is just the spectral function (up to a constant factor). To leading order in  $1/m_Q$ , HQ spin symmetry implies degeneracy of different spin states within a partial wave (i.e., for  $S$ -waves  $\eta_c$  and  $J/\psi$ , as well as for the  $P$ -wave  $\chi_c$  states). Results of the  $T$ -matrix approach for spectral and correlation functions are shown in Fig. 12 for a constant effective  $c$ -quark mass ( $m_c=1.7$  GeV) and a small width ( $\sim 20$  MeV) in the quark propagators (for better resolution we here focus on the energy regime around the open-charm threshold,  $\omega_{thr} = 2m_c$ ). For the potential the (subtracted)  $N_f=3$  internal energy of Ref. [57] has been employed. The spectral functions displayed in the upper panels of Fig. 12 indicate that the  $J/\psi$  (or  $\eta_c$ ) dissolves around  $\sim 3T_c$  ( $\sim 2.5T_c$  when using the internal energy of Ref. [74]), while the  $\chi_c$  states melt at lower temperatures,  $\sim 1.3T_c$ . These values should be considered as upper limits, since larger widths will lead to a melting at smaller temperatures. The continuum part of the spectral functions in both  $S$ - and  $P$ -waves exhibits a large enhancement over the non-interacting case; this effect cannot be neglected in quantitative applications to correlation functions. The pertinent temporal

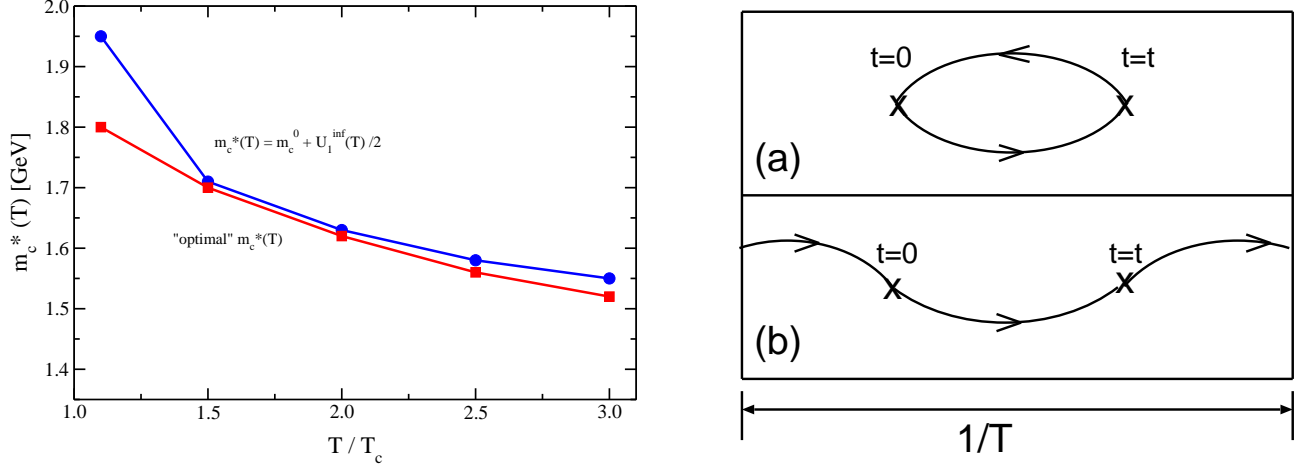


Figure 13: Two effects at the single HQ level relevant to quarkonium correlators. Left panel: in-medium charm-quark mass following from the asymptotic value of the internal energy (upper curve) [57, 71] and as inferred from a “fit” to the  $\eta_c$  correlator [75] as shown in the upper right of Fig. 15. Right panel: contributions to temporal correlation functions computed in finite-temperature lattice QCD [76]. In addition to the standard mesonic point-to-point correlator (upper panel), the periodic boundary conditions in  $\tau$  direction allow for a quark scattering diagram (lower panel).

correlator ratios,  $R_G^\alpha$  (recall Eq.(8)), are plotted in the lower panels of Fig. 12. In the  $S$ -wave they are qualitatively similar to the ones in lQCD, while in the  $P$ -waves they are quite different in both magnitude and temperature dependence, recall Fig. 8. In particular, the decreasing trend at large  $\tau$  indicates that the model spectral functions are missing low-energy strength with increasing temperature. In the  $\eta_c$  channel, this problem is largely overcome when the in-medium charm-quark mass, as following from the asymptotic value of the internal energy, is included, i.e.,

$$m_c^*(T) = m_c^0 + U_{Q\bar{Q}}^{(1),\infty}(T)/2, \quad (21)$$

displayed in the left panel of Fig. 13. This stabilizes the  $T$ -dependence of the  $\eta_c$  correlator ratio [71], but it is not enough to quantitatively improve on the agreement with the lQCD results for  $J/\psi$  and  $\chi_c$ .

An essential part of this puzzle has been identified in Ref. [76], in terms of an energy-independent (but  $T$ -dependent) contribution to the correlators which arises due to the periodic boundary conditions in the (finite)  $\tau$  direction at finite temperature (see right panel of Fig. 13). This term may be interpreted as a scattering contribution of a single heavy quark in the medium which generates a low-energy peak in the quarkonium spectral functions that can be related to a contribution from a heavy-quark susceptibility,  $\chi_\alpha$ , to the lattice QCD correlators [77]. These contributions have been readily implemented into potential model analyses and are found to largely resolve the discrepancies with the lQCD correlator ratios [75, 78, 79]. While the pseudoscalar ( $\eta_c$ ) correlator appears to be free of the zero-mode contribution, the  $P$ -wave correlators in the QGP are enhanced appreciably, in particular at large  $\tau$  (the  $J/\psi$  is mildly affected). This is due to the additional very-low energy strength in the spectral functions which, in quasiparticle approximation, is generated by extra terms  $\sim \chi_\alpha \omega \delta(\omega)$ . When implementing these into the correlation functions and evaluating the susceptibilities,  $\chi_\alpha$ , for a free gas, the description of the lQCD  $P$ -wave correlator ratios (Fig. 8) is much improved [75, 78, 79], see lower panels in Figs. 14 and 15. However, the agreement of the potential approaches with lQCD correlator ratios still allows for a significant redundancy in the underlying spectral functions, leading to rather different conclusions on the “melting” temperatures of the various charmonia, as we will now discuss.

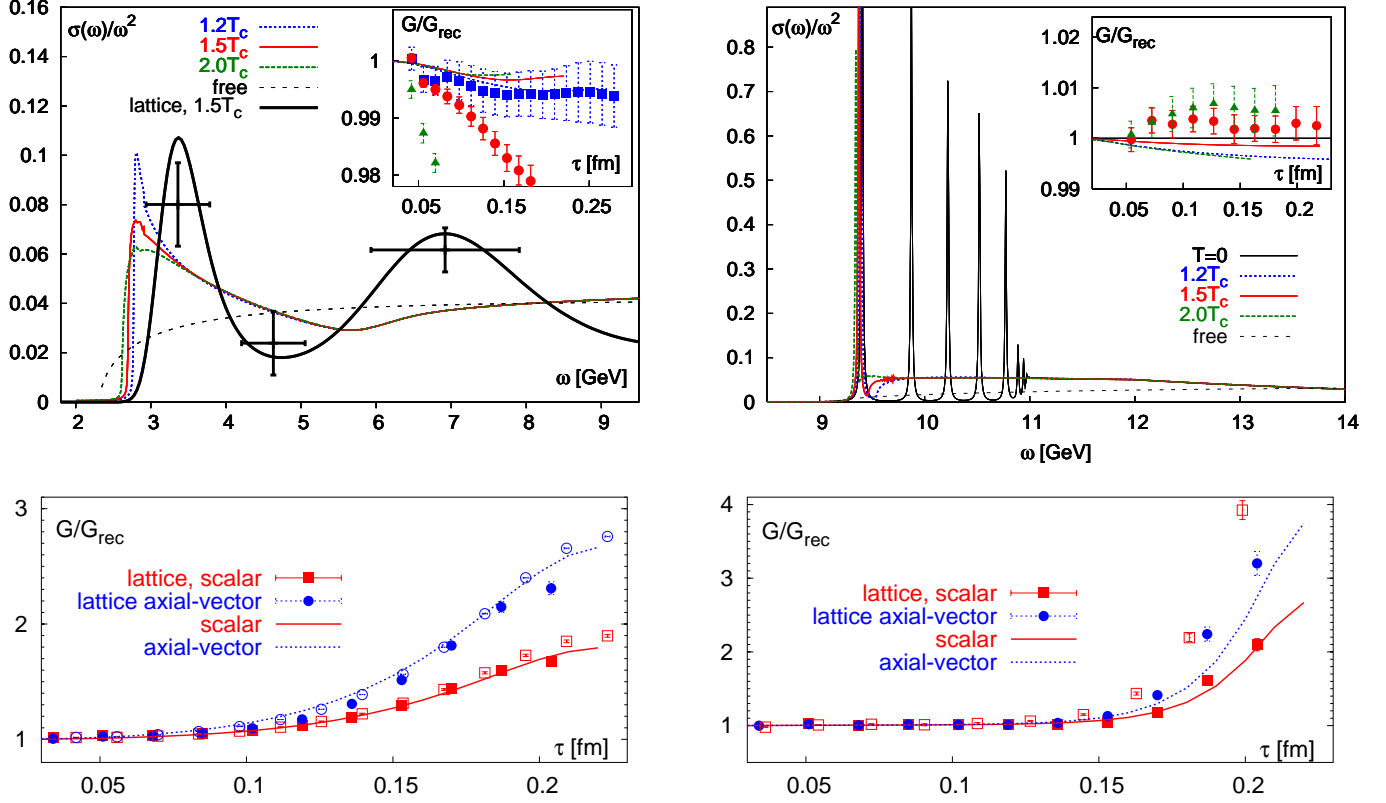


Figure 14: Quarkonium spectral functions and correlator ratios in a Gluon Plasma (quenched QCD) within a nonrelativistic Green's function approach employing a screened Cornell potential [78], supplemented with a perturbative QCD continuum including a  $K$  factor at high energies. Upper panels: spectral functions and correlator ratios (insets) for  $S$ -wave charmonium ( $\eta_c$ , left) and bottomonium ( $\eta_b$ , right) at various temperatures (the data points in the inset are lQCD results with the same color code as for the calculations represented by the lines); the lattice results are for quenched QCD [51], with the data points in the spectral functions indicating the statistical uncertainty (vertical error bar) of the MEM over the energy interval indicated by the horizontal bar (same as in upper left panel of Fig. 7). Lower panels: Euclidean correlator ratios for  $P$ -wave charmonia (left) and bottomonia (right) at  $1.5 T_c$ ; closed and open symbols are quenched lQCD results using isotropic [49, 80] and anisotropic [51] lattices.

In Ref. [78], a screened Cornell potential has been employed within a nonrelativistic Green's function approach to describe the low-energy part of the spectral function. The latter has been combined with a high-energy part which has been approximated with a perturbative continuum multiplied by a  $K$  factor (simulating radiative corrections) to match the large- $\tau$  behavior of the lQCD data. Above  $T_c$  the  $S$ -wave charmonium and bottomonium spectral functions exhibit a moderate variation with  $T$  close to threshold, cf. upper panels in Fig. 14. The  $\eta_c$  state melts at a temperature as low as  $T \simeq 1.3 T_c$ , but the corresponding  $S$ -wave correlator changes little with temperature, roughly consistent with the small variations found in the lQCD correlator ratios (cf. the insets in the upper left panels). It was therefore concluded that the lQCD correlators are consistent with a melting of all charmonium states at temperatures below  $1.3 T_c$ . Essential to this argument is a reduction of the in-medium charm-anticharm quark threshold to  $2m_c^* \simeq 2.7$  GeV, together with a nonperturbative threshold enhancement in the spectral function, as first emphasized in the  $T$ -matrix approach of Ref. [71].

In Ref. [79] the in-medium HQ potential was taken as a linear combination of  $F_{Q\bar{Q}}^{(1)}$  and  $U_{Q\bar{Q}}^{(1)}$  (as advocated in Ref. [64]), in connection with a constant HQ mass and a noninteracting perturbative continuum, corresponding to a spectral function as in Eq. (16). Here, the (semi-) quantitative description

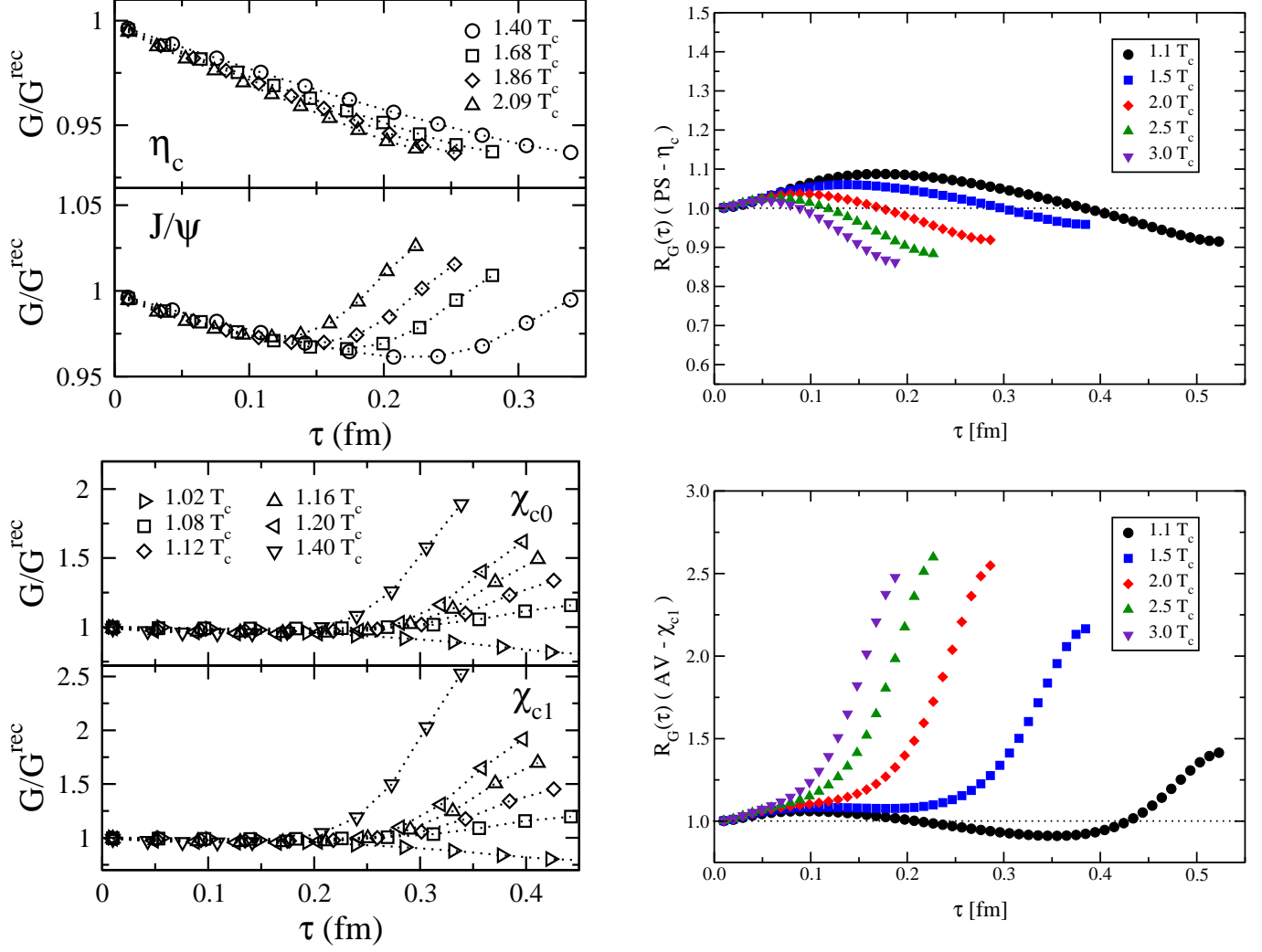


Figure 15: Charmonium correlator ratios,  $R_G = G/G_{\text{rec}}$  as in Eq. (8), including zero-mode contributions. Left panels:  $S$ - and  $P$ -waves (upper and lower left, respectively) in the Schrödinger-equation approach of Ref. [79] where the HQ potential is based on a combination [64] of free and internal energy extracted from unquenched lattice QCD. Right panels:  $\eta_c$  and  $\chi_{c1}$  (upper and lower right, respectively) in the  $T$ -matrix approach of Refs. [71, 75] (employing  $N_f=3$  internal energies from lQCD) including an in-medium charm-quark mass according to the left panel of Fig. 13.

of the lQCD correlator ratios (see left panels of Fig. 15) goes along with a  $J/\psi$  melting at  $\sim 1.6 T_c$ .

The right panels of Fig. 15 depict  $S$ - and  $P$ -wave charmonium correlator ratios within the  $T$ -matrix approach based on the spectral functions in the upper panels of Fig. 12, where the HQ potential is taken as the (subtracted) internal energy. The in-medium charm-quark mass has been calculated including the asymptotic value of the internal energy,  $m_c^* = m_c^0 + U_{Q\bar{Q}}^{(1),\infty}(T)/2$  (except close to  $T_c$  where the large entropy contribution,  $TS_{Q\bar{Q}}^{(1),\infty}$ , is problematic, cf. Fig. 13). As in Refs. [78, 79], the lQCD correlator ratios can be approximately reproduced, only that in this approach the dissolution temperature of the  $J/\psi$  is around  $\sim 2.5 T_c$ .

In a slightly different line of work, potential models have recently been developed utilizing perturbative techniques, starting with a suitable identification of the static finite- $T$  HQ potential [58, 59, 81, 82]. It has been found that, even at leading order in  $\alpha_s$ , the potential develops an imaginary part related to Landau damping in  $t$ -channel gluon exchange (cf. Ref. [83] for an analysis using classical lQCD). When applied within a Schrödinger equation in the bottomonium sector, bound-state solutions emerge

which gradually melt with temperature [84]; pertinent spectral functions exhibit a large threshold enhancement, not unlike the ones displayed in Fig. 12 [71]. In Ref. [85] it has been shown that, in weak coupling, quarkonium resonances survive up to temperatures *parametrically* given by  $T \sim g^2 m_Q$ , but have melted at  $T \sim gm_Q$  (the melting occurs at  $T \sim g^{4/3} m_Q$  [58]).

Let us briefly reflect on the main points of Secs. 2.1 and 2.2. The main strength (and best accuracy) of IQCD lies in the computation of euclidean correlators, which, however, are difficult to transform unambiguously into spectral functions containing the information on the physical excitation spectrum (such as the existence, masses and widths of the quarkonium states). Potential models, on the other hand, are less general in principle (e.g., based on a static approximation), but have the advantage of enabling direct calculations of spectral functions and providing insights into the underlying mechanisms (e.g., color screening and quark-mass dependencies). Moreover, the spectral functions can be readily used to calculate pertinent euclidean correlators. It is thus the synergy of IQCD and effective models which provides the best prospects to better understand the properties of heavy quarkonia in the QGP. More concretely, IQCD computations of Euclidean correlator ratios and associated spectral functions (Figs. 7, 8) exhibit a weak temperature dependence for  $S$ -wave states ( $\eta_c, J/\psi$ ), while  $P$ -wave ( $\chi_c$ ) correlators increase substantially. Potential models employing IQCD-motivated input potentials (or screened Cornell potentials) can essentially reproduce the IQCD results (Figs. 14, 15), but the interpretation is not conclusive: the required low-energy strength in the  $S$ -wave spectral functions can be provided by either bound states surviving up to  $\sim 2T_c$ , or by a rather strong reduction in the open-charm threshold in connection with a nonperturbative rescattering enhancement. The increase in the  $P$ -wave correlators can be accounted for by a low-energy transport peak which is not directly related to bound-state physics (but may be sensitive to the charm-quark mass [86]). A quantitative determination of the in-medium HQ mass will therefore be important to make further progress. Another ingredient that has not received much attention in the context of correlators is the (inelastic) width of the charmonium spectral function, which is a very relevant quantity for heavy-ion phenomenology. This is the topic of the following Section.

## 2.3 Quarkonium Dissociation Reactions in the QGP

The survival of a charmonium state in the QGP does not imply that it is protected from suppression, since it can be dissociated by inelastic collisions with surrounding partons<sup>6</sup>. By detailed balance the inverse of these reactions leads to charmonium *formation*, and therefore the pertinent inelastic width,  $\Gamma_\Psi = (\tau_\Psi)^{-1}$ , is directly related to the relaxation time,  $\tau_\Psi$ , of the charmonium abundance toward its thermal equilibrium number,  $N_\Psi^{\text{eq}}$ . This is immediately borne out of the pertinent kinetic rate equation for the time evolution of the charmonium number  $N_\Psi(\tau)$ , which for a spatially homogeneous system takes the simple form

$$\frac{dN_\Psi}{d\tau} = -\Gamma_\Psi(N_\Psi - N_\Psi^{\text{eq}}) \quad (22)$$

(its solutions in the context of heavy-ion collisions will be discussed in Sec. 3.1 below). As usual, such a rate equation is applicable if a well-defined quasiparticle state  $\Psi$  exists and if the deviation from thermal equilibrium is not too large so that the relaxation time approximation is valid. In general, the dissociation of a composite quasi-particle in a medium can be classified into the following processes:

- (1) direct decays,  $\Psi \rightarrow c + \bar{c}$  (or  $\Psi \rightarrow c + \bar{c} + g$ );
- (2) inelastic collisions with partons, most notably

---

<sup>6</sup>In the following, we refer to  $\Psi = \eta_c, J/\psi, \psi', \chi_c, \dots$  as a generic charmonium state, and  $Y = \eta_b, \Upsilon, \Upsilon', \chi_b, \dots$  as a bottomonium state. To streamline the discussion, we concentrate on charmonia. Most of the arguments also apply to bottomonia although regeneration effects are expected to be less important than for charmonia.

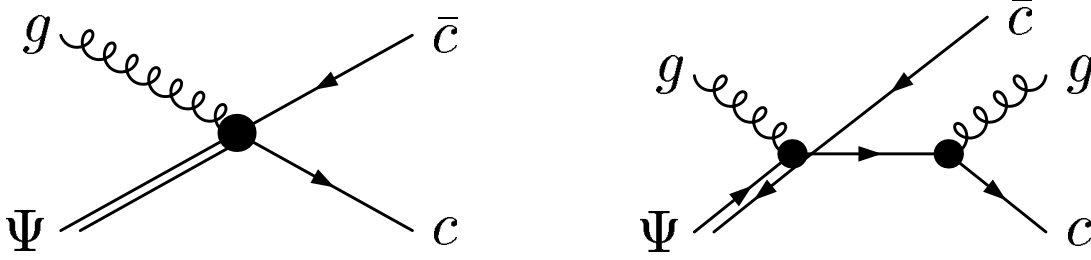


Figure 16: Charmonium dissociation reactions via parton impact; left panel: gluo-dissociation [88, 89] representing the leading-order QCD process; right panel: quasifree dissociation [44] representing a next-to-leading order process.

(2i)  $\Psi + g \rightarrow c + \bar{c}$  (cf. left panel in Fig. 16)

(2ii)  $\Psi + i \rightarrow c + \bar{c} + i$ , with  $i = g, q, \bar{q}$  (cf. right panel in Fig. 16).

Note that the distinction between a bound and a resonance state from the point of view of the rate equation (22) is immaterial; it matters, however, for quantitative assessments of the dominant contributions to the inelastic width. E.g., if a  $\Psi$  state moves into the continuum, i.e., above the  $c\bar{c}$  threshold, at a certain temperature, the opening of the direct-decay channel usually renders it the dominant process. In this sense the dissolution of a state due to screening corresponds to the  $\Gamma_\Psi \rightarrow \infty$  limit of direct decays. The potential-model calculations discussed in the previous section indeed suggest that once a charmonium state becomes unbound, resonance states can no longer be supported. On the other hand, for binding energies of the order of 100 MeV, inelastic widths of a similar magnitude could induce a “premature” melting of the state (the dissociation temperatures quoted above are therefore to be considered as upper limits).

A standard approach to compute inelastic reaction rates in a thermal medium is to calculate the cross section for a given dissociation reaction and fold it over the thermal distribution of the (on-shell) medium particles,

$$\Gamma_\Psi = \int \frac{d^3k}{(2\pi)^3} f^{q,g}(\omega_k, T) v_{\text{rel}} \sigma_\Psi^{\text{diss}}(s) \quad (23)$$

( $v_{\text{rel}}$ : relative velocity of the incoming particles in the center of mass of the collision;  $s=(p+k)^2$ : center-of-mass energy squared of the parton- $\Psi$  collision). The cross section for gluo-dissociation,  $g + J/\psi \rightarrow c + \bar{c}$ , has been evaluated in Refs. [88, 89, 148], using hydrogen-like wave functions. The latter are expected to be a good approximation as long as the Coulombic part of the Cornell potential dominates the  $Q\bar{Q}$  bound-state properties. As noted in Refs. [88, 89] this approximation is not really (marginally) satisfied for the  $J/\psi$  ( $\Upsilon$ ) with vacuum binding energies of  $\sim 0.6(1.0)$  GeV. Within these limitations, the gluo-dissociation cross section for massless gluons of energy  $k_0$  incident on a ground-state quarkonium reads

$$\begin{aligned} \sigma_{g\Psi,Y}(k_0) &= \frac{2\pi}{3} \left(\frac{32}{3}\right)^2 \left(\frac{m_Q}{\varepsilon_B}\right)^{1/2} \frac{1}{m_Q^2} \frac{(k_0/\varepsilon_B - 1)^{3/2}}{(k_0/\varepsilon_B)^5} \\ &= 2\pi \left(\frac{16}{3}\right)^2 \alpha_s a_0^2 \frac{(k_0/\varepsilon_B - 1)^{3/2}}{(k_0/\varepsilon_B)^5}, \end{aligned} \quad (24)$$

where  $\varepsilon_B$  denotes the quarkonium binding energy and  $m_Q$  the effective heavy-quark mass (as used, e.g., in fits to vacuum quarkonium spectra). The second line has been obtained by using the Coulomb-potential expressions for binding energy,  $\varepsilon_B = (\frac{3}{4}\alpha_s)^2 m_Q$ , and Bohr radius,  $a_0 = 4/(3\alpha_s m_Q)$ . It illustrates the leading-order (LO) character ( $\mathcal{O}(\alpha_s)$ ) of the cross section, being proportional to the

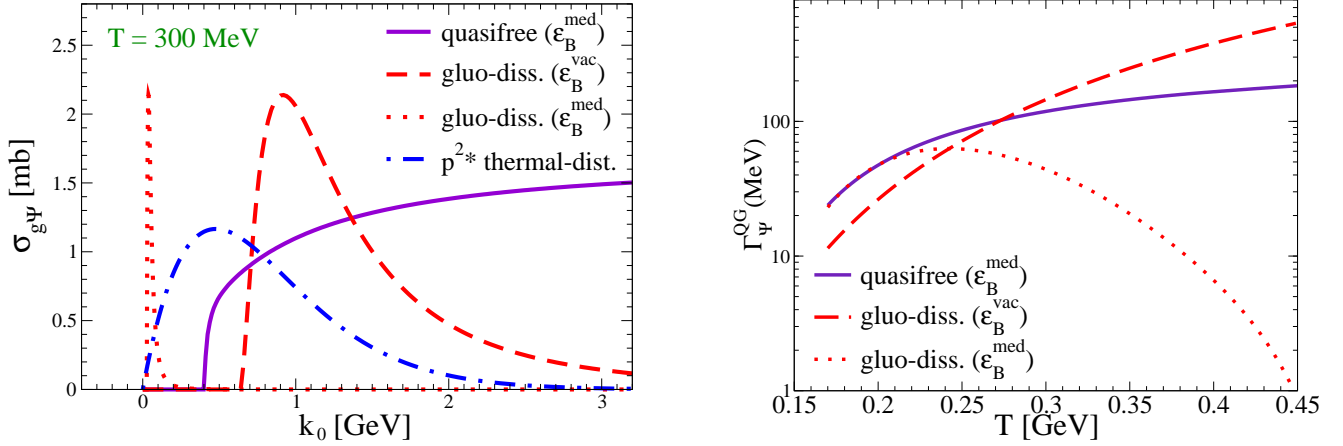


Figure 17: Total cross sections (left panel) and pertinent dissociation rates (right panel) for  $J/\psi$  dissociation reactions in the QGP: gluo-dissociation,  $g + J/\psi \rightarrow c + \bar{c}$ , according to Eq. (24) with vacuum ( $\epsilon_B=640$  MeV, dashed line) and in-medium ( $\epsilon_B \simeq 30$  MeV, dotted line) binding energies (the pertinent phase distribution,  $p^2 f^B(p; T)$ , for massless gluons is illustrated by the dash-dotted line); parton-induced quasifree dissociation,  $i + J/\psi \rightarrow c + \bar{c} + i$ , using an in-medium binding energy,  $\mu_D = gT$  and thermal parton masses  $m_i \propto gT$  [44, 92].

“geometric size” of the bound state. The cross section has a threshold at  $k_0^{\text{thr}} = \epsilon_B$  and acquires its maximum at  $k_0^{\text{max}} = \frac{10}{7}\epsilon_B$ , cf. left panel of Fig. 17. For QGP temperatures of 200–300 MeV, typical for SPS and RHIC energies, the average thermal gluon energy of  $3T$  amounts to 600–900 MeV, providing good overlap with the vacuum gluo-dissociation cross section and resulting in dissociation rates of  $\Gamma_{J/\psi} \simeq 30 - 200$  MeV, see right panel of Fig. 17. However, if the binding energy decreases with temperature, the available phase space of gluo-dissociation shrinks substantially. E.g., in the screened potential model of Ref. [60], corresponding to Eq. (12), a moderate screening mass of  $\mu_D \simeq gT$  with  $\alpha_s \simeq 0.25$  ( $g \simeq 1.75$ ), yields a  $J/\psi$  binding energy of only about 200(30) MeV at  $T=180(300)$  MeV, reaching zero at around 360 MeV. Under these conditions the gluo-dissociation rate decreases with increasing temperature for  $T \geq 250$  MeV, cf. dotted line in the right panel of Fig. 17. This signals that other dissociation processes become important (see also Refs. [64, 90, 91]). For the same reason, the gluo-dissociation process cannot provide a realistic description for the dissociation of excited charmonia whose binding energies are small already in the vacuum.

An early nonperturbative approach to compute heavy quarkonium break-up from quark impact (corresponding to the category (2ii) of the above classification) has been suggested in Ref. [93] in analogy to electron-induced atom ionization; the pertinent “thermal activation” cross section,

$$\sigma(T) = \pi r_{Q\bar{Q}}^2 e^{-k_0^{\text{diss}}/T}, \quad (25)$$

is characterized by a temperature dependent dissociation energy,  $k_0^{\text{diss}} \equiv \epsilon_B$ , while the coefficient has been estimated by the “geometric” transverse size of the bound state,  $\pi r_{Q\bar{Q}}^2$  (cf. Ref. [94] for an alternative derivation of a similar result, which was shown to apply to sufficiently large dissociation energies,  $k_0^{\text{diss}} \gg T$ ). To obtain more quantitative results, microscopic approaches are required.

In Refs. [44, 92] the dissociation reactions of weakly bound charmonia have been treated within a quasifree approximation for parton impact on either one of the heavy quarks within the bound state,  $i + \Psi \rightarrow c + \bar{c} + i$ . The basic process is (quasi-) elastic  $i + c \rightarrow i + c$  scattering [98], including the proper dissociation kinematics (i.e., finite  $\epsilon_B$  and 4-momentum conservation), as well as thermal parton and Debye masses (the latter are essential to render the dominant  $t$ -channel gluon-exchange contributions finite). The key quantities controlling the rate are  $\alpha_s$ ,  $\mu_D$  and  $\epsilon_B$ , while the dependence on  $m_c$  is weak.

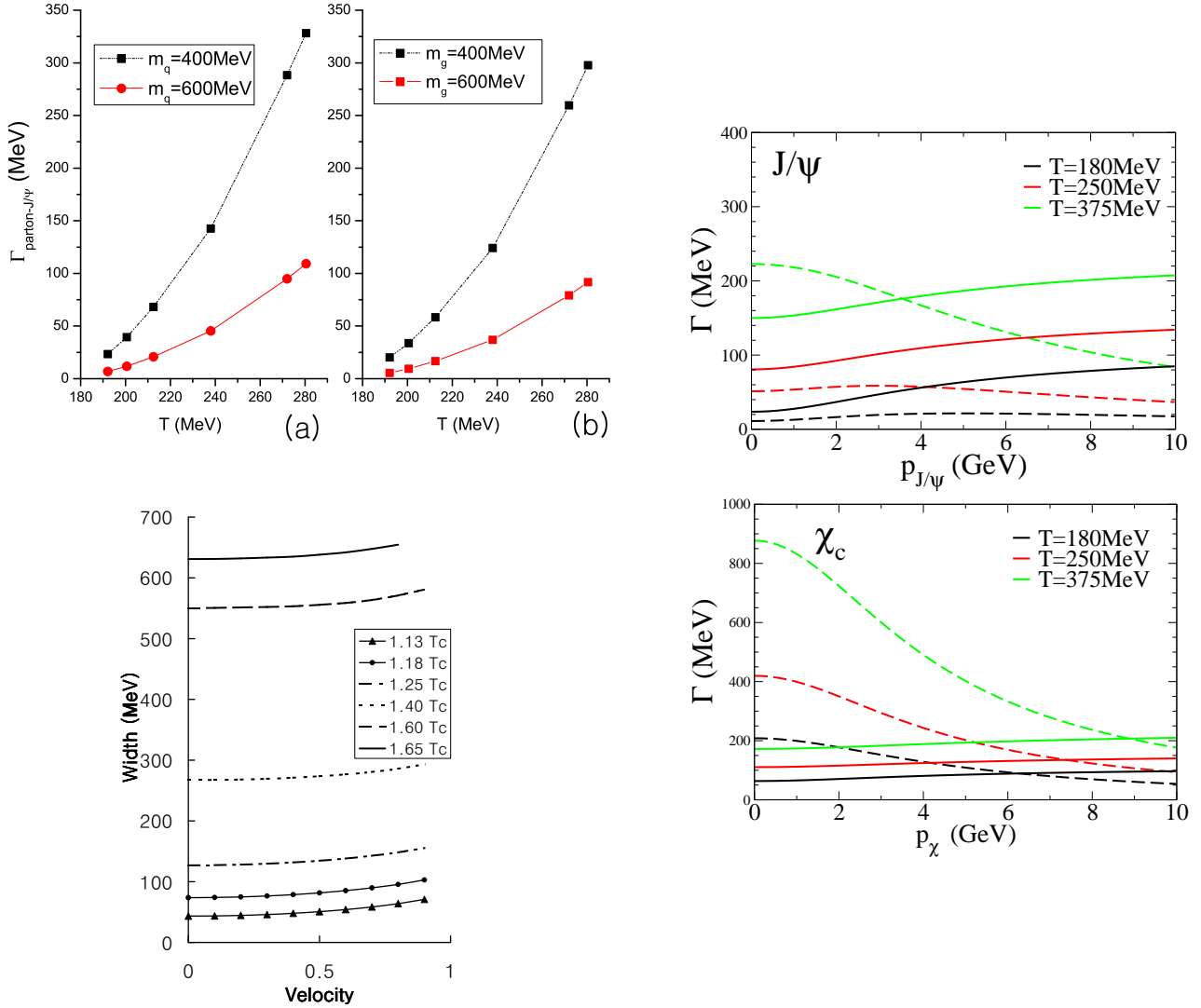


Figure 18: Parton-induced  $J/\psi$  dissociation rates in the QGP. Left panels: NLO results using in-medium binding energies ranging from  $\sim 40 \rightarrow 0$  MeV for  $T=190 \rightarrow 280$  MeV (upper left:  $T$  dependence of  $\Gamma_{J/\psi}(p=0)$  for (a) quark- plus antiquark- and (b) gluon-induced reactions for constant thermal parton masses [95]; lower left:  $\Gamma_{J/\psi}^{\text{tot}} = \Gamma_{J/\psi q + \bar{q}} + \Gamma_{J/\psi g}$ , as a function of the  $J/\psi$  3-velocity,  $v = p/\omega_p$ , relative to the heat bath for different temperatures with constant thermal parton masses of 600 MeV [96] and  $T_c = 170$  MeV). Right panels: comparison of the 3-momentum dependence of  $J/\psi$  (upper right) and  $\chi_c$  (lower right) dissociation rates at 3 different temperatures using either gluo-dissociation with vacuum binding energies [88, 89] (dashed lines) or quasifree destruction with in-medium binding energies [44, 97] (solid lines).

Formally, these reactions are of next-to-leading order (NLO) compared to LO gluo-dissociation, but the available phase space in the cross section is substantially increased (see solid line in the left panel of Fig. 17), leading to significantly larger dissociation rates at temperatures where the charmonium binding is weak (see solid line in the right panel of Fig. 17). In fact, the infrared singularity in the  $t$ -channel exchange of a (Debye-screened) gluon for inelastic quarkonium scattering off thermal partons renders this process of order  $g^2$ .

A complete NLO calculation has recently been performed in Ref. [95] confirming the prevalence of  $i + J/\psi \rightarrow c + \bar{c} + i$  over  $g + J/\psi \rightarrow c + \bar{c}$  processes for weak binding. More quantitatively, for

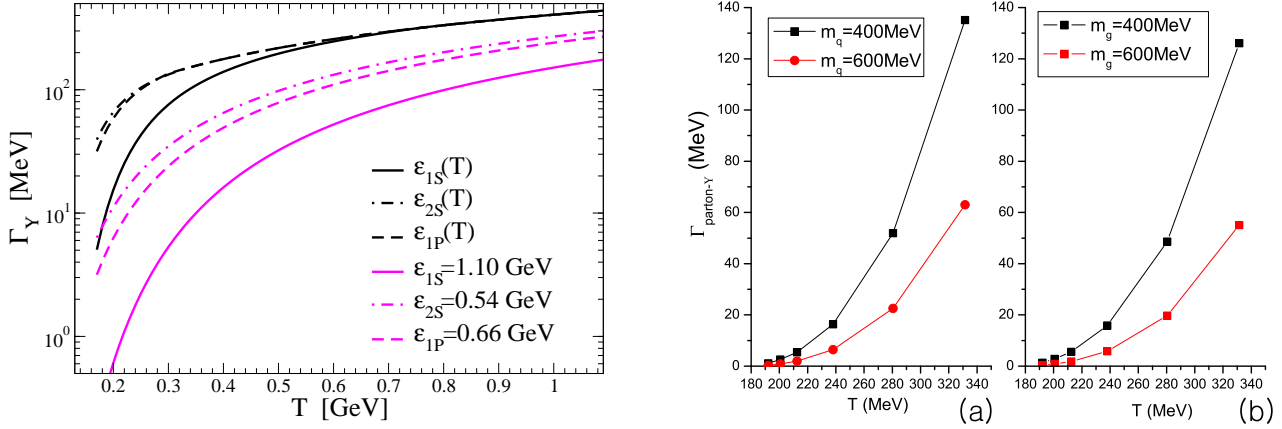


Figure 19: Bottomonium dissociation rates in the QGP. Left panel: quasifree calculation [99],  $\Upsilon + i \rightarrow b + \bar{b} + i$  ( $i=q, \bar{q}, g$ ), using  $\alpha_s \simeq 0.25$  with vacuum (lower curves) and in-medium (upper curves) binding energies for  $\Upsilon$ ,  $\chi_b$  and  $\Upsilon'$  (the in-medium binding energies are based on Ref. [60], with  $\epsilon_B^\Upsilon \simeq 550(200)$  MeV at  $T=180(350)$  MeV). Right panels: NLO calculations for quark- and gluon-induced break-up of the ground-state  $\Upsilon$  [95] (sub-panels (a) and (b), respectively) including  $\Upsilon + g \rightarrow b + \bar{b}$  and  $\Upsilon + i \rightarrow b + \bar{b} + i$  with in-medium binding energies,  $\alpha_s=0.5$  and two different values for thermal parton masses.

$\alpha_s=0.5$ ,  $T=250$  MeV and thermal parton (Debye) masses  $m_{q,g} = 400$  MeV, the total dissociation width of a weakly bound  $J/\psi$  has been found to be  $\Gamma_{J/\psi} \simeq 350$  MeV. This is in reasonable agreement with Refs. [44, 92] where, using  $\alpha_s \simeq 0.25$ ,  $\Gamma_{J/\psi}(T=250 \text{ MeV}) \simeq 80$  MeV, since the NLO rate is proportional to  $\alpha_s^2$  (modulo screening-mass corrections in  $t$ -channel gluon exchange diagrams for forward scattering; e.g., at  $T=250$  MeV, the Debye mass in Refs. [44, 92] is  $\mu_D=440$  MeV). For a constant Debye mass, the NLO results of Refs. [95] exhibit a rather strong increase of  $\Gamma_{J/\psi}$  with temperature (upper left panel in Fig. 18), which is, however, tamed if a perturbative temperature dependence,  $\mu_D \propto g(T)T$ , were included (since the rates decrease with increasing  $\mu_D$ ). The dependence of the NLO rate on the 3-momentum,  $p$ , of the  $J/\psi$  is rather flat, see lower left panel in Fig. 18 [96]. This is quite different from the LO gluo-dissociation process whose rate drops substantially with  $p$  (even more so for weak binding for which the cross section is concentrated at small gluon energies), see dashed lines in the right panels of Fig. 18. The  $p$  dependence following from the quasifree dissociation rate [97] (solid lines in the right panels of Fig. 18) is quite similar to the full NLO calculation (recall that  $\alpha_s$  differs by a factor of  $\sim 2$  in these two calculations).

Inelastic collision rates of the ground-state  $\Upsilon$  are compiled in Fig. 19. Analogous to charmonia, in-medium reduced binding energies render the quasifree process dominant over gluo-dissociation, see Ref. [99] for a detailed discussion<sup>7</sup>; this has also been confirmed in a complete NLO calculation [95]. Since the vacuum binding energy of the  $\Upsilon$  is quite large ( $\epsilon_\Upsilon^0 \simeq 1.1$  GeV) compared to typical temperatures at RHIC ( $T \simeq 0.3$  GeV), its dissociation rates are rather sensitive to color-screening (which has important consequences for  $\Upsilon$  suppression in heavy-ion collisions), e.g.,  $\sim 7$  MeV for  $\epsilon_\Upsilon^0 \simeq 1.1$  GeV vs.  $\sim 80$  MeV for  $\epsilon_\Upsilon^{\text{med}} \simeq 0.25$  GeV at  $T=0.3$  GeV. For comparable values of the parameters (strong coupling constant, binding energy as well as Debye and thermal masses), the widths within the quasifree calculation [99] ( $\epsilon_B(T)$ -curves in the left panel of Fig. 19) tend to be larger than within the NLO analysis [95] (right panel of Fig. 19) when accounting for the factor 2 difference in  $\alpha_s$ . This discrepancy could be due a reduced accuracy of the quasifree approximation for more tightly bound systems [81, 82]. As discussed in the latter paper, in perturbation theory, the imaginary part of the finite-temperature heavy-fermion

<sup>7</sup>For the vacuum binding energy, the gluo-dissociation rate of  $\Upsilon$  is comparable to the quasifree one.

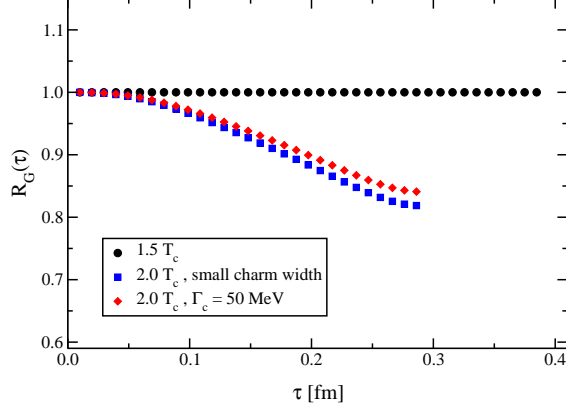


Figure 20:  $S$ -wave charmonium correlator ratios obtained within the  $T$ -matrix approach [71] using 2 different values for the in-medium charm-quark width corresponding to total  $\eta_c$  (or  $J/\psi$ ) widths of 40 MeV (lower squares) and 100 MeV (diamonds); the reconstructed correlator used for normalization is the one at  $1.5 T_c$ , and the charm-quark mass has been held fixed at  $m_c=1.7$  GeV (no zero-mode contributions are included).

potential referred to in the previous section is closely related to quasifree dissociation. In particular, it has been shown that in a QED plasma the infinite-distance limit of the imaginary part,  $\text{Im } V_{Q\bar{Q}}(r \rightarrow \infty) = -g^2 T/4\pi$ , precisely corresponds to (twice) the damping factor of a single heavy fermion in the static limit,  $\Gamma_Q = -g^2 T/8\pi$  (in pQCD, an additional Casimir factor,  $C_F=4/3$ , appears). For small distances (i.e., for tightly bound states), interferences occur which suppress this quarkonium width from the quasifree limit.

Recent calculations have investigated the effects of anisotropic momentum distributions in the QGP on the quarkonium width [100, 101, 102]. The emerging consensus seems to be that anisotropies do not have a large impact on the quarkonium dissociation temperatures and widths as long as the thermal parton density (or entropy density) is kept constant. This conclusion may depend on the microscopic mechanism underlying the dissociation. For example, if the dissociation rate increases (decreases) with 3-momentum, harder momentum spectra of the medium partons may lead to an increase (decrease) in width over the isotropic thermal case.

Finally, let us address the impact of finite-width effects on the charmonium correlator ratios discussed in the previous Section. In the  $T$ -matrix approach of Ref. [71], a  $J/\psi$  width has been implemented via an elastic charm-quark width,  $\Gamma_c$ , in the two-particle propagator,  $G_{Q\bar{Q}}$ , figuring into the Lippmann-Schwinger Eq. (17) (see also Ref. [103] for a more recent calculation). As discussed above, this generates a charmonium width in the spirit of the quasifree dissociation mechanism where the “elastic” scattering of thermal partons essentially occurs with one of the charm quarks within the bound state. Using  $\Gamma_c = \Gamma_{\bar{c}} = 50$  MeV, the  $J/\psi$  spectral function acquires a width of about 100 MeV, and the corresponding correlator ratio with this width is compared to the calculations shown in Fig. 12 (corresponding to a total  $J/\psi$  width of  $\sim 40$  MeV), using the correlator at  $1.5 T_c$  as the reconstructed one. One finds that the moderate increase of the  $J/\psi$  width increases the large- $\tau$  regime of the correlator ratio by a few percent, due to the slight increase of strength in the low-energy part of the spectral function caused by the broadening. More systematic investigations of width effects, especially close to the “melting” temperature, remain to be carried out, e.g., by implementing microscopic dissociation width calculations into the  $T$ -matrix approach. Generally, finite-width effects tend to accelerate the dissociation of the bound state, i.e., lower its dissociation temperature [103].

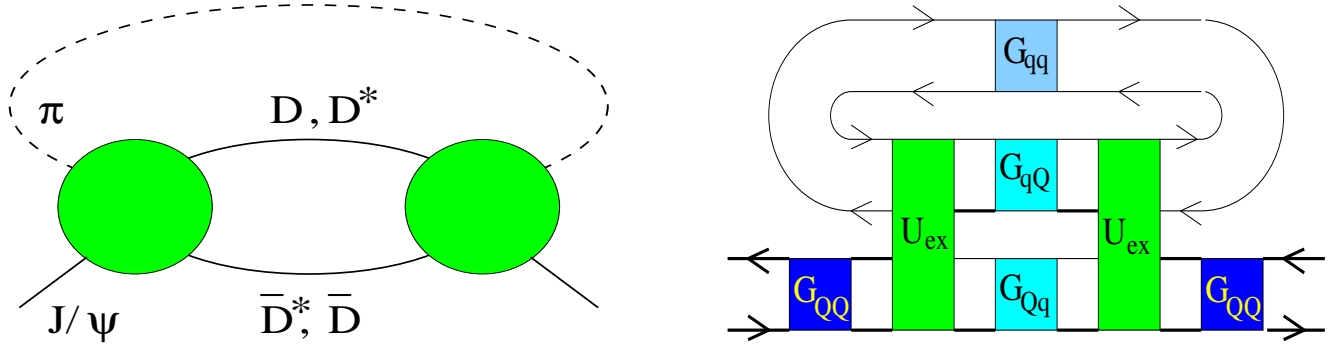


Figure 21: Diagrammatic representation of the  $J/\psi$  self-energy due to interactions with pions from the hadronic heat bath, with effective vertices in a hadronic basis (left panel) and resolved into a quark basis with microscopic pion ( $G_{qq}$ ),  $D$ -meson ( $G_{Qq}$ ) and  $J/\psi$  ( $G_{QQ}$ ) propagators as well quark-exchange interactions ( $U_{\text{ex}}$ ) (right panel) [91]. The  $J/\psi$  dissociation width follows from the imaginary part of the self-energy,  $\Gamma_\Psi = -\text{Im} \Sigma_\Psi/m_\Psi$ ; the underlying process may be visualized by cutting the left-hand diagram through the middle (note that this cannot be done at the quark level since confinement forbids external quark lines in the hadronic phase). Diagrams of this type naturally appear in the cluster expansion for two-particle properties, see Fig. 29 in Sec. 2.5.

## 2.4 Quarkonium Dissociation in Hadronic Matter

The theoretical description of the  $J/\psi$  in medium is not complete without an understanding of its properties in hadronic matter. Since the latter is characterized by confined color charges, color screening of a tightly bound, spatially compact  $c\bar{c}$  state is believed to be negligible below  $T_c$  (on the order of 10 MeV or so) [104]. Thus, most of the calculations of  $J/\psi$  properties in hadronic matter have focused on the role of dissociation reactions of the type  $J/\psi + M \rightarrow D + \bar{D}$  where  $M$  denotes a meson from the heat bath (e.g.,  $\pi$ ,  $\rho$ ) and  $D$  generically denotes a  $D$ -meson (e.g.,  $D(1870)$  or  $D^*(2010)$ ); for reaction with baryons ( $B$ ) from the medium one has  $J/\psi + B \rightarrow \Lambda_c, \Sigma_c + \bar{D}$ . On the phenomenological side, a quantitative assessment of the inelastic reaction rates in the hadronic phase of a heavy-ion reaction is indispensable for disentangling the “anomalous suppression” in the QGP. Here, we focus on the most recent developments over the last 5 years or so (for earlier reviews, see, e.g., Refs. [105, 106, 173, 107, 108]).

The “natural” framework to evaluate hadronic  $J/\psi$  dissociation are effective hadronic models to compute the pertinent inelastic cross section for the reactions of the type listed above. However, even after the exploitation of standard symmetry in hadronic physics (such as vector-current conservation, vector-meson dominance [113] and chiral [111, 112] or broken flavor- $SU(4)$  [113, 114] symmetry), a quantitative control over the dissociation rates could not be achieved due to uncertainties in hadronic formfactors. The latter are required to account for the finite size of the vertices in the effective theory. When varying the pertinent cutoff parameters over a typical hadronic scale, say,  $\Lambda=1\text{-}2\text{ GeV}$ , the  $J/\psi$  dissociation cross sections can vary by about 2 orders of magnitude (from sub-mb to tens of mb). Alternatively, parton-based calculations have been performed which, in principle, could provide a more microscopic description of the effective vertices. Combining the LO gluon-dissociation cross section (as discussed in the previous section for deconfined gluons in the QGP) [88] with the gluon distributions within a hadron, the resulting hadron- $J/\psi$  break-up cross section was found to be small (sub-mb) [148], primarily due to the soft gluon distribution function within the hadrons (also, the thermal motion of hadrons below  $T_c$  is suppressed compared to deconfined gluons above  $T_c$ ; medium effects in the bound state have been studied in Ref. [90], and NLO calculations have been carried out for the  $\Upsilon$  [115] but not for the  $J/\psi$ ). However, the hadronic dissociation reactions of charmonia are presumably dominated by other processes, specifically quark exchanges as illustrated in Fig. 21, which have been addressed within effective quark models [117, 116, 120, 106, 107, 112]. A realistic description of such processes requires

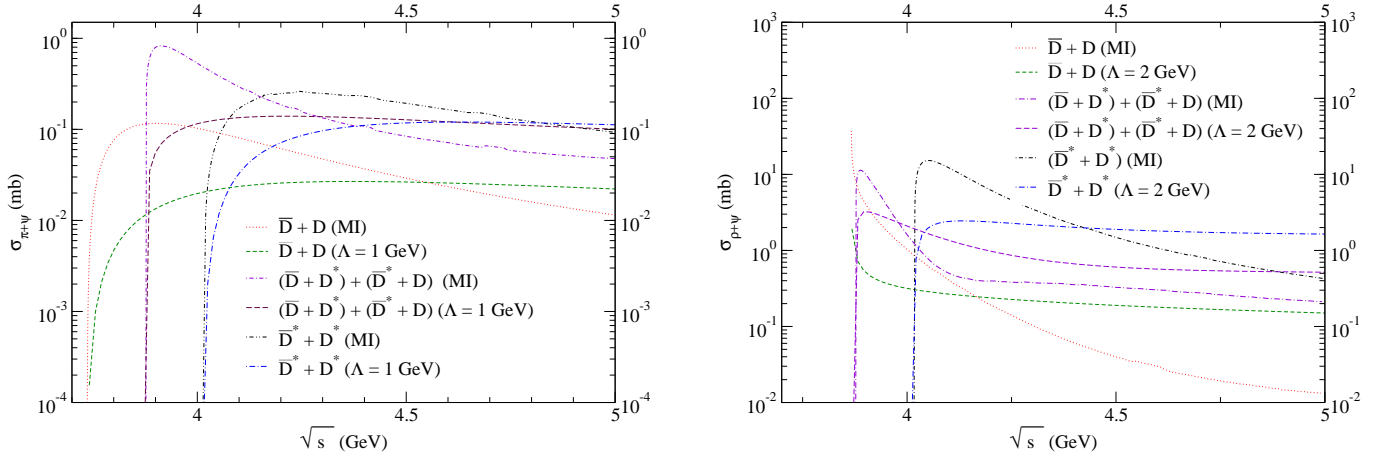


Figure 22: Dissociation cross sections of the  $J/\psi$  induced by pions (left panel) and  $\rho$ -mesons (right panel) as a function of center of mass energy of the reaction. In each panel, results for a chiral (Nambu-Jona-Lasinio) quark model (labeled “MI”) [112] are compared to those for a chiral effective hadronic model [109] in which the vertex formfactor cutoffs (quoted in parenthesis) have been adjusted to approximately match the strength in the quark model calculations. The low-energy thresholds in the left panel correspond to (from left to right)  $2m_D \simeq 3.75$  GeV,  $m_D + m_{D^*} \simeq 3.88$  GeV and  $2m_{D^*} \simeq 4.02$  GeV, and in the right panel to (from left to right)  $m_{J/\psi} + m_\rho \simeq 3.87$  GeV and  $2m_{D^*} \simeq 4.02$  GeV. Figures are taken from Ref. [112].

non-perturbative input in terms of both the effective quark propagators (especially for their momentum-dependent mass functions in the chirally broken and confined hadronic phase) and the interaction vertices (which are usually resummed in ladder approximation). In principle, these quantities can be constrained by vacuum phenomenology (hadron spectra, decay constants and quark/gluon condensates), but their implementation in a hadronic medium poses formidable challenges, including a fully relativistic treatment, cancellations due to constraints from chiral symmetry, etc. Note that the quarkonium propagator,  $G_{Q\bar{Q}}$ , figuring into the right-hand-side of Fig. 21, is closely related to the potential models discussed in Sec. 2.2. For example, the  $D\bar{D}$  state appropriate for hadronic matter could be implemented into the charmonium  $T$ -matrix by coupling an additional  $D\bar{D}$  channel,  $G_{D\bar{D}}$ , into Eq. (17) using a suitably constructed transition potential,  $U_{\text{ex}} \equiv V_{c\bar{c} \rightarrow D\bar{D}}$ .

A recent example for the calibration of hadronic vertices evaluated in chiral effective theory [109] using a chiral quark model [112] is shown in Fig. 22 for the processes  $\pi + J/\psi \rightarrow D + \bar{D}$  (left panel) and  $\rho + J/\psi \rightarrow D + \bar{D}$  (right panel; see also Ref. [121] for a similar analysis). These plots illustrate several features: (a) The energy dependence of the cross sections for hadronic and quark models does not match well; most notably, the quark-model results exhibit threshold peaks which do not appear in the hadronic calculations (whether this is a realistic feature remains to be seen); nevertheless, with formfactor cutoff values in a typical hadronic range,  $\Lambda_{\pi J/\psi} = 1$  GeV and  $\Lambda_{\rho J/\psi} = 1$  GeV, the overall strengths are comparable; (b) the cross sections for  $\rho$ -induced dissociation are significantly larger than the pion-induced ones, and both agree within a factor of  $\sim 2$  with their counterparts in quark-model calculations [105, 106, 107]. This is quite encouraging in view of the much larger uncertainties alluded to above; similar results are obtained in Ref. [121]. A recent comparison for nucleon-induced dissociation can be found in Refs. [118, 110] (note that the low-energy  $\Psi$ - $N$  break-up cross section, which is relevant for  $J/\psi$  absorption in an equilibrated hadron gas, is different from (and probably much smaller than) the high-energy absorption cross section figuring into “nuclear absorption” in heavy-ion collisions discussed in Sec. 3.2).

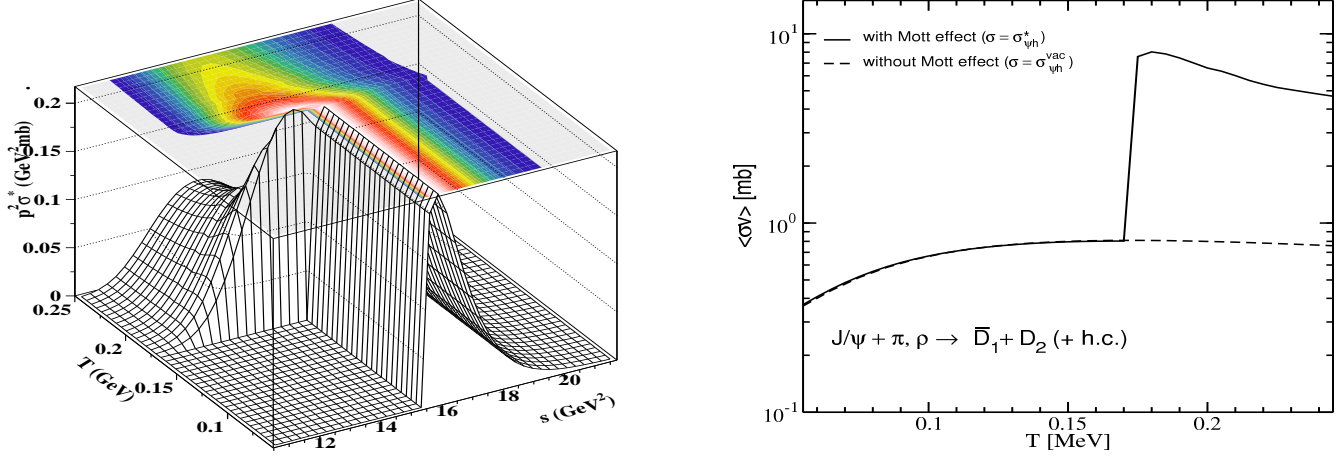


Figure 23: Left panel: energy ( $s$ ) and temperature ( $T$ ) dependence of the effective cross section ( $\sigma^*$ ) for  $J/\psi$  breakup by  $\rho$ -meson impact. We display  $p^2\sigma^*(s; T)$  ( $p$ : initial-state hadron momentum) for better visibility of the effective lowering of the breakup threshold when  $T$  exceeds the  $D$ -meson Mott temperature  $T^{\text{Mott}} \simeq 172$  MeV; right panel:  $T$  dependence of the thermally averaged  $J/\psi$  breakup cross section in a  $\pi$ - $\rho$  gas; the calculation with vacuum  $D$ -mesons (dashed line) is compared to one with in-medium broadened  $D$ -meson spectral functions (due to the Mott effect at the chiral phase transition) causing a step-like enhancement (solid line) caused by the reduced breakup threshold; from Ref. [105].

The energy-dependent cross sections for quarkonium break-up by hadron impact enable to calculate the temperature- (and density-) dependent dissociation rates in hadronic matter. If one assumes the short-distance vertex functions to be unaffected by the surrounding medium, the issue remains whether mass and width of the final-state open-charm hadrons change with temperature and density. These medium effects, in particular, imply modifications of the thresholds for the breakup processes [38, 123, 124, 125, 126, 127, 128]. The theoretical basis for the discussion of quark-exchange effects in the self-energy of heavy quarkonia in strongly correlated quark matter is given by systematic cluster expansion techniques developed in the context of plasma physics (more details are contained in the next subsection in connection with Figs. 26, 27 and 29). Fig. 23 illustrates the effect of the spectral broadening of  $D$ -mesons at the chiral phase transition due to the opening of the decay channel into their quark constituents (Mott effect) for temperatures exceeding the  $D$ -meson Mott temperature,  $T^{\text{Mott}} \approx 172$  MeV. The temperature-dependent lowering of the  $J/\psi$  breakup threshold in the thermally averaged  $J/\psi$  cross section in a  $\pi$ - $\rho$  meson gas induces a step-like enhancement [105]. This effect has been discussed as a possible mechanism underlying the threshold-like anomalous suppression pattern of  $J/\psi$ 's observed by the NA50 experiment [125, 129].

We finally make a rough estimate of the magnitude of the dissociation widths of the  $J/\psi$  in hadronic matter, based on the most recent evaluations discussed above, and compare it to the values found in the QGP as discussed in the previous Section. In analogy to Eq. (23), the  $J/\psi$  dissociation rate in the hadron gas can be written as a convolution of the  $h$ - $J/\psi$  break-up cross section with the thermal distributions of all hadrons  $h$  in the heat bath,

$$\Gamma_{\Psi}^{\text{HG}} = \sum_h \int \frac{d^3k}{(2\pi)^3} f^h(\omega_k, T) v_{\text{rel}} \sigma_{h\Psi}^{\text{diss}}(s). \quad (26)$$

Let us approximate this expression by  $\Gamma_{\Psi} = \langle \sigma^{\text{diss}} n_h^{\text{tot}} v_{\text{rel}} \rangle$  with a total density  $n_h^{\text{tot}} = 5 n_0 = 0.8 \text{ fm}^{-3}$  for a hadron-resonance gas at  $T=175$  MeV. From Figs. 22 and 23 we estimate  $\langle \sigma^{\text{diss}} v_{\text{rel}} \rangle \simeq 0.5 \text{ mb}$  as an estimate for the average over all hadrons (note that mass thresholds, the relative velocity  $v_{\text{rel}} < 1$  and an average over the thermal motion significantly reduce the average value for  $\sigma^{\text{diss}} v_{\text{rel}}$ , compared to the relatively narrow maxima in the cross section plots), yielding  $\Gamma_{\Psi}^{\text{HG}} \simeq 8 \text{ MeV}$ . This is significantly smaller

than the estimates for the QGP-induced suppression shown in the right panel of Fig. 17, even close to  $T_c$ . We can therefore expect that the anomalous suppression of the  $J/\psi$  in heavy-ion collisions is very small (and even less for the  $\Upsilon$ ). However, the situation may be quite different for excited charmonia,  $\psi'$  and  $\chi_c$ , which contribute “indirectly” to  $J/\psi$  production via late decays after freezeout (“feed-down”). Unfortunately, much less is known about hadronic dissociation of  $\psi'$  and  $\chi_c$  states.

## 2.5 Insights from Plasma Physics

In developing a theoretical approach to heavy quarkonia as messengers of the deconfinement and/or hadronization transition of a quark-gluon plasma as formed in a heavy-ion collision, one should aim at a unifying description where hadrons appear as bound states (clusters) of quarks and gluons. The situation is reminiscent of the problem of two-particle states in QED plasmas where a well-developed theory in the framework of the Green function technique exists. These methods have been widely elaborated for the case of the hydrogen plasma, where the electrons and protons as the elementary constituents can form hydrogen atoms as bound states of the attractive Coulomb interaction. The problem is tractable analytically for the isolated two-particle system, with a discrete energy spectrum of bound states and a continuous spectrum of scattering states. More complex bound states, such as molecular hydrogen can also be formed.

In a many-particle system, the problem of bound state formation needs to account for medium effects. They give contributions to a plasma Hamiltonian,

$$H^{\text{pl}} = H^{\text{Hartree}} + H^{\text{Fock}} + H^{\text{Pauli}} + H^{\text{MW}} + H^{\text{Debye}} + H^{\text{pp}} + H^{\text{vdW}} + \dots, \quad (27)$$

where the first three terms - the Hartree and Fock energies of one-particle states and the Pauli blocking for the two-particle states - are of first order in the interaction and represent the mean-field approximation. The following two terms of the plasma Hamiltonian are the Montroll-Ward (MW) term accounting for the dynamical screening of the interaction in the self-energy, and the dynamical screening (Debye) of the interaction between the bound particles. These contributions are related to the polarization function and are of particular interest for plasmas due to the long-range character of the Coulomb interaction. In a consistent description, both terms should be treated simultaneously. The last two contributions to the plasma Hamiltonian are of second order in the fugacity (particle density): the polarization potential (pp), describing the interaction of a bound state with free charge carriers, and the van der Waals (vdW) interaction, accounting for the impact of correlations (including bound states) in the medium on the two-particle system under consideration [18, 72].

Approximations to medium effects in the self-energy and the effective interaction kernel have to be made in a consistent way, resulting in predictions for the modification of one- and two-particle states. On this basis, the kinetics of bound-state formation and breakup processes can be described, establishing the ionization equilibrium under given thermodynamic conditions [130], see, e.g., Eq. (22). Coulomb systems similar to the hydrogen plasma are electron-hole plasmas in semiconductors [131], where excitons and bi-excitons play the role of the atoms and molecules. Other systems which have been widely studied are expanded fluids like alkali plasmas or noble gas plasmas [18]. Applications of the plasma physics concepts for cluster formation and Mott effect to the rather short-ranged strong interactions have been given, e.g., in Refs. [132, 133] for nuclear matter and in Refs. [134, 135] for quark matter.

In this Section, we would like to discuss basic insights from the investigations of bound-state formation in electromagnetic plasmas, as far as they might concern our discussion of heavy-quarkonia formation in hot and dense matter. Before going more into the details, let us give a brief overview. The bound-state energy remains rather inert to changes of the medium since the self-energy and interaction effects partially compensate each other to lowest order in density. The small size of the bound states plays an important role in this respect. The compensation is not operative for continuum states which

are influenced by self-energy effects only, usually resulting in a lowering of the in-medium ionization threshold. This often leads to a strong enhancement of the transition rates from bound to free states, inducing a sequential “melting” of different bound-state excitation levels into the continuum of scattering states for certain critical plasma parameters (Mott effect [17]), until eventually the ground state becomes unbound.

The theory of plasma correlations has also been developed for strongly non-ideal systems, where the formation of clusters in the medium needs to be taken into account. This situation is reminiscent of a hadronizing quark-gluon plasma; we will therefore refer to cluster expansion techniques as the theoretical basis.

**Bethe-Salpeter equation and plasma Hamiltonian.** A systematic approach to the description of bound states in plasmas starts from the Bethe-Salpeter equation (BSE) for the thermodynamic (Matsubara-) two-particle Green function of particles  $a$  and  $b$  (in analogy to Eq. (18) in Sec. 2.2),

$$G_{ab} = G_{ab}^0 + G_{ab}^0 K_{ab} G_{ab} = G_{ab}^0 + G_{ab}^0 T_{ab} G_{ab}^0, \quad (28)$$

which is equivalent to the use of the two-particle  $T$ -matrix  $T_{ab}$ . The 2-body equation has to be solved in conjunction with the Dyson equation for the full one-particle Green function,

$$G_a = G_a^0 + G_a^0 \Sigma_a G_a, \quad (29)$$

defined by the dynamical self-energy  $\Sigma_a(p, \omega)$  and the free one-particle Green function  $G_a^0(p, \omega) = [\omega - \varepsilon_a(p)]^{-1}$  for a particle of species  $a$  with the dispersion relation  $\varepsilon_a(p) = \sqrt{p^2 + m_a^2} \approx m_a + p^2/(2m_a)$ , see Fig. 24.

Figure 24: The coupled one- and two-particle problem in the medium. Dyson equation (left) and Bethe-Salpeter equation (right) need to be solved in consistent (conserving) approximations for self-energy ( $\Sigma$ ) and interaction kernel ( $K$ ).

The BSE contains the information about the spectrum of two-particle bound as well as scattering states in the plasma. A proper formulation of the plasma effects on the two-particle spectrum is essential to understand why bound and scattering states are influenced in a different way by the surrounding medium, leading to the Mott-effect for bound states. We here give the essence of a detailed discussion as presented in Ref. [72].

The homogeneous BSE associated with Eq. (28) can be cast into a form of an effective Schrödinger equation for the wave function  $\psi_{ab}(p_1, p_2, z)$  of two-particle states in the medium [131],

$$\sum_q \{[\varepsilon_a(p_1) + \varepsilon_b(p_2) - z] \delta_{q,0} - V_{ab}(q)\} \psi_{ab}(p_1 + q, p_2 - q, z) = \sum_q H_{ab}^{\text{pl}}(p_1, p_2, q, z) \psi_{ab}(p_1 + q, p_2 - q, z), \quad (30)$$

where  $a, b$  denote a pair of particles with 3-momenta  $p_1$  and  $p_2$  which transfer a 3-momentum  $2q$  in their free-space interaction  $V_{ab}(q)$ , and  $z$  is a complex two-particle energy variable. The in-medium effects described by Eq. (30) have been singled out in the definition of a plasma Hamiltonian, containing all modifications beyond the two-body problem in free space [72, 131],

$$\begin{aligned} H_{ab}^{\text{pl}}(p_1, p_2, q, z) = & \underbrace{V_{ab}(q) [N_{ab}(p_1, p_2) - 1]}_{\text{(i) Pauli blocking}} - \underbrace{\sum_{q'} V_{ab}(q') [N_{ab}(p_1 + q', p_2 - q') - 1] \delta_{q,0}}_{\text{(ii) Exchange self-energy}} \\ & + \underbrace{\Delta V_{ab}(p_1, p_2, q, z) N_{ab}(p_1, p_2)}_{\text{(iii) Dynamically screened potential}} - \underbrace{\sum_{q'} \Delta V_{ab}(p_1, p_2, q', z) N_{ab}(p_1 + q', p_2 - q') \delta_{q,0}}_{\text{(iv) Dynamical self-energy}}. \end{aligned} \quad (31)$$

Here,  $\Delta V_{ab}(p_1, p_2, q, z) = K_{ab}(p_1, p_2, q, z) - V_{ab}(q)$  stands for the in-medium modification of the bare interaction potential to a dynamically screened interaction kernel  $K_{ab}(p_1, p_2, q, z)$ . The effects of phase space occupation are encoded in the function  $N_{ab}(p_1, p_2)$ , which for the case of an uncorrelated fermionic medium takes the form of the Pauli blocking factor  $N_{ab}(p_1, p_2) = 1 - f_a(p_1) - f_b(p_2)$ , where  $f_a(p) = \{\exp[(\varepsilon_a(p) - \mu_a)/T] + 1\}^{-1}$  is the Fermi distribution and  $\mu_a$  the chemical potential of species  $a$ ; cf. the factors  $\hat{f}^{Q\bar{Q}}$  in Eq. (17). Eq. (30) is a generalization of the two-particle Schrödinger equation, where the left-hand side describes the isolated two-particle problem while many-body effects due to the surrounding medium are given on the right-hand side. The in-medium effects denoted in the plasma Hamiltonian (27) can be obtained from the one derived in the Bethe-Salpeter approach (31) upon proper choice of the interaction kernel  $K_{ab}$  so that Eq. (27) appears as a special case of Eq. (31).

The influence of the plasma Hamiltonian on the spectrum of bound and scattering states can be qualitatively discussed in perturbation theory. Since bound states are localized in coordinate space, their momentum-space wave functions extend over a finite range  $\Lambda$  and we may assume them to be  $q$ -independent,  $\psi_{ab}(p_1 + q, p_2 - q, z = E_{nl}) \approx \psi_{ab}(p_1, p_2, z = E_{nl})$ , for small momentum transfer,  $q < \Lambda$ , and to vanish otherwise ( $E_{nl}$  energy of the bound state with quantum numbers  $n$  and  $l$ ). Assuming further a flat momentum dependence of the Pauli blocking factors  $N_{ab}(p_1 + q, p_2 - q) \approx N_{ab}(p_1, p_2)$  for small  $q$  where the interaction is strong, we obtain a cancellation of the Pauli blocking term (i) by the exchange self-energy (ii), and of the dynamically screened potential (iii) by the dynamical self-energy (iv). Therefore, the bound-state energy remains largely unmodified by medium effects. For scattering states which are extended in coordinate space and can be represented by a  $\delta$ -function in momentum space, the above cancellations do not apply and a shift of the two-particle continuum threshold results. For this mechanism to work it is important that approximation schemes for the self-energy and the interaction kernel are consistent as, e.g., in the conserving scheme of  $\Phi$ -derivable theories [136].

Summarizing the discussion of the plasma Hamiltonian, we state that bound-state energies remain unshifted to lowest order in the charge carrier density while the threshold for the continuum of scattering states is lowered. This formally implies a reduction of the binding energy if the latter is identified with the difference between the 2-particle threshold and the bound-state energy,  $\varepsilon_B = 2m_a + m_b - E_{nl}$ . The intersection points of bound state energies and continuum threshold define the Mott densities (and temperatures) for bound-state dissociation.

When applying this approach to heavy quarkonia in a medium where heavy quarks (either free or bound in heavy hadrons) are rare, then  $N_{ab} = 1$  so that both, (i) and (ii), can be safely neglected. The effects (iii) and (iv) originate from the dynamical coupling of the two-particle state to collective excitations (plasmons) in the medium. In the screened-potential approximation, the interaction kernel is represented by

$$\begin{aligned} V_{ab}^S(p_1 p_2, q, \omega) &= V_{ab}^S(q, \omega) \delta_{P, p_1 + p_2} \delta_{2q, p_1 - p_2} \\ V_{ab}^S(q, \omega) &= V_{ab}(q) + V_{ab}(q) \Pi_{ab}(q, \omega) V_{ab}^S(q, \omega) = V_{ab}(q) [1 - \Pi_{ab}(q, \omega) V_{ab}(q)]^{-1}, \end{aligned} \quad (32)$$

with the total momentum  $P$ , momentum transfer  $2q$  and energy transfer  $\omega$  in the two-particle system. The most frequently used approximation for the polarization function,  $\Pi_{ab}(q, \omega)$ , or for the equivalent dielectric function,  $\varepsilon_{ab}(q, \omega) = 1 - \Pi_{ab}(q, \omega) V_{ab}(q)$ , is the random phase approximation (RPA). In the next two paragraphs we discuss the static, long wavelength limit of the RPA and its generalization in a clustered medium.

**Example 1: Statically screened Coulomb potential.** The systematic account of the modification of the interaction potential between charged particles  $a$  and  $b$  through polarization of the medium is taken into account in the dynamical polarization function,  $\Pi_{ab}(q, \omega)$ , which in RPA reads [72]

$$\Pi_{ab}^{\text{RPA}}(q, \omega) = 2\delta_{ab} \int \frac{d^3p}{(2\pi)^3} \frac{f_a(E_p^a) - f_a(E_{p-q}^a)}{E_p^a - E_{p-q}^a - \omega}. \quad (33)$$

For the Coulomb interaction, corresponding to the exchange of a massless vector boson, the potential is obtained from the longitudinal propagator in Coulomb gauge,  $V_{ab}(q) = e_a e_b / q^2$ . For a recent discussion in the context of heavy-quarkonium correlators and potentials see, e.g., Refs. [81, 82, 59]. Due to the large masses of the constituents in the heavy-quarkonium system, one may use a Born-Oppenheimer expansion to replace the dynamically screened interaction by its static ( $\omega = 0$ ) and long-wavelength ( $q \rightarrow 0$ ) limit. For nondegenerate systems the distribution functions are Boltzmann distributions and their difference can be expanded as

$$f_a(E_p^a) - f_a(E_{p-q}^a) = e^{-E_p^a/T} \left(1 - e^{-(E_p^a - E_{p-q}^a)/T}\right) \approx -f_a(E_p^a)(E_p^a - E_{p-q}^a)/T, \quad (34)$$

so that the energy denominator gets compensated and the polarization function becomes

$$\Pi_{ab}^{\text{RPA}}(q, 0) = -2 \frac{\delta_{ab}}{T} \int \frac{d^3 p}{(2\pi)^3} f_a(E_p^a) = -\delta_{ab} \frac{n_a(T)}{T}. \quad (35)$$

The corresponding dielectric function  $\varepsilon_{ab}^{\text{RPA}}(q, \omega)$  takes the form

$$\lim_{q \rightarrow 0} \varepsilon^{\text{RPA}}(q, 0) = 1 + \frac{\mu_D^2}{q^2}, \quad \mu_D^2 = \frac{1}{T} \sum_a e_a^2 n_a(T). \quad (36)$$

The screened Coulomb potential in this approximation is therefore  $V_{ab}^S(q) = V_{ab}(q)/\varepsilon^{\text{RPA}}(q, 0) = e_a e_b / (q^2 + \mu_D^2)$ . In this “classical” example of the statically screened Coulomb interaction, the contribution to the plasma Hamiltonian is real and in coordinate representation given by

$$\Delta V_{ab}(r) = -\frac{\alpha}{r} (e^{-\mu_D r} - 1) \approx \alpha \mu_D - \frac{\alpha}{2} \mu_D^2 r, \quad (37)$$

where  $\alpha = e^2/(4\pi)$  is the fine structure constant. For the change in the Hartree self-energy of one-particle states due to Debye screening we can perform an estimate in momentum space,

$$\Sigma_a = \frac{4\pi\alpha}{(2s_a + 1)} \int \frac{d^3 q}{(2\pi)^3} \left[ \frac{1}{q^2 + \mu_D^2} - \frac{1}{q^2} \right] f_a(E_q^a) \approx -\frac{\alpha \mu_D^2}{\pi} \int_0^\infty \frac{dq}{q^2 + \mu_D^2} = -\frac{\alpha \mu_D}{2}, \quad (38)$$

which compensates to lowest order in the density the shift of the bound-state energy levels due to the screening of the interaction (37),

$$\Delta \epsilon_{B,ab} \approx \alpha \mu_D = \mathcal{O}(\sqrt{n a_{B,0}^3}), \quad (39)$$

( $a_{B,0}$ : Bohr radius in vacuum) so that [72, 137]

$$\Delta E_{nl} \approx -\frac{\alpha}{2} \mu_D^2 \langle r \rangle_{nl} = \mathcal{O}(n a_{B,0}^3). \quad (40)$$

The Debye mass,  $\mu_D$ , is equivalent to the inverse of the Debye radius  $r_D$  characterizing the effective range of the interaction, and depends on the square root of the density  $n(T)$  of charge carriers. It is this different response of bound states and scattering continuum to an increase of density and temperature in the medium which leads to the Mott effect for electrons in an insulator [17, 18]: bound states of the Debye potential can only exist when the Debye radius is larger than  $r_{D,\text{Mott}} = 0.84 a_{B,0}$  [138]. This entails that above a certain density even the ground-state electrons become unbound and form a conduction band, resulting in an insulator-metal transition (also called Mott-transition). Further details concerning this example can be found in Ref. [139].

In complete analogy to the electronic Mott effect it is expected that in hadronic matter at high density the hadrons - as bound states of quarks - undergo a Mott transition which results in a

phase transition from the color-insulating phase (hadronic matter) to a color-conducting or even color-superconducting phase (deconfined quark matter). This applies to light hadrons as well as to heavy quarkonia, whereby due to the different scales of Bohr radii the Mott dissociation of heavy quarkonia is expected to occur at higher densities than for light hadrons. In some approaches quark self-energy effects are neglected and one is only left with the medium effect due to a statically screened potential. Consequently, in such a picture the continuum edge of the scattering states remains unshifted and, due to the lack of a compensating effect, the effective interaction entails an appreciable medium dependence of the bound-state energies (masses). For the electron-hole plasma in highly excited semiconductors it could be shown experimentally, however, that the compensation picture is correct and the bound state energies remain almost unshifted [140]. In the context of heavy quarkonia in the QGP this could, at least qualitatively, provide a natural explanation of the approximate constancy of the Euclidean correlator ratios found in thermal lattice QCD.

One may of course absorb the self-energy effects into a redefinition of the effective interaction, by adding a homogeneous mean-field contribution. This is equivalent to the use of the Ecker-Weitzel potential [141],

$$V_{\text{Ecker-Weitzel}}(r) = -\frac{\alpha}{r}e^{-\mu_D r} - \alpha\mu_D. \quad (41)$$

Recent investigations of the screening problem in the context of Debye-Hückel theory [142] and  $Q\bar{Q}$  correlators [59, 82] have obtained this continuum shift  $(-\alpha\mu_D)$  as a homogeneous background field contribution. According to the above lesson from plasma physics, however, this contribution should be attributed to the self-energy of the constituents rather than to the interaction kernel, since it determines the shift of the continuum edge (cf. Eq. (21)).

**Example 2: Heavy quarkonia in a relativistic quark plasma.** We consider the problem of a heavy quark-antiquark pair interacting via (an ansatz for) the statically screened Cornell potential (12) in a relativistic quark plasma. The thermodynamics of this medium is described in good agreement with lattice QCD data by a Nambu-Jona-Lasinio model coupled to a Polyakov-loop potential (PNJL model [143] which allows us to estimate the Debye mass,  $\mu_D(T)$ , by evaluating the RPA polarization function, Eq. (33), for  $N_c$  colors and  $N_f$  flavors of massless quarks with  $E_p^a = |p|$  as

$$\Pi_{ab}^{\text{RPA}}(q \rightarrow 0, 0) = 2\delta_{ab} \int \frac{d^3p}{(2\pi)^3} \frac{df_a(E_p^a)}{dE_p^a} = -2\delta_{ab} \int_0^\infty \frac{dp}{\pi^2} p f_\Phi(p) = -\frac{\delta_{ab}}{6\pi^2} I(\Phi) T^2. \quad (42)$$

Here,  $I(\Phi) = (12/\pi^2) \int_0^\infty dx x f_\Phi(x)$  and  $f_\Phi(x) = [\Phi(1 + 2e^{-x})e^{-x} + e^{-3x}]/[1 + 3\Phi(1 + e^{-x})e^{-x} + e^{-3x}]$  is the generalized quark distribution function [144] which in the case of a deconfined medium ( $\Phi = 1$ ) is just the Fermi function, yielding  $I(1) = 1$ . In the deconfinement transition region, where  $0 < \Phi < 1$ , quark excitations are strongly suppressed, e.g.,  $I(0) = 1/9$ . Taking as the bare potential a color singlet one-gluon exchange  $V(q) = -4\pi\alpha_s/q^2$ ,  $\alpha_s = g^2/(4\pi)$ , the Fourier transform of the Debye potential,  $V^S(r) = -\alpha \exp(-\mu_D(T)r)/r$ , results as a statically screened potential with the Debye mass  $\mu_D(T) = 4\pi\alpha_s I(\Phi) T^2$ . The Hartree self-energy for heavy quarks in a PNJL quark plasma is then given by Eq. (38).

In the spirit of Eq. (38), one can evaluate the Hartree shift due to the screened confinement part,  $V_{\text{conf}}^S(r) = (\sigma/\mu_D)(1 - \exp(-\mu_D r))$ , of the potential (12) and show that it vanishes,  $\Sigma_{\text{conf}} = 0$ .

In Fig. 25 we show the temperature dependence of the two-particle energies for heavy quarkonia as a solution of the effective Schrödinger equation

$$H^{\text{Pl}}(r; T)\phi_{nl}(r; T) = E_{nl}(T)\phi_{nl}(r; T) \quad (43)$$

for the plasma Hamiltonian

$$H^{\text{Pl}}(r; T) = 2m_Q - \alpha\mu_D(T) - \frac{\vec{\nabla}^2}{m_Q} + V_{Q\bar{Q}}(r; T), \quad (44)$$

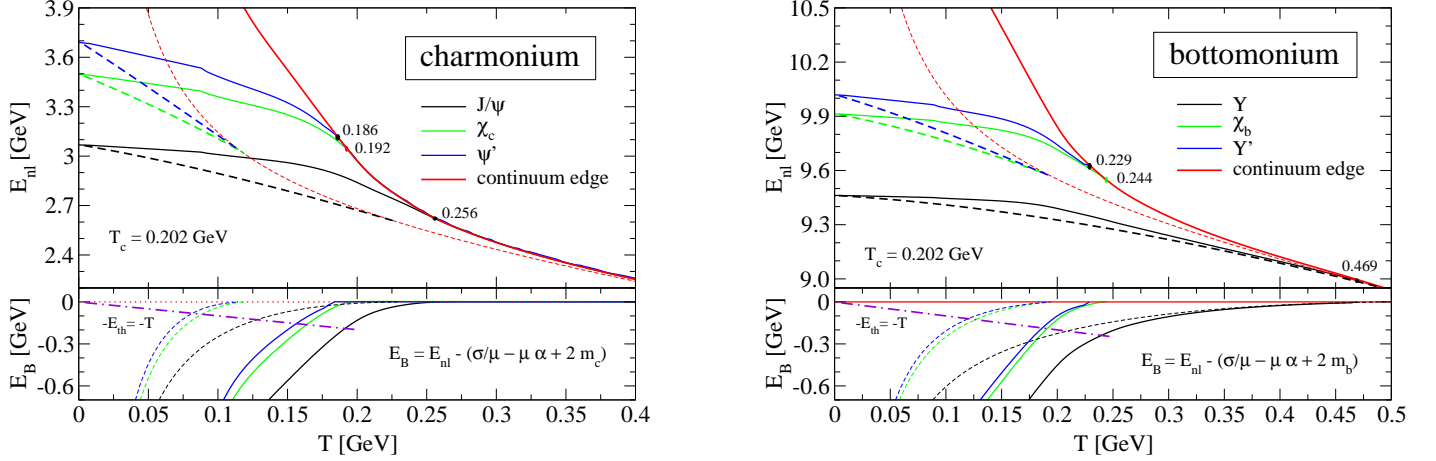


Figure 25: Two-particle energies of charmonia (left panel) and bottomonia (right panel) in a statically screened potential, from Ref. [145]. The full results of the PNJL model (solid lines) are compared to results without the coupling to the Polyakov loop potential (dashed lines).

as evaluated recently in Ref. [145].

We can draw three conclusions from this example: (1) Due to the suppression of light-quark excitations by the confining effects of the Polyakov loop the lowering of the continuum edge and the merging of two-particle bound states with it (Mott effect) occur at higher temperatures when compared to the simple NJL model case; (2) The inclusion of the Hartree selfenergy for heavy quarks in the plasma Hamiltonian, Eq. (44), leads to a compensation and even overcompensation of the upwards shift of quarkonia masses obtained from a solution of the Schrödinger equation with the naive Hamiltonian, Eq. (13); see, e.g., upper left panel of Fig. 12 or upper right panel Fig. 14 for the effect of neglecting the downwards shift of the continuum due to the heavy quark self-energy on the temperature dependence of the quarkonium spectrum. The compensation of a decreasing  $m_c^*$  and decreasing  $\varepsilon_B$  indeed play an important role in understanding the rather constant euclidean correlator ratios from lattice QCD. (3) From Fig. 25 one can also read off the in-medium lowering of the dissociation threshold  $k_0^{\text{diss}} = \varepsilon_B$ , which is the energy difference between the considered bound-state level and the continuum edge. This quantity is indifferent to the inclusion of a rigid self-energy shift. The lowering of  $k_0^{\text{diss}}$  with increasing density and/or temperature leads to a strong increase in the quarkonium breakup cross section, Eq. (25), by thermal impact, and to bound-state dissociation even before the binding energies vanish at the critical Mott densities/temperatures for the corresponding states. To estimate this effect we show in the lower panels of the graphs in Fig. 25 the thermal energy  $E_{\text{th}} = T$  together with the in-medium binding energy  $E_B \equiv -\varepsilon_B$ . The temperatures for the onset of bound-state dissociation by thermal collisions with medium particles are obtained from the crossing points of these curves which are considerably lower than the naive Mott temperatures corresponding to vanishing binding energies.

For the development of a comprehensive approach to heavy quarkonia in hadronizing hot/dense QCD matter another insight from plasma physics may be of relevance and will be discussed next: the effect of strong correlations (bound states) in the bulk of the medium. To this end, the bound states will be treated like a new species occurring in the system. Accordingly, additional diagrams have to be taken into account which arise from a cluster expansion of the interaction kernel  $K_{ab}$  and the corresponding self-energy  $\Sigma_a$ , see Figs. 26-28. In the plasma Hamiltonian,  $H^{\text{Pl}}$ , this leads to a generalization of the self-energy contributions (cluster Hartree-Fock approximation), the distribution functions in the Pauli-blocking factors and the dynamical screening (cluster-RPA). The van-der-Waals interaction in Eq. (27) appears naturally as a contribution to the cluster expansion, describing polarization effects due to bound states in the medium.

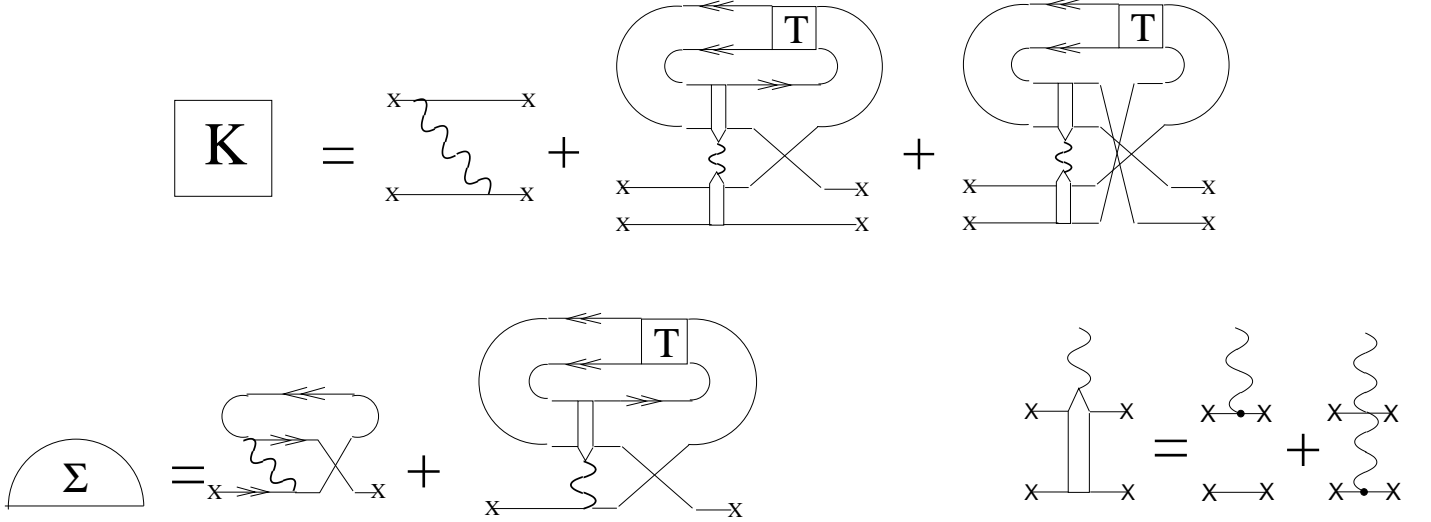


Figure 26: Cluster expansion for the interaction kernel for the two-particle problem in a strongly correlated medium (upper equation) and the corresponding self-energy (lower left equation) with a dipole ansatz for the vertex (lower right equation).

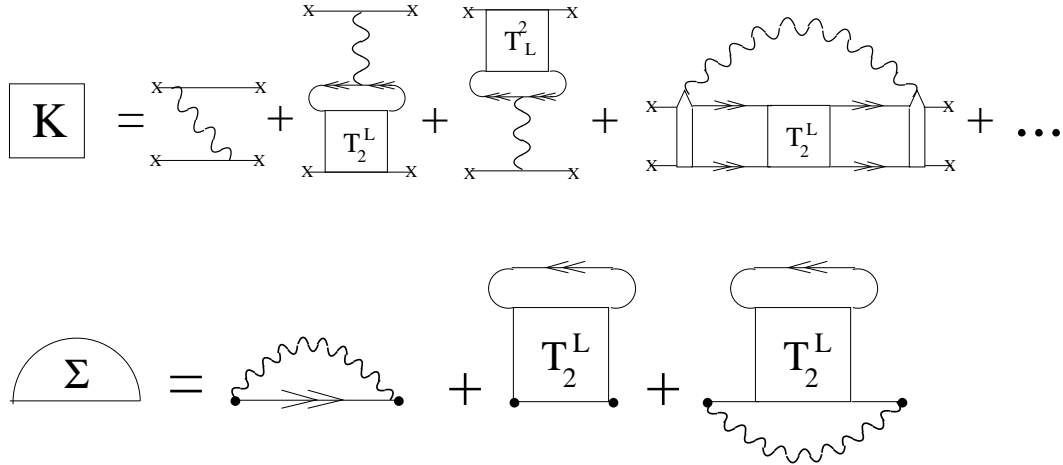


Figure 27: Alternative way of drawing the diagrams for the cluster expansion of the interaction kernel and the corresponding self-energy of Fig. 26 in a form familiar in plasma and nuclear physics;  $T_2^L$  denotes the 2-body  $T$ -matrix computed in ladder approximation.

**Two-particle states in the medium: Cluster expansion.** In the vicinity of the plasma phase transition, correlations play an important role, and their proper accounting requires rather sophisticated theoretical methods such as cluster expansion techniques. For the problem of charmonium in dense hadronic matter at the deconfinement transition, i.e., in the strong-coupling case, we suggest a systematic Born series expansion of collisions with free and bound states in the surrounding matter so that all terms linear in the density of free particles and bound states are taken into account.

We here describe the cluster expansion in terms of its diagrammatic expressions for the interaction kernel and the corresponding self-energy. The 1<sup>st</sup> Born approximation diagrams of this expansion are given in Fig. 26, see also the monograph [72]. The wavy lines denote the dynamically screened interaction  $V_{ab}^S$ , which in a strongly correlated plasma receives contributions from the polarization of the medium beyond the RPA, denoted as generalized (cluster-) RPA in Fig. 28 [146]. Bound and scattering states are described consistently in the two-particle  $T$ -matrices. For a generalization to higher  $n$ -particle

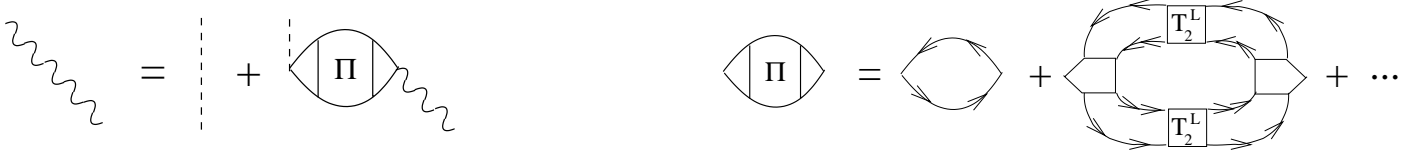


Figure 28: Left panel: The dynamically screened interaction potential,  $V_{ab}^S(\omega, q)$  (wavy line), determined by the bare potential (dashed line) and the polarization function,  $\Pi_{ab}(\omega, q)$ . Right panel: Cluster expansion for the generalized RPA, where in addition to free particles (RPA) also two-particle states (cluster-RPA) contribute to the polarizability of the medium [146].



Figure 29: Contributions to the dynamical self-energy of a two-particle system in a correlated medium at  $2^{nd}$  Born order. Left panel: impact by two-particle states without constituent exchange (van-der-Waals or dipole-dipole interaction). Right panel: constituent-rearrangement collisions (string-flip process), from Ref. [150], see also Ref. [151].

correlations, see Refs. [133, 147, 72]. The diagrams containing  $T$ -matrices do not contribute to the charmonium spectrum as long as the densities of the charmed quarks and of charmed hadrons in the medium are negligible. This is the situation expected for FAIR, SPS and RHIC energies, but for the expected copious charm production at LHC these terms may become significant.

At the  $2^{nd}$  Born order, we distinguish two classes of collisions with light clusters (hadrons) that can give rise to spectral broadening of the charmonia. The first class concerns hadron impact without quark rearrangement inducing transitions to excited states, shown in the left panel of Fig. 29. These processes have been considered for charmonium-hadron interactions within the operator product expansion techniques following Peskin and Bhanot [88, 89], see Refs. [148, 149]. The result is a deformation of the charmonium spectrum under conservation of the spectral weight integrated over all charmonia states. In the second class are quark rearrangement (string-flip) processes, as indicated in the right panel of Fig. 29. They induce transitions to open-charm hadrons which are also responsible for charmonium dissociation in hadronic matter, cf. Sec. 2.4.

**Example 3: String-flip model of charmonium dissociation.** As a third example for utilizing insights from plasma physics we discuss charmonium dissociation within the string-flip model of quark matter [134, 135, 152, 153]. In this model string-type color interactions between quarks are saturated within the sphere of nearest neighbors so that in a dense system of overlapping quark-antiquark pairs frequent string-flip processes occur to drive the system into its minimal energy configuration at any time. The microscopic evaluation of those processes requires diagrams as the one shown in the right panel of Fig. 29 involving at least four quarks. Evaluating the imaginary part of this diagram, in connection with the optical theorem ( $\sigma_{\text{diss}} \propto \text{Im } T$ ), gives access to the heavy-quarkonium dissociation rate in hadronic matter, cf. Eq. (26) in the previous section 2.4. When considering a heavy quark-antiquark pair in dense

matter with negligible heavy-flavor fraction, the Pauli blocking and exchange self-energy contributions are negligible, but the strong correlations with light quarks of complementary color within the nearest neighbor sphere will result in a mean-field self-energy shift (Hartree shift  $\Delta^H$ ) for all quarks [154] which determines the shift of the continuum edge. Because of the compensation in the Bethe-Salpeter kernel between the effects of screening of the interaction and self-energy shifts calculated with it (see discussion above), it is suggested that to lowest order the bound-state energies remain unshifted when increasing the temperature and/or density of the medium. In contrast to the first example of Debye screening of long-range Coulombic interactions, the screening mechanism in the string flip model is color saturation within nearest neighbors, applicable for strong, short-range interactions as appropriate for the case of the sQGP at RHIC or dense systems at CBM-FAIR. The resulting two-particle energy spectrum for charmonium and bottomonium states is discussed in Ref. [93], where the static screening picture is compared to the string-flip picture. Within the latter the in-medium lowering of the dissociation threshold  $k_0^{\text{diss}}$  is directly given by the behavior of the continuum edge, i.e. by the Hartree shift, as known for rate coefficients in strongly coupled plasmas [130].

### 3 Quarkonia in Heavy-Ion Collisions

The utilization of heavy quarkonia as a probe of the medium created in heavy-ion reactions has to rely on the analysis of their final number and momentum spectra. Since the equilibration of quarkonia is generally not warranted, the interface between their in-medium properties and observables is usually based on transport approaches (Sec. 3.1). If the bulk medium is in local thermal equilibrium, the in-medium properties (as elaborated in the previous Section) enter in the form of relaxation times (dissociation rates) and asymptotic limits for the yields (equilibrium abundances). With realistic initial conditions, usually inferred from  $p$ - $A$  collisions (Sec. 3.2), phenomenological studies over a wide range of energies can be performed (Sec. 3.3).

#### 3.1 Charmonium Transport

The evolution of the abundance and spectrum of a quarkonium state,  $\Psi$ , in a hot and dense fireball can be tracked via its phase space distribution,  $f_\Psi$ , satisfying a transport equation of the form

$$p^\mu \partial_\mu f_\Psi(\vec{r}, t; \vec{p}) = -\omega_p \Gamma_\Psi(\vec{r}, t; \vec{p}) f_\Psi(\vec{r}, t; \vec{p}) + \omega_p \beta_\Psi(\vec{r}, t; \vec{p}) . \quad (45)$$

Here,  $\Gamma_\Psi$  denotes the dissociation width discussed in Secs. 2.3 and 2.4,  $\beta_\Psi$  the gain term responsible for regeneration (discussed in more detail below), and  $p_0 = \omega_p = (m_\Psi^2 + \vec{p}^2)^{1/2}$  the on-shell energy of state  $\Psi$  implying that a well-defined quasiparticle state exists (mean-field terms have been neglected which is justified if mass corrections are small). The right-hand-side of this equation is the collision term which accounts for both dissociation and formation reactions (possibly including transitions between different charmonium states). Detailed balance (and the correct equilibrium limit) requires that both terms include the same reaction mechanisms.

Let us first discuss the situation where the gain term in the transport equation can be neglected; this can be realized in scenarios (or evolution phases) where either no charmonium states can be formed (are not supported in the medium) and/or the actual charmonium number is much larger than the equilibrium abundance in connection with relatively small reaction rates. Under these circumstances, the evolution of the charmonium number is given by a sequence of suppression stages for which the solution of the rate equation may be schematically written in terms of a (3-momentum dependent) survival probability (or suppression factor)

$$S_\Psi = S_{\text{HG}} S_{\text{QGP}} S_{\text{nuc}}$$

$$\simeq \exp \left( - \int_{T_c}^{T_{fo}} \Gamma_{\text{HG}}(T) \frac{dT}{\dot{T}} \right) \exp \left( - \int_{T_0}^{T_c} \Gamma_{\text{QGP}}(T) \frac{dT}{\dot{T}} \right) \exp (-n_N \sigma_{\text{abs}} L) . \quad (46)$$

In this approximation the key ingredients are the inelastic reaction rates in hadron gas (HG) and QGP phases, as well as primordial nuclear absorption (which will be discussed in more detail in the following Section, 3.2). If the latter can be accurately determined from  $p$ - $A$  data, and if the hadronic suppression is small,  $S_\Psi$  would provide direct information on the (temperature-dependent) inelastic reaction rate in the QGP (recall that the complete melting of a charmonium state (e.g. due to color screening) may be considered as the limit  $\Gamma_\Psi \rightarrow \infty$ ). As discussed in the introduction, the suppression approach has been widely applied in the interpretation of SPS data on charmonium production in light- and heavy-ion reactions, encompassing a wide range of models for both the charmonium dissociation mechanisms (hadronic comovers [21, 22, 155, 156, 157], screening-based models [1, 30, 158], as well as thermal dissociation-rate calculations) and the evolution of the medium (transport, fireball and hydrodynamic simulations). An updated account of the state-of-affairs in this enterprise will be given in Sec. 3.3 below. The suppression factor, Eq. (46), encodes no notion of the charmonium masses, of their equilibrium number, nor of any coupling to the open-charm content in the system. These aspects, however, become essential upon inclusion of regeneration processes, i.e., the gain term in Eq. (45), as we will now discuss.

Early evaluations of secondary charmonium production in heavy-ion collisions were focusing on hadronic regeneration reactions in the hadronic [159] and mixed phases [160] under LHC conditions. In Refs. [41, 43, 161] (see, e.g., Ref. [162] for a recent update) the statistical hadronization model has been invoked assuming that charmonia thermally equilibrate (and diffuse into a homogeneous distribution) upon completion of the hadronization phase transition (on the hadronic side), without further modifications in their abundances in the subsequent hadronic phase. In terms of the rate equation (45) this implies that the thermal relaxation time (or inelastic width) of charmonia changes rather rapidly across the phase transition, which is not inconsistent with the microscopic calculations discussed in the previous two Sections (at least for the  $J/\psi$ ). It also implies that the open-charm states forming the charmonia have kinetically equilibrated. This assumption is less certain, with current estimates of the thermal relaxation time of charm quarks of around  $\tau_c^{\text{eq}} \simeq 5\text{-}7 \text{ fm}/c$  [163]. However, it is presently an open question by how much the  $J/\psi$  regeneration yield is affected by deviations of charm-quark distributions from thermal equilibrium. E.g., when comparing the limiting cases of either primordial spectra (i.e., no reinteractions) or a thermal source (+flow), a factor of  $\sim 3$  difference in the  $J/\psi$  yield in central Au-Au at RHIC has been found in the coalescence model of Ref. [164], while the variations in the transport model of Ref. [165] are smaller. In Ref. [161] it was additionally assumed that charm equilibrates chemically with the surrounding medium, so that the charmonium density is determined solely by its mass and the ambient temperature. With a hadronization temperature of  $T_c = 175 \text{ MeV}$ , a surprisingly good description of the  $J/\psi$ -over-pion ratio at the SPS was found. In Ref. [41] the assumption of chemical equilibration of charm-quarks was relaxed based on theoretical expectations [14, 166, 160] that  $c\bar{c}$  pair production is restricted to primordial  $N$ - $N$  collisions and frozen thereafter (available experimental data at RHIC [12] and SPS [13] support this assertion). Under these conditions, charmonium production at the hadronization transition corresponds to a coalescence of available charm and anticharm quarks. In thermal equilibrium, this leads to a charmonium density

$$n_\Psi^{\text{eq}}(m_\Psi; T, \gamma_c) = d_\Psi \gamma_c^2 \int \frac{d^3p}{(2\pi)^3} f_\Psi(\omega_p; T) , \quad (47)$$

where  $\gamma_{\bar{c}} = \gamma_c$  denote a (anti-) charm-quark fugacity (particle densities and numbers are denoted by  $n$  and  $N$ , respectively). In *relative* chemical equilibrium, the fugacity is determined by matching the number of charm-quark carriers to the total number,  $N_{c\bar{c}}$ , of  $c\bar{c}$  pairs in the system,

$$N_{c\bar{c}} = \frac{1}{2} N_{op} \frac{I_1(N_{op})}{I_0(N_{op})} + V_{FB} \sum_{\eta_c, J/\psi, \dots} n_\Psi^{\text{eq}}(T) , \quad (48)$$

where  $N_{op}$  denotes the number of all open-charm states in a fireball of volume  $V_{FB}$ . In a QGP, where the charm-quark number is carried by deconfined  $c$ -quarks, one has  $N_{op}=V_{FB}\gamma_c 2n_c^{\text{eq}}(m_c^*, T)$ , whereas in the HG,  $N_{op}=V_{FB}\gamma_c \sum_{\alpha} n_{\alpha}^{\text{eq}}(T, \mu_B)$  with  $\alpha$  running over all known charmed hadrons ( $D, \bar{D}, \Lambda_c, \dots$ ; note that for a finite baryon chemical potential,  $\mu_B > 0$ ,  $N_{\Lambda_c} \neq N_{\bar{\Lambda}_c}$  implying  $N_D \neq N_{\bar{D}}$ , etc.). The ratio of modified Bessel functions,  $I_1/I_0$ , in Eq. (48) approaches one for large  $N_{op}$ , but goes to  $0.5N_{op}$  for  $N_{op} \ll 1$ . In the latter limit,  $I_1/I_0$  can be interpreted as the probability of producing an extra (anti-) charm state, i.e., it enforces exact charm conservation in the canonical ensemble ( $c$  and  $\bar{c}$  can only be produced together) [43]. Note that the charmonium equilibrium limit does not depend on nuclear absorption or pre-equilibrium effects. The QGP evolution prior to hadronization is, however, imprinted on the collective properties of the statistically produced charmonia, i.e., their  $p_T$  spectra and elliptic flow [164, 165, 167]. If  $c\bar{c}$  coalescence occurs off equilibrium, the pertinent charmonium spectra reflect on the collective properties of the charm quarks, which, in turn, may serve as an additional means to identify a coalescence component in the spectra [164, 168]. In Refs. [44, 92], a 2-component model has been proposed where statistical production at hadronization is combined with primordially produced charmonia subject to suppression in the QGP, followed by hadronic suppression of both components.

Solutions of the transport equation (45) for  $J/\psi$  production in heavy-ion collisions under inclusion of the gain have first been evaluated in Ref. [42]; neglecting spatial dependencies in the temperature profile as well as in the  $J/\psi$  and open-charm densities, a simplified rate equation of the form

$$\frac{dN_{J/\psi}}{d\tau} = \lambda_F N_c n_{\bar{c}} - \lambda_D N_{J/\psi} n_g, \quad (49)$$

has been employed, very similar to Eq. (22). The reactivity  $\lambda_D = \langle v_{\text{rel}} \sigma_D \rangle$  is given in terms of the  $J/\psi$  dissociation cross section, for which the gluo-dissociation process, Eq. (24), has been used (and detailed balance for the formation reactivity,  $\lambda_F$ ). As emphasized in Ref. [42] (as well as in the statistical models with charm conservation [41, 43]), the  $J/\psi$  formation rate depends quadratically on the number,  $N_{c\bar{c}}$ , of (anti-) charm quarks in the system, rendering an accurate knowledge of the charm-production cross section an essential ingredient for reliable predictions of charmonium regeneration. In the equilibrium limit, the quadratic dependence is encoded in the squared fugacity factor in the charmonium densities, Eq. (47). As elaborated in Refs. [38, 173, 174], the equilibrium limit of the  $J/\psi$  abundance is sensitive to the masses of both open- and hidden-charm states. E.g., for fixed charmonium masses, a reduced charm-quark mass in the QGP (or reduced charm-hadron masses in the HG) implies a reduced  $\gamma_c$  for fixed  $N_{c\bar{c}}$ , which in turn leads to a smaller  $N_{\psi}^{\text{eq}}$ ; in other words, reduced (increased) open-charm masses make it thermodynamically more (less) favorable to allocate a given number of  $c\bar{c}$  pairs into open-charm states rather than into charmonia, see Fig. 30. This interplay has been quantitatively worked out in Ref. [38] based on the rate equation (22) with in-medium charm-quark and -hadron masses in QGP and HG phases, respectively. In particular,  $m_c^*(T_c) \simeq 1.6\text{--}1.7\text{ GeV}$  on the QGP side has been chosen to provide a continuous transition of  $\gamma_c$  into the hadronic phase at the (pseudo-) critical temperature (this range of  $c$ -quark masses is somewhat below the value of  $m_c^*(T_c) \simeq 1.8\text{ GeV}$  as inferred from the lattice correlator analysis using the internal energy as the heavy-quark potential, recall Fig. 13). As discussed in Sec. 2.2, the screening of lattice-based potentials leads to reduced binding energies, while the in-medium change in the  $J/\psi$  mass is expected to be rather small. The latter is rendered approximately constant by a decrease in the in-medium charm-quark mass  $m_c^*$ , as seems to be required in potential-model analyses of lattice QCD correlators (recall also the paragraph prior to Eq.(41)). In Ref. [97], the rate-equation approach of Ref. [38], which was restricted to inclusive charmonium production (i.e., for  $p=0$ ), has been extended to finite 3-momentum. The suppression part has been treated explicitly (including spatial dependencies, such as leakage effects) in an expanding fireball background, whereas the momentum dependence of the regeneration part was approximated with a blast-wave model (within the same fireball). The latter implies the underlying charm-quark spectra to be thermalized, at least in the relevant regime of low momentum [163, 175].

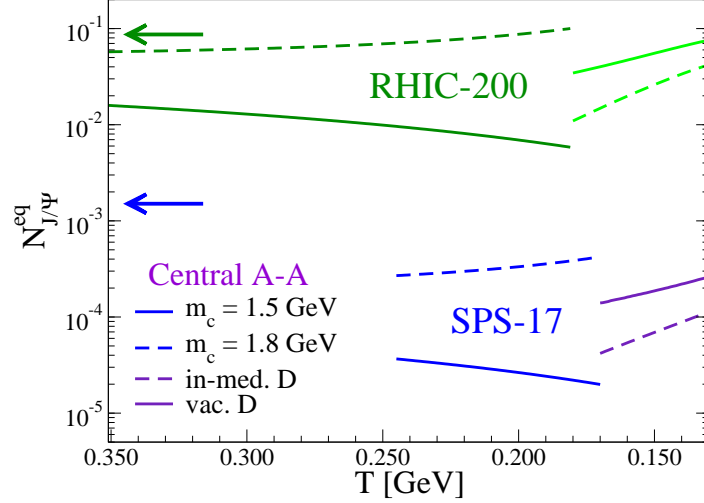


Figure 30: Equilibrium abundance of  $J/\psi$  mesons as a function of temperature in an isotropic fireball representative for central Pb-Pb and Au-Au collisions at SPS and RHIC, respectively [38]. While the variation in temperature is comparatively moderate, a large sensitivity of the equilibrium numbers with respect to the charm-quark (charm-hadron) masses in the QGP (HG) is found. The absolute numbers are based on open-charm cross sections in  $p$ - $p$  collisions of  $\sigma_{pp}^{c\bar{c}} = 570 \mu\text{b}$  and  $5.5 \mu\text{b}$  at RHIC and SPS, respectively (these values are roughly consistent with PHENIX measurements [12, 169] and compilations for fixed target energies [171, 172]), extrapolated to central A-A using binary-collision scaling, and for a rapidity interval of 3.6 units around midrapidity (corresponding to 2 thermal fireballs). The arrows to the left indicate the  $J/\psi$  abundance from primordial (hard) production.

A more advanced treatment of the gain term in the rate equation (45) within a hydrodynamically evolving background medium was carried out in Ref. [165] (see also Ref. [176]). Assuming the prevalence of the  $2 \leftrightarrow 2$  dissociation rate from gluon-dissociation,  $g + \Psi \leftrightarrow c + \bar{c}$ , the gain term takes the form

$$\beta_{\Psi}(\vec{p}_T; \vec{r}_t, \tau) = \frac{1}{2\omega_p} \int \frac{d^3k}{(2\pi)^3 2\omega_k} \frac{d^3p_c}{(2\pi)^3 2\omega_{p_c}} \frac{d^3p_{\bar{c}}}{(2\pi)^3 2\omega_{p_{\bar{c}}}} f^c(\vec{p}_c; \vec{r}_t, \tau) f^{\bar{c}}(\vec{p}_{\bar{c}}; \vec{r}_t, \tau) W_{c\bar{c}}^{g\Psi}(s) \Theta(T(\vec{r}_t, \tau) - T_c) \times (2\pi)^4 \delta^{(4)}(p + k - p_c - p_{\bar{c}}), \quad (50)$$

where the charmonium phase space has been restricted to the transverse plane at central rapidity ( $p_z=0=y$ ). With  $W_{g\Psi}^{c\bar{c}}(s) = \sigma_{g\Psi}^{\text{diss}} v_{\text{rel}}(2\omega_k 2\omega_p)$  representing the  $\Psi$  dissociation probability, the formation probability,  $W_{c\bar{c}}^{g\Psi}(s)$ , is inferred from detailed balance.  $\omega_k$ ,  $\omega_p$ ,  $\omega_{p_c}$  and  $\omega_{p_{\bar{c}}}$  denote the on-shell energies of gluon, charmonium, charm and anticharm quark, respectively, with charm(onium) masses of  $m_c=1.87 \text{ GeV}$  and  $m_{J/\psi}=3.1 \text{ GeV}$  (corresponding to a “vacuum” binding energy of  $\varepsilon_B^{J/\psi}=0.64 \text{ GeV}$ ). The  $\Theta(T-T_c)$  function in Eq. (50) restricts the inelastic processes to the QGP phase, with  $T_c=165 \text{ MeV}$  in Ref. [165]. Note that an explicit treatment of NLO dissociation processes in the regeneration term requires the evaluation of a 3-body initial state. The initial conditions for the charmonium distribution function,  $f_{\Psi}(\vec{p}; \vec{r}, \tau_0)$ , for its evolution in the thermally evolving medium are typically taken from a Glauber collision profile for production in primordial  $N$ - $N$  collisions, plus the effects of nuclear absorption. In the “pre-equilibrium” phase, i.e., for times earlier than the thermalization time,  $\tau_0$ , of the fireball, the gain term is switched off. While the production of a  $c\bar{c}$  pair is expected to occur on a short time scale,  $\tau_{c\bar{c}} \sim 1/2m_c^0 \approx 0.1 \text{ fm}/c$ , the development of the charmonium wave function in its rest frame requires a time duration on the order of its inverse binding energy,  $\tau_{\Psi} \sim 1/\varepsilon_B \approx 0.3 \text{ fm}/c$ . For a slowly moving  $J/\psi$ , this time is comparable or smaller to commonly assumed thermalization times of  $\tau_0 = 0.3\text{-}1 \text{ fm}/c$ . However, for  $J/\psi$ 's at large transverse momentum, the formation time in the fireball

frame is time-dilated by the (transverse) Lorentz factor  $\gamma_T = m_T/m$ , and therefore may well reach into the QGP phase, presumably reducing the suppression effects [157, 177, 178, 179, 180, 181] (in a naive picture, the  $c\bar{c}$  wave package is of smaller size than a fully formed bound state, thus reducing dissociation cross sections with thermal partons). The interplay of charmonium-formation and fireball-thermalization time scales will be further pronounced for in-medium reduced binding energies, as well as for excited charmonia (which even in vacuum have rather small binding energies).

An alternative approach to thermal descriptions of the bulk medium are microscopic transport models where the evolution of essentially all particle distributions is treated by numerical simulations of the Boltzmann equation. On the one hand, transport models have the important advantage that no explicit assumption on equilibration is required, which in particular eliminates the introduction of thermalization and freezeout times (or conditions)<sup>8</sup>. On the other hand, the treatment of phase transitions is more problematic than in thermal models, where pertinent aspects are readily encoded in the equation of state (EoS). The main input for charmonium interactions are  $2\leftrightarrow 2$  dissociation reactions (plus detailed balance), i.e., gluo-dissociation ( $g + \Psi \rightarrow c + \bar{c}$ ) in the partonic phase and meson dissociation ( $M + \Psi \rightarrow D + \bar{D}$  with  $M=\pi, K, \rho, \dots$ ) in the hadronic phase (sometimes augmented with elastic cross sections). Especially hadronic cross sections at low energy, as relevant for the typical reactions in the hadronic phase (corresponding to temperatures  $T < 200$  MeV), are currently beset with rather large theoretical uncertainties (and, in the case of meson dissociation, not accessible experimentally), recall Sec. 2.4. This problem applies, of course, to both transport and thermal descriptions of the expanding medium. Systematic comparisons of charmonium observables within complementary descriptions of the bulk medium are thus valuable to extract robust information on charmonium properties in heavy-ion collisions. Recent calculations of charmonium production within transport models, including regeneration reactions, can be found in Ref. [182, 183, 184], and will be reiterated in the context of heavy-ion data in Sec. 3.3. E.g., in Ref. [182], it was found that an increase in the masses of open-charm states ( $c$ -quarks and  $D$ -mesons in the partonic and hadronic phase, respectively) entails an enhanced  $J/\psi$  production, which is consistent with the systematics of the thermal model as illustrated in Fig. 30. In Ref. [185], the uncertainty in meson-induced dissociation reactions was circumvented by introducing a single matrix element for all dissociation reactions, augmented by spin-isospin factors and phase space factors (subsequently used in Refs. [183, 184]). In a similar spirit, the hadronic comover model [155] has recently been extended to include regeneration reactions [186].

### 3.2 Nuclear Absorption and Initial-State Effects

A commonly employed strategy to isolate cold-nuclear-matter (CNM) effects on the production of heavy quarkonia in heavy-ion collisions, encoded in the suppression factor  $S_{\text{nuc}}$  in Eq. (46), is to study its  $A$ -dependence in  $p$ - $A$  collisions relative to  $p$ - $p$  collisions. The pertinent effects on quarkonium production may be classified into three different stages: (1) *initial state*, prior to  $Q\bar{Q}$  production by parton fusion, due to the nuclear modification of parton distribution functions (PDFs) and/or parton energy loss; (2) *formation stage* of the quarkonium states from the initial  $Q\bar{Q}$  pair; and (3) *final-state* inelastic interactions leading to quarkonia absorption in the target matter. It is at present an open problem how to disentangle these three CNM effects from the experimental results for the  $A$ -dependence measured in  $p$ - $A$  collisions. To obtain a simplified baseline for predictions and applications in heavy-ion collisions, it is assumed that absorption is the dominant process in all three stages and may be analyzed using Glauber theory in terms of a survival probability for a  $J/\psi$  produced in a  $p$ - $A$  collision [27, 31],

$$S_{\text{nuc}}^{pA} = \frac{\sigma_{pA \rightarrow \psi}}{A\sigma_{pp \rightarrow \psi}} = \int d^2b \int_{-\infty}^{\infty} dz n_N(b, z) \exp \left\{ -(A-1) \int_z^{\infty} dz' n_N(b, z') \sigma_{\text{abs}}(z' - z) \right\}, \quad (51)$$

---

<sup>8</sup>Much like for charmonia, primordial particle production in hadronic transport models account for a formation time,  $\tau_F^h \simeq 1/\Lambda_{\text{QCD}} \simeq 0.5\text{-}1 \text{ fm}/c$ , in the rest frame of the hadron.

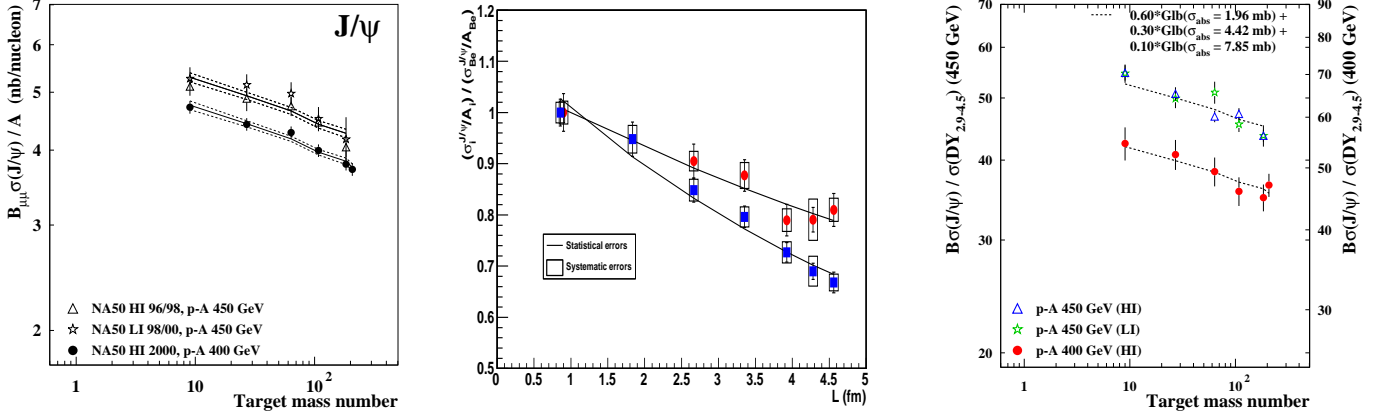


Figure 31: Left panel:  $J/\psi$  cross section in  $p$ - $A$  collisions from three different NA50 data sets [187] at 400 GeV and 450 GeV together with a Glauber fit of an effective nuclear-absorption cross section,  $\sigma_{\text{abs}} = 4.2 \pm 0.5 \text{ mb}$ . Middle panel: Cross sections for  $J/\psi$  production in  $p$ - $A$  collisions normalized to  $p$ - $Be$  for 158 GeV (squares) and 400 GeV (circles) from the NA60 experiment [188]. The lines are Glauber model fits with  $\sigma_{\text{abs}}(158 \text{ GeV}) = 7.6 \pm 0.7(\text{stat}) \pm 0.6(\text{syst}) \text{ mb}$  and  $\sigma_{\text{abs}}(400 \text{ GeV}) = 4.3 \pm 0.8(\text{stat}) \pm 0.6(\text{syst}) \text{ mb}$ . Right panel:  $A$ -dependence of the  $J/\psi$  over Drell-Yan (DY) cross section ratio, compared to a Glauber model calculation taking into account feed-down from higher  $c\bar{c}$  states [189].

where  $b$  is the impact parameter and  $n_N(b, z)$  is the density profile of the target nucleus. As a result a “convoluted”  $J/\psi$  absorption cross section,  $\sigma_{\text{abs}}$ , is extracted from experimental data for the  $A$ -dependence of the survival probability, Eq. (51), parameterizing the combined result of all CNM effects. A Glauber model fit to three different NA50 data sets [187] gives an effective nuclear absorption cross section of  $\sigma_{\text{abs}} = 4.2 \pm 0.5 \text{ mb}$  (see left panel of Fig. 31) for both 400 GeV and 450 GeV incident proton energies. Recently, the NA60 collaboration has published results for the  $A$ -dependence of  $J/\psi$  production in  $p$ - $A$  collisions at 158 GeV and 400 GeV [188] which show a larger effect at lower incident energy:  $\sigma_{\text{abs}}(158 \text{ GeV}) = 7.6 \pm 0.7(\text{stat}) \pm 0.6(\text{syst}) \text{ mb}$  and  $\sigma_{\text{abs}}(400 \text{ GeV}) = 4.3 \pm 0.8(\text{stat}) \pm 0.6(\text{syst}) \text{ mb}$ , see middle panel of Fig. 31. The origin of the increase of  $\sigma_{\text{abs}}$  towards lower collision energies is presently under investigation. One may speculate that an energy dependence of the  $J/\psi$  breakup cross section on nucleons could be responsible for such a behavior (note that the high-energy absorption cross section relevant in the present context might be quite different from the low-energy dissociation cross section discussed in Sec. 2.4 as relevant for the hadronic phase of heavy-ion collisions). Another option are formation time effects which we will return to below.

In extracting absorption cross sections from experiment one has to keep in mind that only about 60% of the observed  $J/\psi$  mesons are directly produced, while about 30% (10%) arise from  $\chi_c$  ( $\psi'$ ) feed-down. If one approximates  $\sigma_{\psi N}$  geometrically, as  $\pi r^2$ , with  $r_{J/\psi} = 0.25 \text{ fm}$ ,  $r_{\psi'} = 2 \times r_{J/\psi}$  and  $r_{\chi_c} = 1.5 \times r_{J/\psi}$ , and repeats the Glauber-model calculation, an equally acceptable description of the  $A$ -dependence for 400 GeV and 450 GeV is obtained [189], see the right panel of Fig. 31. This reasoning would point to a smaller absorption cross section for the  $J/\psi$  on nucleons, on the order of 2 mb. Formation-time effects have been evaluated in Ref. [190] within a quantum mechanical description of the formation of charmonia from an initially small-sized “pre-meson” state. An energy- and time-dependent cross section has been derived. At a collision energy of  $\sqrt{s} = 10 \text{ GeV}$ , the initial pre-meson starts out with  $\sigma_{\text{abs}} \simeq 3 \text{ mb}$ , evolving into  $\sigma_{J/\psi N} = 2.8 \pm 0.3 \text{ mb}$  and  $\sigma_{\psi' N} = 10.5 \pm 3.6 \text{ mb}$  at asymptotic times ( $t \rightarrow \infty$ ). In this framework, which is in accordance with geometric scaling, a good description of the ( $x_F$ -dependence of the) E866 data [200] can be achieved, and an apparent discrepancy between the  $\sigma_{\text{abs}}$  values extracted from hadro- and photo-production data can be resolved [191]. A characteristic

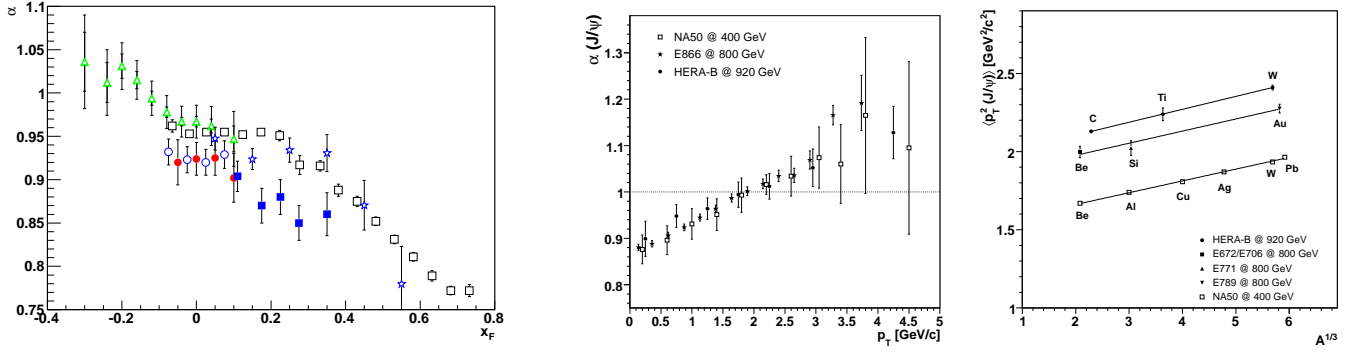


Figure 32: The nuclear-dependence parameter  $\alpha$  as a function of  $x_F$  (left panel) and of  $p_T$  (middle panel), for  $J/\psi$  mesons measured in  $p$ - $A$  collisions at three different projectile energies (the symbols in the left panel correspond to data from HERA-B (open triangles) [201], E866 (open squares) [200], NA50 at 450 GeV (open circles) [187, 202], NA60 at 400 GeV and 158 GeV (closed circles and squares, respectively) [188] and NA3 (open stars) [23]. A measure for  $p_T$  broadening (Cronin effect),  $\langle p_T^2 \rangle$ , increases with nuclear target size and with collision energy (right); compilation of data in the left panel taken from Ref. [188] and in the middle and right panels from Ref. [189].

feature of the quantum mechanical treatment of charmonium formation in  $p$ - $A$  (also applicable to  $AA$ ) collisions [192, 193, 194, 195] is the possibility for an oscillatory behavior of the survival probability with time, most pronounced for the  $\psi'$ . This is different from the classical picture of a  $c\bar{c}$  state expanding in time [196, 197, 198, 199] and could be tested via detailed kinematic (e.g.,  $x_F$ ) dependencies of production cross sections [195].

The kinematic dependencies of CNM effects on  $x_F$  and  $p_T$  have been measured for charmonium production [23, 200, 187, 202, 201, 188] and are often parametrized with the nuclear-dependence parameter,  $\alpha(x_F, p_T)$ , defined via

$$\sigma_{pA \rightarrow \psi} = \sigma_{pp \rightarrow \psi} A^\alpha. \quad (52)$$

Results from fixed-target experiments at different center-of-mass (cm) energies are compared in Fig. 32. The values of  $\alpha$  at  $x_F \approx 0$  (relevant for heavy-ion collision experiments) tend to increase with collision energy. Since the scaling of  $\alpha$  with  $p_T$  (middle panel of Fig. 32) appears to be independent of energy, the increase with cm energy might originate from the increase of the average  $p_T$  with collision energy, see right panel of Fig. 32.

The two parameterizations of CNM effects, Eqs. (52) and (51), can be related to each other [3, 2]. Introducing the effective path length  $L$  of the  $J/\psi$  trajectory inside the target nucleus with nuclear matter density  $n_0$ , Eq. (51) can be approximated as

$$S_{\text{nuc}}^{pA} = \exp(-Ln_0\sigma_{\text{abs}}). \quad (53)$$

Comparing with Eq. (52) one finds

$$\sigma_{\text{abs}} = \frac{1 - \alpha}{Ln_0} \ln A. \quad (54)$$

If one furthermore assumes a uniform density profile, one has  $L = 3r_0A^{1/3}/4$ , and with  $A^{1/3} \approx \ln A$  (valid for large  $A > 50$ ), the relation (54) takes the form

$$\sigma_{\text{abs}} = \frac{16\pi}{9} r_0^2 (1 - \alpha), \quad r_0 = 1.2 \text{ fm}. \quad (55)$$

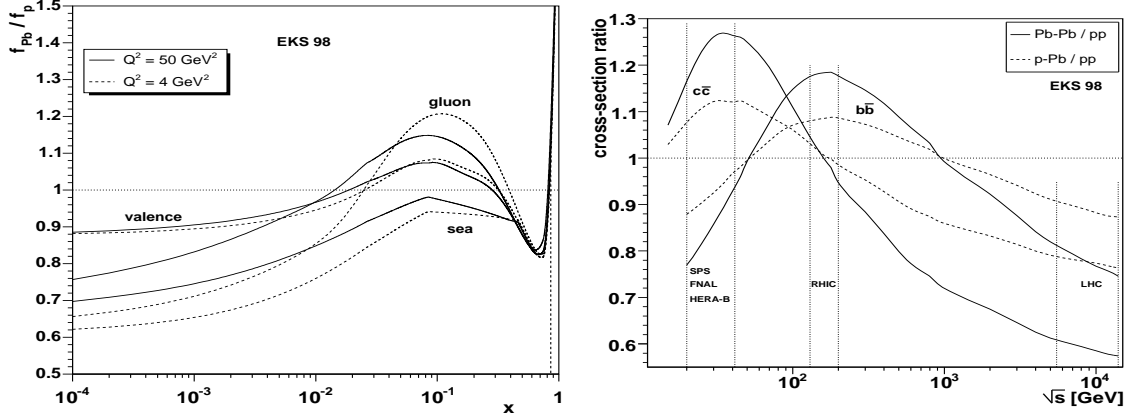


Figure 33: Left panel: nuclear modification of gluon distribution functions in a Pb nucleus, according to the EKS98 [203, 204] weight functions, from Ref. [172]. Right panel: changes of the  $c\bar{c}$  and  $b\bar{b}$  cross sections induced by the nuclear modification of the PDFs at mid-rapidity, from Ref. [172].

With this “pocket formula” a range of  $\alpha$ -values,  $\alpha = 0.95 \pm 0.02$ , translates into a range of absorption cross sections of  $\sigma_{\text{abs}} = 4.0 \pm 1.6$  mb. For a similar example, see Ref. [2].

Next we turn to CNM effects in nuclear PDFs (nPDFs),  $f_i^A(x, Q^2)$ , characterized by the ratio [205]

$$R_i^A(x, Q^2) = f_i^A(x, Q^2) / f_i^p(x, Q^2) . \quad (56)$$

The left panel of Fig. 33 shows this ratio for a lead nucleus within the EKS98 parametrization [203, 204], for two values of the momentum transfer,  $Q^2 = 4(50)$  GeV<sup>2</sup>, appropriate for  $c\bar{c}$  ( $b\bar{b}$ ) production. Relevant values for the Bjorken variable,  $x = M/\sqrt{s}$ , at central rapidity ( $y = 0$ ) and for charm (bottom) production,  $M \sim m_Q = 1.5(5)$  GeV, are in the range of  $0.03 < x < 0.3$  from SPS to HERA-B energies ( $200 < E_{\text{lab}} < 920$  GeV, corresponding to  $\sqrt{s} = 20\text{--}40$  GeV). Of particular interest are gluons, which are expected to dominate the production cross section for  $Q\bar{Q}$  pairs via the two-gluon fusion process (except for close to the production threshold). Typical nuclear effects are: (a) shadowing at low  $x$ , where  $R^A(x, Q^2) < 1$ , (b) anti-shadowing at intermediate  $x$ , where  $R^A(x, Q^2) > 1$ , (c) EMC effect at  $0.25 < x < 0.8$ , where  $R^A(x, Q^2) < 1$ , and (d) Fermi motion at  $x \approx 1$ , where  $R^A(x, Q^2) > 1$ . The right panel of Fig. 33 indicates a 10%  $c\bar{c}$  production cross section enhancement at midrapidity for SPS energies, while there is essentially no effect at RHIC. On the other hand, for d-Au collisions at backward rapidities ( $y = -2.0$ ) at RHIC, a 15% antishadowing is predicted, compared to 20% shadowing at forward rapidities of  $y = 2.0$  (in the direction of the Au beam). This trend for the  $y$  dependence can be seen in the recent PHENIX data at  $\sqrt{s_{NN}} = 200$  GeV [207], see left panel of Fig. 34. Based on EKS98 PDFs, a best fit to the measured nuclear modification factor,  $R_{\text{dAu}}$ , results in a “residual” nuclear absorption cross section of  $\sigma_{\text{abs}} = 2.8^{+1.7}_{-1.4}$  mb. For the nDSg PDF [206] a smaller cross section of  $\sigma_{\text{abs}} = 2.2^{+1.8}_{-1.5}$  mb has been extracted. This is an example of how, in principle, a “de-convolution” of initial-state effects due to the nuclear dependence of PDFs (in particular for gluons) may be performed. A recent systematic study of the “residual”  $J/\psi$ -nucleon absorption cross section was performed in Ref. [208]. After factorization of the charmonium production process, a global fit involving data from SPS to RHIC energies resulted in  $\sigma_{\text{abs}} = 3.4 \pm 0.2$  mb when neglecting uncertainties in the gluon distribution functions. It was furthermore concluded that present uncertainties in the gluon (anti-) shadowing do not allow for a precise determination of  $\sigma_{\text{abs}}$ . On the one hand, the new EPS08 nPDFs [209], which, for the first time, included RHIC results for forward-rapidity hadron production in d-Au [210] into the analysis, show a strong enhancement of gluon anti-shadowing (shadowing) in the SPS (LHC) domain. On the other hand, the rather mild  $x$ -dependence of  $J/\psi$  production in  $p$ -A collisions at  $\sqrt{s_{NN}} = 38.8$  GeV in E866 [200] disfavors the nDSg, EKS98 and EPS08 parameterizations [211]. This

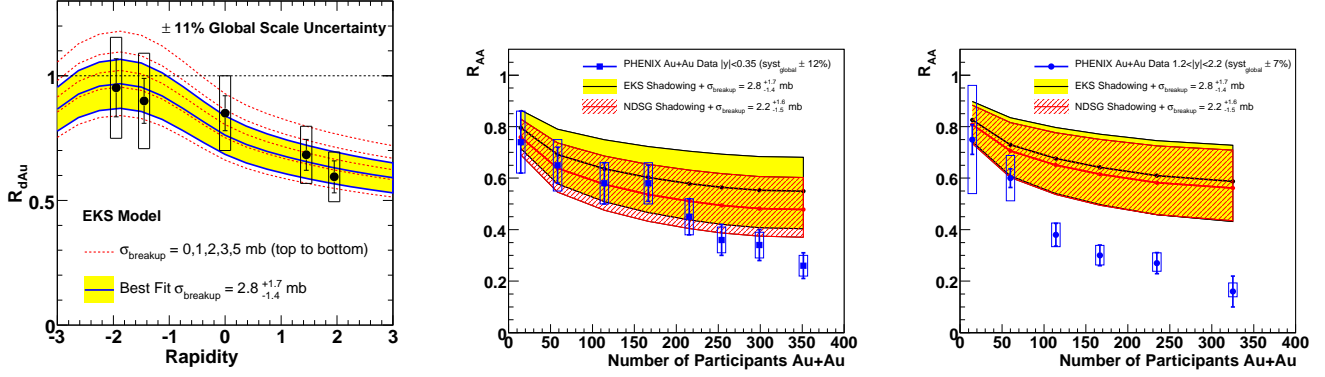


Figure 34: Left panel: PHENIX data for the nuclear modification factor,  $R_{dAu}$ , as a function of rapidity, compared to theoretical curves using the EKS shadowing model [203, 204] for different values of the nuclear absorption cross section  $\sigma_{\text{abs}} (= \sigma_{\text{breakup}})$ . The best fit to these data gives  $\sigma_{\text{abs}} = 2.8^{+1.7}_{-1.4}$  mb. Middle panel:  $R_{AA}$  for Au-Au collisions at mid-rapidity compared to projections of CNM effects extrapolated from the d-Au data, for EKS98 and nDSg [206] shadowing. Right panel:  $R_{AA}$  at forward rapidity; from Ref. [207].

might suggest that the suppression observed in the BRAHMS data [210] may not be entirely attributed to nPDFs alone, but also to other mechanisms such as initial-state parton energy loss [212].

Another aspect which complicates the “de-convolution” of CNM effects is the microscopic nature of the  $J/\psi$  production process. Recent reanalyses of the two-gluon fusion process have been performed in Refs. [213, 214, 215, 216] (see also Ref. [217]). These works suggest that production processes involving a hard gluon recoiling off the  $J/\psi$  can account for the low- and intermediate-transverse momentum spectra from the Fermilab Tevatron (CDF) to RHIC (PHENIX), as opposed to the soft-gluon emission mechanism of the color evaporation model (CEM) at leading order (LO) or to the color-octet model (COM) of NRQCD at LO. In this context, one distinguishes the kinematical effect of an “extrinsic” source of  $p_T$  due to a recoiling gluon from a “primary” source of  $p_T$  due to an “intrinsic”  $p_T$  inherited from the initial gluon pair (as in the COM and CEM). In the “extrinsic” case, a shift of the rapidity dependence of the  $J/\psi$   $R_{dAu}$  occurs, not inconsistent with PHENIX data [207]. In connection with the EKS98 nPDFs this requires a larger absorption cross section,  $\sigma_{\text{abs}} = 4.2$  mb, to be compatible with the data [218].

It is important to assess the limits of a classical description of CNM effects, i.e., whether a quantum mechanical approach to the propagation of a charm quark pair (pre-meson) in the nuclear environment is warranted. The pre-meson evolution is governed by two time scales: the proper time for the formation of a spectrum of charmonium eigenstates typically estimated as  $\tau_{J/\psi} \simeq (m_{\psi'} - m_{J/\psi})^{-1} \simeq 0.35$  fm/c, and the so-called coherence time,  $\tau_c = 2E_{J/\psi}/m_{J/\psi}^2$ , representing the lifetime of a  $c\bar{c}$  fluctuation in the lab frame. When the formation length becomes larger than the size of the Lorentz contracted nucleus, the phenomenon of color transparency occurs [219, 220], also interpreted geometrically by a small-size pre-meson state [221]. When the coherence length becomes comparable to this size (e.g., by Lorentz time dilation), the amplitudes for processes on different nucleons interfere destructively, producing additional suppression. A review of the quantum mechanical treatment including applications to heavy-flavor production in a nuclear environment can be found in Ref. [222].

An example for the extrapolation of the CNM effects from d-Au to Au-Au collisions is shown in Fig. 34 for mid- (middle panel) and forward rapidity (right panel) in comparison to PHENIX data [207]. While at forward rapidity the onset of effects beyond CNM suppression appears at  $N_{\text{part}} \approx 70$  (which roughly coincides with the onset of anomalous suppression in the NA50 experiment), there is almost no deviation from the CNM baseline at midrapidity, even for central collisions. This counter-

intuitive result points to the existence of an additional  $J/\psi$  production process which is predominantly operative in the central-rapidity region. In the previous Section, charm recombination in the medium has been discussed as a gain process in the kinetic equation for charmonium production. Its role in the interpretation of present and future experiments will be discussed quantitatively in the following Section.

### 3.3 Applications at SPS, RHIC and LHC

In this section we attempt to convert the theoretical and phenomenological developments described above (charmonium equilibrium properties as well as implementations into transport approaches) into interpretations of available data from ultrarelativistic heavy-ion collisions (URHICs) at SPS and RHIC. As a rough guideline, let us start by recalling some of the basic relations which have been proposed to associate different observables with key properties of charmonia in medium.

- (A) Centrality dependence of  $J/\psi$  production, which is typically normalized to the expected yield in the absence of any medium effects,  $R_{AA}(N_{\text{part}})$  – based on an increasing matter density with centrality (i.e., decreasing impact parameter), this is the classic observable to search for an anomalous suppression of charmonia possibly linked with the onset of QGP formation.
- (B) Transverse-momentum ( $p_T$ ) spectra, normalized to the expected spectra without medium effects (i.e., in  $p$ - $p$  collisions),  $R_{AA}(p_T)$  – here, the original objective is the extraction of the  $p_T$  dependence of the charmonium dissociation rates. In addition,  $p_T$ -spectra from regeneration are expected to be softer than the primordial power-law spectra, which provides a handle to disentangle secondary and (suppressed) primordial production. The discrimination power may be further augmented in the elliptic flow,  $v_2(p_T)$ .
- (C) Excitation function,  $R_{AA}(\sqrt{s})$  – the suppression effect on primordial charmonia is expected to increase with increasing collision energy, providing complementary information on the temperature and density dependence of charmonium disintegration (in addition to centrality dependencies at fixed energy). However, the possibly largest virtue of an excitation function is the stronger increase in charm-quark production relative to light particles, leading to a large variation in the charm-quark densities in the fireball which (quadratically) enhances regeneration mechanisms with increasing energy. The excitation function thus promises to be a prime observable to study the interplay of suppression and regeneration mechanisms.
- (D) Rapidity dependence,  $R_{AA}(y)$  – the idea behind this observable is reminiscent of (C) in that light- and charm-quark production are characterized by different rapidity distributions (narrower for heavy quarks); regeneration, being proportional to  $N_{cc}^2$  (grand-canonical limit), should thus lead to a narrowing of the charmonium distributions compared to  $p$ - $p$  collisions.
- (E) Excited charmonia ( $\chi_c$ ,  $\psi'$ ) – different binding energies, dissociation rates and dissolution temperatures are hoped to provide a systematic suppression/production pattern that can serve as a “thermometer” upon varying control parameters such as centrality, system size and collision energy (all of the  $J/\psi$  observables listed under (A)-(D) apply here).
- (F) Bottomonia – due to stronger binding energies, bottomonium suppression could provide a more sensitive measure of color screening via an associated increase in dissociation rates. This notion is corroborated by the small open-bottom cross sections which presumably suppresses bottomonium regeneration.

We recall that feed-down contributions via the decays of excited charmonia into lower lying ones need to be considered. For the  $J/\psi$  about 30% of its inclusive production yield in  $p$ - $p$  collisions arises

from decays of  $\chi_c$  states [223], and  $\sim 10\%$  from  $\psi'$  [224, 225]. Such fractions cannot be neglected in quantitative calculations of  $J/\psi$  observables in heavy-ion reactions, rendering a simultaneous and consistent treatment of medium effects on  $\chi_c$  and  $\psi'$  production mandatory. At high  $p_T > 5$  GeV, relevant for collider energies, the inclusive  $J/\psi$  yield is expected to receive additional feed-down contributions from  $B$ -meson decays, on the order of 20-40% [226, 225].

In the remainder of this Section we discuss the 6 classes of observables in the order given above, focusing on the recent status and developments, and with preference for approaches which have been applied at both SPS and RHIC energies.

### 3.3.1 Centrality Dependence

We start our discussion with the centrality dependence of  $J/\psi$  production at SPS energies, specifically with implementations of the  $J/\psi$  transport equation into a thermally expanding background medium.

In Ref. [227] the gluo-dissociation rates for  $J/\psi$  and  $\chi_c$  (using vacuum binding energies) have been folded over a 2+1 hydrodynamic evolution of Pb(158 AGeV)-Pb collisions, employing an EoS consisting of a 2+1-flavor QGP and a hadron resonance gas (connected via a mixed phase at  $T_c \simeq 165$  MeV). Hadronic suppression of the  $J/\psi$  and regeneration effects (expected to be small at SPS energies due to small open charm production) have been neglected. The primordial nuclear absorption cross section has been fixed at  $\sigma_{\text{abs}} = 4.3$  mb. The overall magnitude of the suppression in the NA50 data has been reproduced by introducing a minimal initial entropy density of  $s_0^{\text{min}} \simeq 32 \text{ fm}^{-3}$ , below which the matter is assumed to decouple instantaneously (i.e., not to become part of the thermally evolving medium); with a thermalization time of  $\tau_0 = 0.8 \text{ fm}/c$  (the moment when the hydrodynamic evolution is assumed to start), the centrality dependence of the  $J/\psi$  yield (upper left panel of Fig. 35), as well as its average momentum squared (lower left panel), are well reproduced.

Within a similar spirit, but adopting a slightly different approach, solutions of the rate equation (22) have been evaluated in Refs. [38, 97]. The thermal evolution of the medium has been treated in a more simplistic isotropic fireball expansion, parametrized to resemble hydrodynamic models, with an EoS including QGP, mixed and hadronic phases and  $T_c = 170(180)$  MeV at SPS (RHIC)<sup>9</sup>, similar to Ref. [227]. The inelastic charmonium reactions in the QGP include an in-medium reduction of the binding energies, incorporated using the quasifree dissociation process [44] (rather than gluo-dissociation, recall Fig. 16) corresponding to the rates displayed in the right panel of Fig. 17. The dissociation rates in the hadronic phase have been estimated based on  $SU(4)$  effective theory, leading to rather small effects on the  $J/\psi$  (somewhat more significant for  $\chi_c$  and  $\psi'$ ). Fixing  $\sigma_{\text{abs}} = 4.4$  mb and  $\tau_0 = 1 \text{ fm}/c$  (translating into an average initial temperature of  $\bar{T}_0 \simeq 210$  MeV in central Pb-Pb), the coupling constant in the quasifree process has been adjusted to  $\alpha_s \simeq 0.25$  to fit the suppression in central Pb-Pb. Also here the centrality dependence of inclusive  $J/\psi$  production and its mean  $\langle p_T^2 \rangle$  are well described. The contribution from regeneration turns out to be small (with a total open-charm cross section of  $\sigma_{cc}^{\text{tot}} = 5.5 \mu\text{b}$  distributed over 2 thermal fireballs, i.e.,  $\sim 3.5$  units in rapidity); it is further reduced by a schematic implementation of incomplete charm-quark thermalization via a relaxation-time factor  $\mathcal{R}(\tau)$  (with a smaller relaxation time,  $\tau_c^{\text{eq}}$ , leading to a larger regeneration yield), see below.

Hadronic comover-interaction [155] and transport [229] models have also been successful in describing the  $J/\psi$  suppression pattern observed by NA50. With a typical comover dissociation cross section of 0.65-1 mb, the required comover energy densities in central Pb-Pb are rather large, (well) above the typical value of  $1 \text{ GeV}/\text{fm}^3$  associated with the phase transition. The comover interaction is thus to be understood as at least partially of partonic origin, consistent with the rather small value of the dissociation cross section. In the hadronic transport calculations of Ref. [229], the hadronic comover

---

<sup>9</sup>A smaller value of  $T_c$  at SPS energies is expected due to its decrease with  $\mu_B$ , while  $T_c = 180$  MeV at  $\mu_B = 0$  is within the current range of lattice results for full QCD [228].

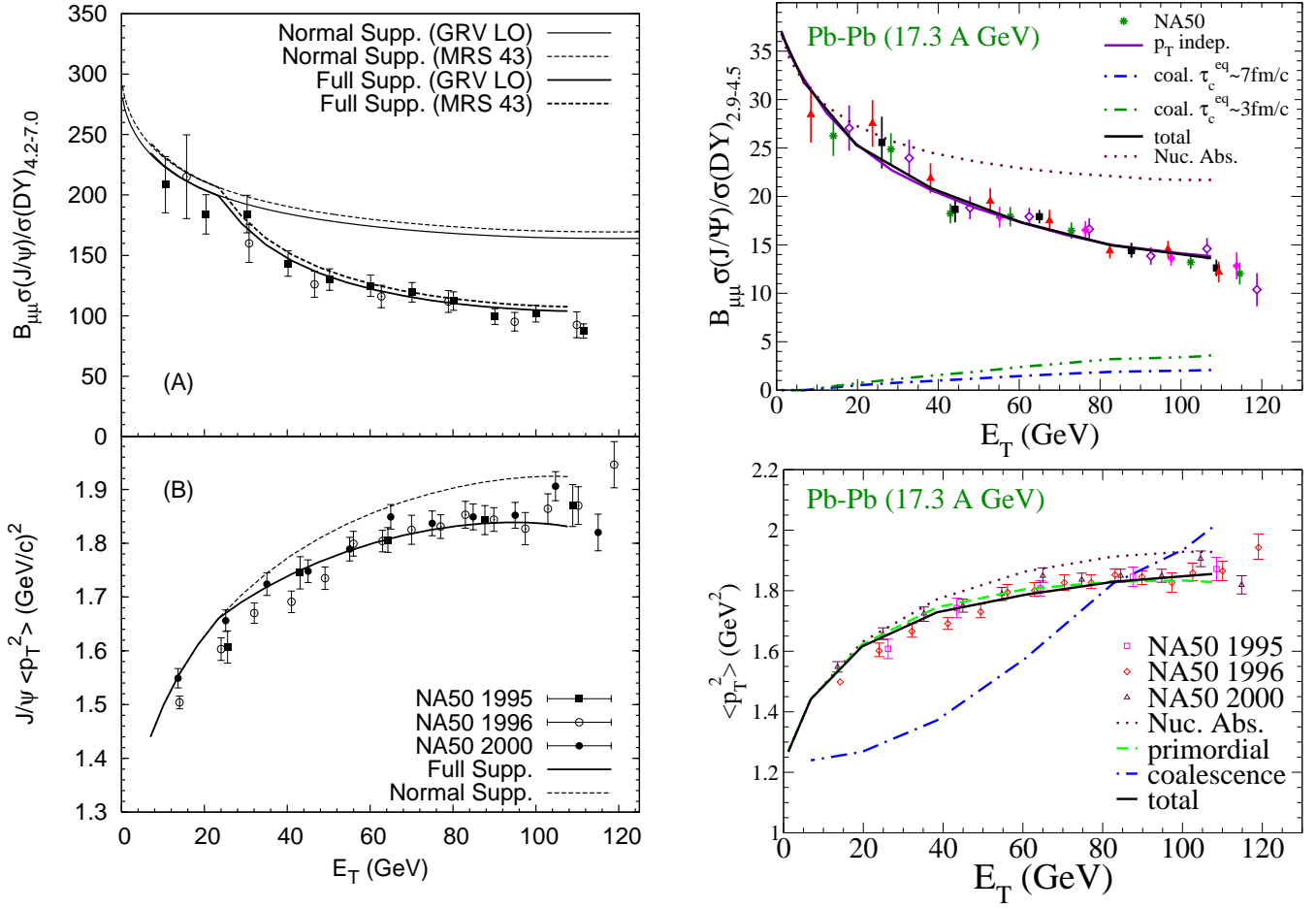


Figure 35:  $J/\psi$  production in Pb-Pb collisions at SPS employing the rate equation (45) within a hydrodynamic evolution with gluo-dissociation in the QGP (left panels, gain term neglected) [227], and within an expanding thermal fireball with quasifree dissociation in the QGP and meson-induced break-up in the hadronic phase (right panels) [38, 97]. Upper panels: nuclear modification factor as a function of centrality quantified by the measured transverse energy,  $E_T$ , of produced particles. Lower panels: centrality dependence of the average transverse momentum squared of the  $J/\psi$  spectra.

interactions are significantly larger (a few millibarns for baryon-induced dissociation, and 2/3 of that for mesons), but “pre-hadronic” degrees of freedom still play a role.

An often discussed issue in the interpretation of the NA50 data is the (non-) presence of a threshold behavior in semi-central Pb-Pb collisions, around  $E_T \simeq 30\text{-}40$  GeV. To address this question experimentally, the successor experiment NA60 has measured  $J/\psi$  production for an intermediate-size system, i.e., In-In collisions ( $A_{In} = 115$ ). The pertinent data are compared theoretical *predictions* in the left panel of Fig. 36, all 3 of which are in reasonable agreement with the Pb-Pb data. While the comover model [233] and the threshold-melting scenario [231] do not reproduce the data, the thermal rate equation approach in QGP + hadronic phase [38, 232] shows a fair agreement (except for central collisions where the data suggest a reduced suppression). The suppression pattern at SPS energies has been revisited within the Hadron String Dynamics (HSD) transport model in Ref. [183], where charmonium suppression was studied within the QGP threshold-melting scenario (middle panel of Fig. 36) and a comover-interaction model (right panel of Fig. 36). The former is characterized by critical energy den-

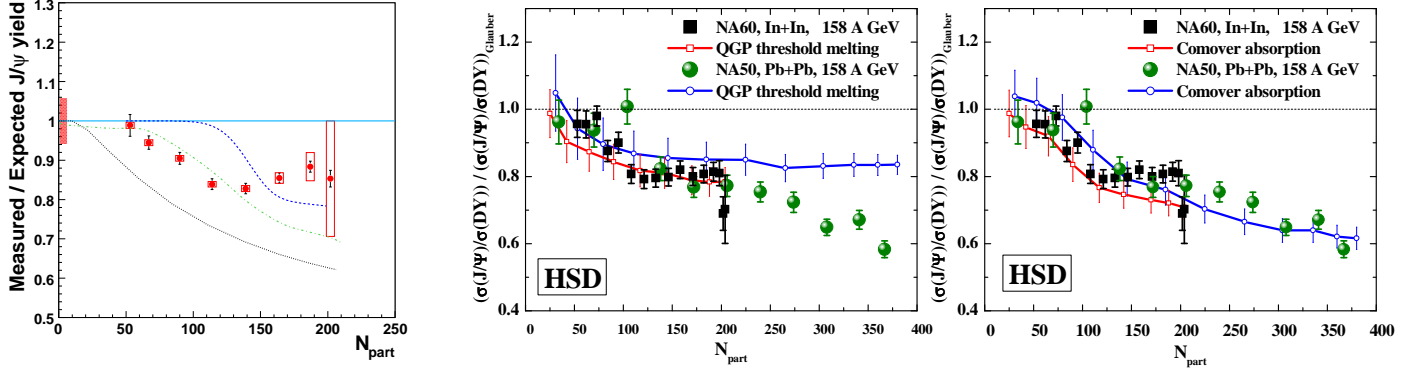


Figure 36: Left panel: NA60 data for  $J/\psi$  production in In(158 AGeV)-In collisions at SPS energies [230] compared to theoretical predictions based on the QGP threshold-suppression scenario [231] (upper dashed line), QGP and hadronic suppression in a thermal fireball [232] (middle dashed-dotted line) and the comover model [233] (lower dotted line); all models are in fair agreement with NA50 data in Pb-Pb collisions. Middle and right panels: postdictions for Pb-Pb [32] and In-In [234] data computed in the HSD transport model [183] using either a QGP threshold-melting scenario (middle panel) or comover model (right panel); note that the NA60 data are the preliminary ones from Ref. [234].

sities above which the corresponding state does not form<sup>10</sup> while the latter has been implemented via a single matrix element for all charmonium states (including phase space and spin effects). The threshold melting leads to a rather pronounced drop in  $J/\psi$  production at small centralities ( $N_{part} \leq 75$ ) together with a leveling off at large  $N_{part}$ , whereas the comover scenario produces a more gradual suppression pattern which reproduces the trend in the data somewhat better [183]. Note that the level of agreement of the HSD+comover scenario with NA60 data is quite comparable to the thermal rate-equation prediction [38, 232] in the left panel of Fig. 36 (the latter is sometimes quoted as not reproducing the NA60 data [183, 230, 235]).

Let us now turn to RHIC energies, focusing on the approaches discussed above in the SPS context. The hydrodynamic model with gluo-dissociation has been extended to include regeneration reactions,  $c + \bar{c} \rightarrow g + \Psi$ , in Ref. [165]. The charm-quark distributions figuring into the gain term, Eq. (50), have been approximated by two limiting scenarios: (a) primordial spectra in  $p$ - $p$  given by perturbative QCD (pQCD), or (b) fully thermalized spectra including the collective flow of the hydrodynamic background. The corresponding difference in the inclusive  $J/\psi$  yields turns out to be rather small, cf. upper left panels in Fig. 37. The underlying open-charm production cross section has been adopted from the PHENIX measurement in Ref. [12],  $\sigma_{pp}^{c\bar{c}} = 622 \pm 57 \mu\text{b}$ <sup>11</sup>. The experimental uncertainty translates into an uncertainty in the regeneration yield reflected by the colored bands in the left panels of Fig. 37 (the cross section has been scaled by the number of binary  $N$ - $N$  collision at given impact parameter). The overall magnitude of preliminary PHENIX  $J/\psi$  data [236] is roughly reproduced (the agreement is somewhat better with updated PHENIX data [37] displayed in the upper right panel). The contribution from regeneration is moderate but significant, reaching ca. 50% of the total yield in central Au-Au.

The right panels of Fig. 37 shown results of the thermal rate-equation approach [38], extended to include the finite 3-momentum dependence of the inelastic charmonium reaction rates [97]. Here, the impact of incomplete charm-quark thermalization has been schematically modeled by a “thermal relaxation time” factor,  $\mathcal{R}(\tau) = 1 - e^{-\tau/\tau_c^{\text{eq}}}$ , multiplying the charmonium equilibrium abundance,  $N_{\Psi}^{\text{eq}}$ , which figures into the gain term of the rate equation (22). This implementation leads to a stronger

<sup>10</sup>It may be thought of as a sudden transition of the quarkonium width from zero to infinity.

<sup>11</sup>An update of the PHENIX open-charm cross section amounts to  $\sigma_{pp}^{c\bar{c}} = 567 \pm 57 \mu\text{b}$  [169]; for both measurements the additional systematic uncertainty is about 150-200  $\mu\text{b}$ ; STAR data [170] give significantly larger values,  $\sigma_{pp}^{c\bar{c}} = 1.3 \pm 0.1 \pm 0.2 \text{ mb}$ , which is a currently unresolved discrepancy.

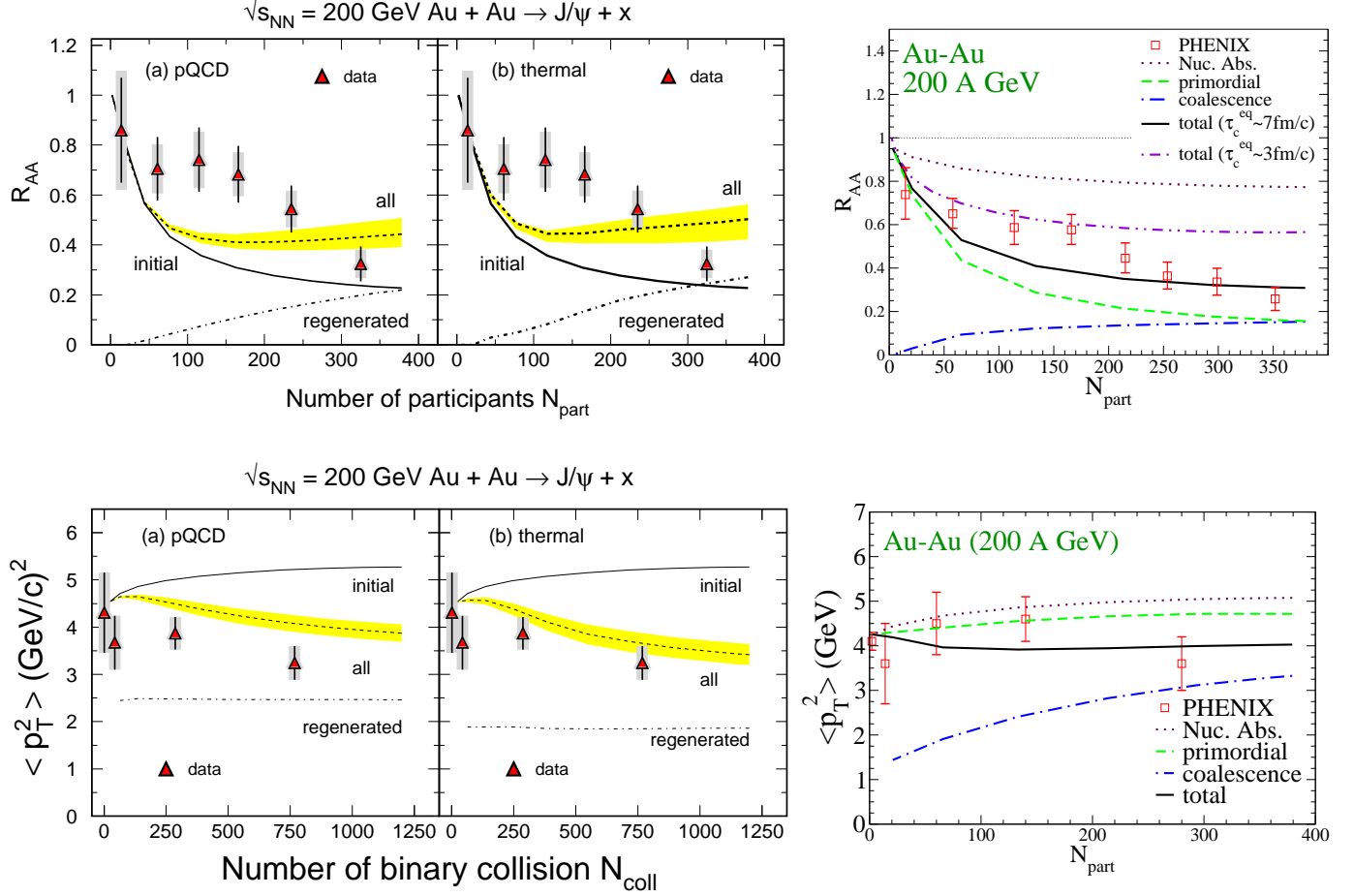


Figure 37:  $J/\psi$  production in Au-Au collisions at RHIC computed within kinetic rate equations in a thermally evolving background medium, corresponding to the approaches displayed in Fig. 35 (left panels: gluo-dissociation with vacuum binding energies in a hydrodynamic simulation [165, 227], right panels: quasifree dissociation with in-medium binding energies in a thermal fireball expansion [38, 97]). The upper panels show the nuclear modification factor,  $R_{AA}^{J/\psi}(N_{part})$  vs. centrality for inclusive  $J/\psi$  yields, while the lower panels display the centrality dependence of the  $J/\psi$ 's average momentum squared (vs.  $N_{coll}$  in the left panels and vs.  $N_{part}$  in the right panel). The left panels contain preliminary data [236], the right panels final ones [37].

dependence of the regeneration yield on charm-quark equilibration than in Ref. [165]; the original predictions of Ref. [38] were done with  $\tau_c^{eq} = 3 \text{ fm/c}$  and  $\sigma_{pp}^{c\bar{c}} = 570 \mu\text{b}$  [92] (consistent with the PHENIX cross section), which somewhat overestimate the  $J/\psi$  yield in central Au-Au as compared to the most recent PHENIX measurement [37] (cf. dash-double-dotted line in the upper right panel of Fig. 37). Using  $\tau_c^{eq} = 5-7 \text{ fm/c}$  [97] improves the agreement, implying a decomposition into primordial and regenerated component rather comparable to the one shown in the upper left panels [165]. A potential problem for both calculations are the (two) data points at  $N_{part} = 100-200$ , and has been addressed in threshold-melting scenarios [237]. HSD calculations at RHIC based on suppression-only scenarios (comover or threshold melting) [184] underpredict existing PHENIX data, thus supporting the presence of a regeneration component.

The  $J/\psi$  regeneration yield is rather sensitive to the open-charm content of the system. First and foremost, this pertains to the number of charm-anticharm pairs,  $N_{c\bar{c}}$ , in the system. In the grand-canonical limit ( $N_{op} \gg 1$ ) the charmonium equilibrium number depends quadratically on  $N_{c\bar{c}}$ . But

even at SPS energies, where charm-quark production is small and the canonical limit applies (implying that  $N_\Psi^{\text{eq}}$  depends linearly on  $N_{c\bar{c}}$ ), it has been argued that the (semi-) central NA50  $J/\psi$  data can be accounted for by statistical production alone [162] using a factor of  $\sim 2$  increase of the pQCD open-charm cross section (amounting to  $d\sigma_{c\bar{c}}/dy = 5.7 \mu\text{b}$ ; a recent data compilation of open-charm data [172] results in a value of  $\sigma_{c\bar{c}}^{\text{tot}}(E_{\text{lab}} = 158 \text{ AGeV}) \simeq 3.6\text{--}5.2 \mu\text{b}$  for the total cross section). It furthermore matters over what range in rapidity the statistical model is applied. In the canonical limit, it follows from Eqs. (47) and (48) that  $N_\Psi \propto 1/V_{FB}(N_{\text{part}})$ , which reproduces the observed centrality dependence for semi-/central collisions. The width of the considered rapidity window also affects the total yield due to different  $y$ -distributions of  $N_{ch}$  and  $N_{c\bar{c}}$ . Finally, recalling Fig. 30, even for fixed  $N_{c\bar{c}}$ , the charm-quark fugacity, and thus the equilibrium charmonium numbers, are sensitive to the underlying open-charm spectrum (e.g., due to medium effects in charm hadrons and/or quarks).

Finally, we comment on two recent developments. In Ref. [239] the regeneration processes at RHIC have been studied by performing Langevin simulations for both  $c$  and  $\bar{c}$  quarks in a hydrodynamically evolving medium and treating their mutual interaction after production via a potential taken as the heavy-quark internal energy provided by lQCD. The combination of a small spatial  $c$ -quark diffusion coefficient with a strong  $c$ - $\bar{c}$  attraction (deep potential) keeps the original  $c\bar{c}$  pair, whose primordial production essentially occurs at the same space-time point, close together and results in a sizable probability to form a charmonium bound state in the subsequent QGP and mixed-phase evolution. This “diagonal” recombination of  $c$  and  $\bar{c}$  from the same primordial  $c\bar{c}$  pair is not unlike the “canonical limit” of the statistical model, augmented by a “correlation volume” to localize it in space. The correlation volume is of course replaced by a dynamical calculation using a microscopic diffusion process. The centrality dependence of the PHENIX data for the inclusive  $J/\psi$  yield can be approximately reproduced, and the  $p_t$  spectra exhibit a significant softening caused by the softening of the (partial) thermalization of the  $c$ -quark spectra.

In Ref. [238] the thermal rate-equation approach (underlying the right panels in Figs. 35 and 37) has been employed to study the consequences of weak- and strong-binding scenarios for charmonia. Pertinent charmonium spectral functions have been constructed for these two scenarios based on the  $T$ -matrix calculations of Ref. [103] for either the free ( $F$ ) or internal energy ( $U$ ) as potential, respectively. In quasiparticle approximation, the main quantities characterizing the spectral functions and figuring into the rate equation are the temperature-dependent charmonium binding energies, charm-quark mass and inelastic width (the former two define the charmonium masses). The resulting spectral functions were constrained to yield correlator ratios close to one (in line with lQCD). In addition, updated nuclear absorption cross sections have been implemented into the initial conditions, i.e., increasing from  $\sigma_{\text{abs}} \simeq 4.5 \text{ mb}$  to  $\sim 7.5 \text{ mb}$  at SPS energy in line with recent  $p$ -A data by NA60 at 158 GeV projectile energy [188], and from 1.5 mb to  $\sim 4 \text{ mb}$  at RHIC energy (which also accounts for shadowing) [259]. Some of the findings are as follows: the strong-binding scenario (with a  $J/\psi$  dissociation temperature of  $T_{\text{diss}} \simeq 1.8T_c$ ) entails a very small “anomalous suppression” of primordial  $J/\psi$ ’s at SPS; most of the observed anomalous suppression (which is small due to the large  $\sigma_{\text{abs}} \simeq 7.5 \text{ mb}$ ) is due to  $\chi_c$  and  $\psi'$  suppression, and the regeneration contribution is small (not unlike the right panels in Fig. 35). In central Au-Au at RHIC, the partition of (suppressed) primordial and regenerated components is comparable (not unlike the right panels in Fig. 37). On the other hand, in the weak-binding scenario (with a  $J/\psi$  dissociation temperature of  $T_{\text{diss}} \simeq 1.1T_c$ ), the regeneration component exceeds the suppressed primordial one already for central Pb-Pb at SPS, and dominates the yield for central Au-Au at RHIC. While both scenarios can be compatible with the centrality dependence of the total yields, i.e.,  $R_{AA}(N_{\text{part}})$ , the different  $p_T$  dependencies of the two components offer a more promising observable for discriminating weak- and strong-binding scenarios.

### 3.3.2 Transverse-Momentum Spectra and Elliptic Flow

Charmonium  $p_T$ -spectra are believed to shed more light on the suppression mechanisms (in particular, its momentum dependence, recall Fig. 18), as well as to disentangle (suppressed) primordial and regenerated production components. Since latter is expected to follow an exponential shape (plus effects from collective flow), vs. the power-law spectra of primordial production, it should primarily contribute at low momentum (where the open-charm phase space density is largest). The  $p_T$ -dependence of suppression may thus be more directly studied toward higher momenta (unless regeneration is absent (or small) altogether, as is expected at lower collision energies). At high momenta, additional effects may lead to a reduction in charmonium suppression, e.g., escape from the fireball (“leakage effect”) [93, 177, 178, 240], delayed formation time due to Lorentz time dilation [177, 197, 241] (coupled with an inhibited formation in the QGP zone not unlike a leakage effect, or using reduced dissociation cross sections during the build-up of the charmonium wave package [181, 242]), or the Cronin effect (a broadening of hadron  $p_T$  spectra in  $p$ - $A$  relative to  $p$ - $p$  collisions) [243, 244, 245].

In lower panels of Fig. 35 the centrality dependence of the  $J/\psi$ ’s average  $p_T^2$  in the hydro+gluo-dissociation (left) and fireball+quasifree dissociation (right) calculations is compared to NA50 data. Most of the observed increase of  $\langle p_T^2 \rangle$  with centrality is accounted for by the Cronin effect. In both calculations the latter is implemented into the initial condition for the  $p_T$  spectra (at the start of the thermal evolution,  $\tau = \tau_0$ ) using an impact-parameter dependent average nuclear pathlength,  $\langle l \rangle(b)$ , of the parton prior to fusing into charmonium,  $\langle p_T^2 \rangle(b; \tau_0) = \langle p_T^2 \rangle_{pp} + a_{gN} \cdot \langle l \rangle(b)$  with  $a_{gN} = 0.76 \text{ GeV}^2/\text{fm}$  as extracted from  $p$ - $A$  data [246]. The reduction of the final  $\langle p_T^2 \rangle$  toward central collisions in the lower right panel of Fig. 35 [97] is mostly caused by the 3-momentum dependence of the quasifree dissociation rate (cf. right panels in Fig. 18), leading to larger suppression for higher momentum charmonia (the smallness of the regeneration yield, evaluated in blast-wave approximation at  $T_c$ , renders its impact on  $\langle p_T^2 \rangle$  practically negligible at SPS). A similar reduction is observed in the lower left panel of Fig. 35 [227], despite the decrease of the underlying dissociation rate with 3-momentum. In Ref. [247], the  $J/\psi$  and  $\psi'$  spectra in central Pb(158 AGeV)-Pb collisions have been analyzed using a blast-wave description alone; the extracted temperature ( $T \simeq 170 \text{ MeV}$ ) and collective expansion velocity ( $\bar{v} \simeq 0.2c$ ) are consistent with the charmonia forming at the hadronization transition (quite similar to the regeneration component in the lower left panel of Fig. 35). However, at high  $p_T > 3 \text{ GeV}$ , and toward more peripheral collisions, this description most likely needs to be supplemented by non-thermal (primordial) contributions.

At RHIC energies, the regeneration component in both the hydro+gluo-dissociation and the fireball+quasifree dissociation calculations predicts a softening of  $\langle p_T^2 \rangle$  with centrality, relative to the Cronin-enhanced initial production, see the lower panels of Fig. 37. Current PHENIX data support this scenario, but one should note that the Cronin effect is not yet well constrained from available  $d$ - $A$  data. The analysis of  $J/\psi$   $p_T$ -spectra in terms of a blast-wave description does not yet allow for a quantitative identification of the temperature and transverse flow associated with the kinetic decoupling of charmonia. However, the current PHENIX data suggest that a decoupling at the phase boundary results in spectra which are too soft [162], especially for noncentral collisions. This is illustrated more explicitly in Fig. 38, where the  $J/\psi$   $R_{AA}(p_T)$  is displayed in 4 centrality bins and compared to the fireball+quasifree dissociation approach [97]. The rather soft regeneration spectra (corresponding to decoupling at  $T_c$  with a flow velocity increasing for more central collisions), together with the much harder primordial spectra (including suppression), result in a rather flat  $R_{AA}(p_T)$  (suggesting that both primordial and regeneration components are relevant). Recent measurements of high- $p_T$   $J/\psi$ ’s in Cu-Cu( $\sqrt{s_{NN}} = 200 \text{ GeV}$ ) indicate that  $R_{AA}(p_T > 5 \text{ GeV})$  is compatible with one [249]. At first sight, and in view of the strong suppression of other measured hadrons thus far ( $R_{AA}^{\pi, \eta} \simeq 0.25$ ), this appears to be a surprise. However, estimates of bottom feed-down ( $B \rightarrow J/\psi + X$ ) and formation-time effects (via a reduced absorption cross section at early times), indicate that this observation may be understood in the framework of the rate-equation approach [250]. Formation time effects coupled with threshold

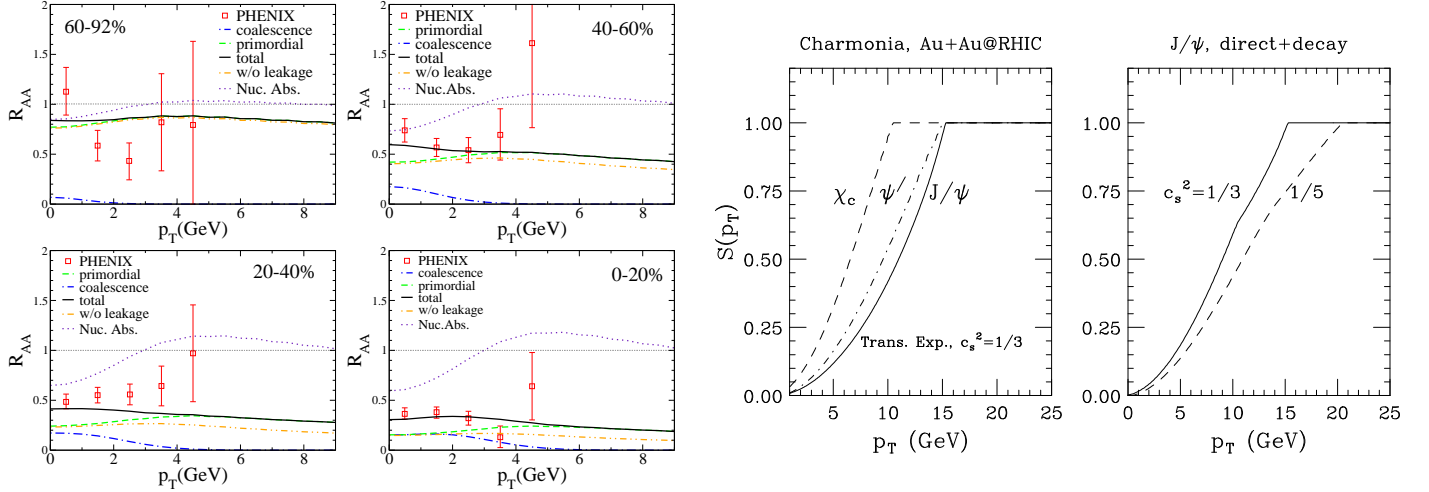


Figure 38:  $J/\psi$  nuclear modification factor as a function of transverse momentum in Au-Au( $\sqrt{s_{NN}}=200$  GeV) collisions. Left panels: PHENIX data [37] compared to calculations in a fireball+quasifree dissociation model (including regeneration) [97] in various centrality classes (dotted lines: primordial production including Cronin effect and nuclear suppression, dashed line: primordial production after QGP and hadronic suppression, dash-double-dotted line: primordial suppressed production without leakage effect, dash-dotted line: regeneration yield in blast-wave approximation, full line: total). Right panels: suppression of primordial charmonium states (second from right) and inclusive  $J/\psi$  (far right; including feed-down as well as the sensitivity to the speed of sound employed in the hydrodynamical expansion) within a hydrodynamic model employing a QGP threshold-melting scenario supplemented by formation time effects [248].

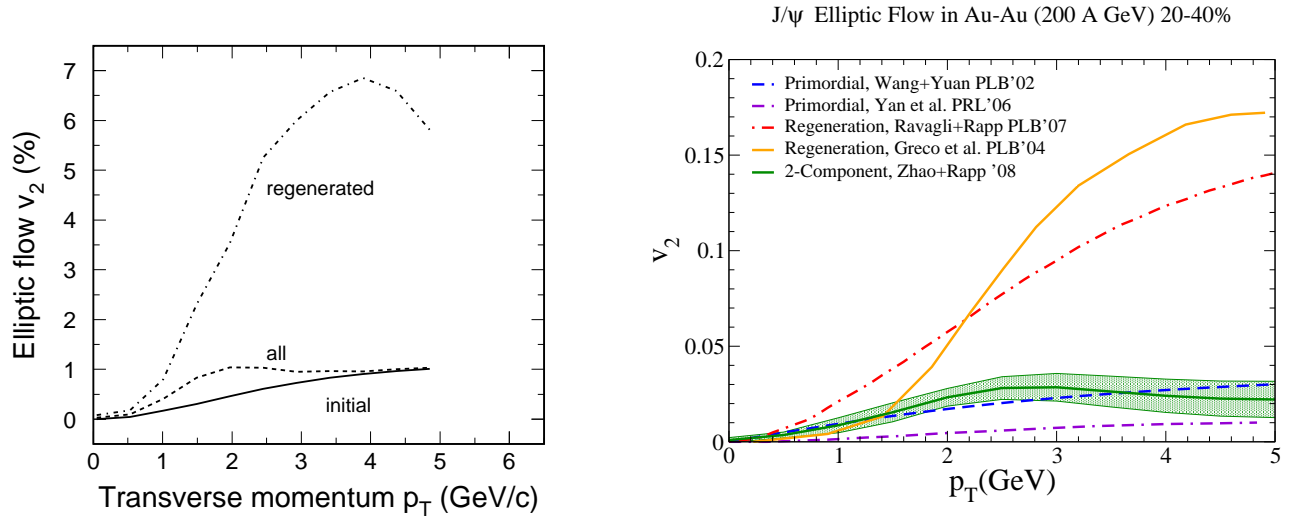


Figure 39: Theoretical predictions for elliptic flow of  $J/\psi$  mesons in 20-40% central Au-Au( $\sqrt{s_{NN}}=200$  GeV) collisions (corresponding to an average impact parameter of  $b \simeq 7.8$  fm). Left panel: transport calculations in the hydro+gluo-dissociation approach [165]; right panel: weighted average of coalescence model and suppression calculations using the  $p_T$ -dependent weights computed in the fireball+quasifree dissociation approach [97, 250].

suppression scenarios [177, 178] have indeed predicted  $R_{AA}^{\psi} \rightarrow 1$  at high  $p_T \sim 20$  years ago, see, e.g., right panel of Fig. 38 [248]. A rather unique signature of this effect is a stronger suppression of  $J/\psi$  relative to  $\chi_c$ , which is opposite to both conventional suppression and statistical hadronization scenarios.

A promising observable to discriminate suppressed primordial production from regeneration is believed to be the azimuthal asymmetry of  $J/\psi$  production in the transverse plane, quantified by the second Fourier coefficient,  $v_2(p_T)$ , in the azimuthal angle,  $\phi$ , relative to the direction of the impact parameter vector (commonly identified with the positive  $x$ -axis),

$$\frac{dN_\Psi}{d^2p_T} = \frac{dN_\Psi}{2\pi p_T dp_T} (1 + 2v_2(p_T) \cos(2\phi) + \dots) . \quad (57)$$

Direct and regenerated charmonia are expected to exhibit a large difference in  $v_2$ . For the former, the azimuthal asymmetry is solely due to different absorption path lengths of the  $J/\psi$  traversing the almond-shaped overlap zone in a noncentral nuclear collision: a shorter path length along the “short” ( $x$ -) axis of the almond implies less suppression, while there is larger suppression along the “long” ( $y$ -) axis. Calculations typically predict a corresponding  $v_2$  of up to 1-3 % [165, 251], see Fig. 39. On the contrary, if charmonia are regenerated from  $c\bar{c}$  coalescence, their  $v_2$  is largely determined by the underlying charm-quark elliptic flow,  $v_2^{c,\bar{c}}$ , and expected to approximately “scale” as  $v_2^\Psi(p_T) \simeq 2v_2^c(p_T/2)$  (assuming  $v_2^c=v_2^{\bar{c}}$ ) [252, 164, 255]<sup>12</sup>. Such an approximate scaling has been observed at RHIC for light and strange mesons and baryons, with the inferred light-quark  $v_2$  reaching up to  $\sim 7$ -8%. If the charm-quark  $v_2$  reaches similar values (as suggested by theoretical predictions [253] for semileptonic electron-decay spectra [254]), the elliptic flow of regenerated  $J/\psi$ ’s may reach up to  $\sim 15\%$  [252, 164, 255] (see right panel of Fig. 39), about an order of magnitude larger than in suppressed primordial production. In a two-component picture, the combined  $v_2$  is given by the weighted sum,  $v_2^{\text{tot}}(p_T) = f^{\text{prim}}(p_T) v_2^{\text{prim}}(p_T) + f^{\text{reg}}(p_T) v_2^{\text{reg}}(p_T)$ , where  $f^{\text{prim}}(p_T) + f^{\text{reg}}(p_T)=1$  describe the fraction of primordial and regenerated  $J/\psi$ ’s at each value of  $p_T$ . The left panel of Fig. 39 displays the results of the hydro+gluo-dissociation transport model (employing thermal  $c$ -quark distributions) [165]. While the  $v_2$  of the regenerated component is large, it carries a small weight (decreasing toward higher  $p_T$ ), leading to a total  $v_2$  of around 1%. This will be very difficult to detect experimentally. In the right panel of Fig. 39, the total  $J/\psi$   $v_2$  (represented by the band) has been estimated by combining blast-wave results for the regenerated component [164, 255] with the suppression calculations of Refs. [165, 251], using the weighting following from the fireball+quasifree dissociation model [97]. The maximum value for the total  $v_2$  of  $\sim 3\pm 1\%$  is somewhat larger than in Ref. [165], mostly due to the larger  $v_2$  in the coalescence component. Most of the difference in the  $v_2$  of the regenerated component in Refs. [165] and [250] is presumably due to the fact that the former accounts for continuous regeneration throughout the QGP while the latter approximates the production at  $T_c$ . Another difference could be due to the underlying formation reaction, which is  $c+\bar{c} \rightarrow J/\psi + g$  in Ref. [165] compared to  $c+\bar{c}+p \rightarrow J/\psi + p$  ( $p=q, \bar{q}$  or  $g$ ) in Ref. [97]. The main point, however, is the overall smallness of the  $J/\psi$  elliptic flow in both approaches. Note that for semi-central collisions ( $N_{\text{part}} \simeq 150$ ), for which the  $v_2$  is evaluated, both calculations underestimate the inclusive yield (cf. upper panels of Fig. 37), leaving room for extra regeneration and thus larger elliptic flow.

### 3.3.3 Rapidity Distributions

The large mass of charm and bottom quarks implies that their rapidity ( $y$ ) distributions in hadronic (and nuclear) collisions are narrower than those of light and strange quarks/hadrons, even at the LHC. Since the equilibrium number of charmonia is given by  $N_\Psi^{\text{eq}} \propto N_{c\bar{c}}^2/V_{FB}$  (grand-canonical limit), and the volume of the fireball at a given temperature (e.g.,  $T_c$ ) is determined by the light particles, the  $y$ -distribution of the equilibrium number of charmonia will be narrower than that from primordial production, typically given by  $N_\Psi^{\text{prim}} \propto N_{c\bar{c}}$ . This is to be contrasted with the suppression of primordial production, which is expected to become *weaker* with decreasing light-particle density, thus generating

<sup>12</sup>More precisely, the  $Q$ -value of the reaction should be small, i.e., the meson mass should be close to the quark-antiquark threshold [255]; this should be a good approximation for loosely bound  $J/\psi$ ’s.

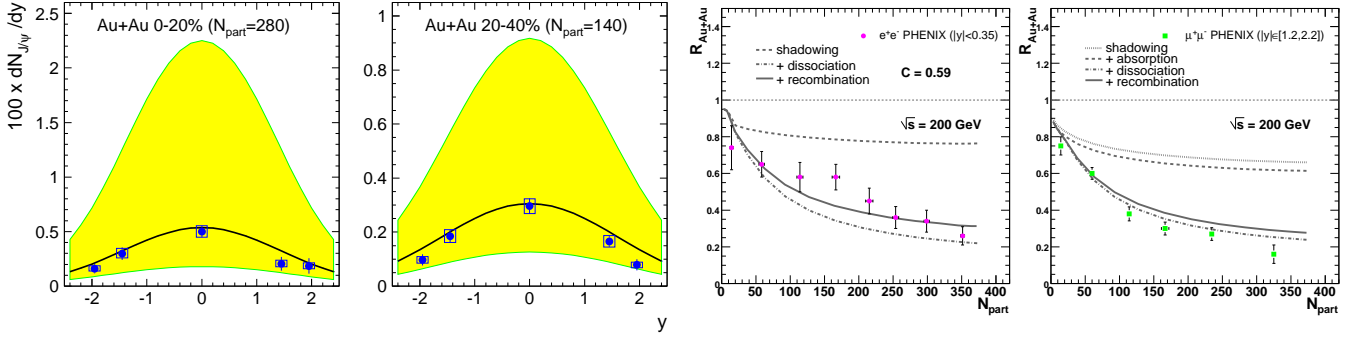


Figure 40: Rapidity dependence of  $J/\psi$  production in Au-Au ( $\sqrt{s_{NN}}=200$  GeV) collisions at RHIC. Left panels: calculations for the rapidity density in central (first left) and semi-central (second left) Au-Au within the statistical hadronization model [162], compared to PHENIX data [37]. The central lines (and shaded error bands) correspond to (the uncertainty in) pQCD charm cross sections,  $\sigma_{pp}^{c\bar{c}}=256^{+400}_{-146} \mu\text{b}$  [258]. Right panels: calculations for  $R_{AA}(N_{part})$  within the comover-interaction model (including regeneration) at mid- (second from right) and forward (far right) rapidity [186], compared to PHENIX dielectron and dimuon data [37].

a broader  $\Psi$  rapidity distribution than the primordial one (more suppression at mid- relative to forward rapidity).

The rapidity distributions of the PHENIX  $J/\psi$  data in Au-Au exhibit a narrowing relative to  $p$ - $p$  collisions which is quite consistent with regeneration only, as demonstrated by calculations in the statistical hadronization model [162], cf. the two left panels in Fig. 40. Since the  $J/\psi$  abundance in the statistical model is directly proportional to the (squared) open-charm number in the system, the open-charm cross section is the key input to compute the  $J/\psi$  rapidity distribution. Alternatively, the rapidity dependence has been evaluated in the comover-interaction model in Ref. [186] (two right panels in Fig. 40). Including shadowing and comover dissociation on the primordial component, the total suppression of the latter is about equal at mid- and forward rapidity (a larger comover density around  $y=0$  is essentially compensated by larger shadowing at  $y=1.2-2.2$ ). Only upon inclusion of a gain term does the  $J/\psi$  production at mid-rapidity slightly exceed the one at forward  $y$ . Very similar results are obtained in the thermal rate-equation approach [256]. Recent d-Au data indicate that CNM effects may account for a large part of the observed rapidity dependence [257].

### 3.3.4 Excitation Function

A promising observable to identify the interplay of (suppressed) primordial and secondary charmonium suppression is an excitation function. This is due to the much stronger increase of charm- relative to light-quark production over a large range in energy. Original predictions of a 2-component model [44] for central  $A$ - $A$  collisions envisaged a transition from a suppression-dominated regime at SPS to a largely regeneration-dominated one at top RHIC energy, cf. left panel of Fig. 41. While the more recent theoretical analyses (recall upper panels of Fig. 37) suggest that the current RHIC data contain a smaller fraction of regeneration than originally predicted, it is important to realize the following (experimental) uncertainty pertaining to secondary production in the commonly used nuclear modification factor. The latter is generically defined as the yield (or spectrum) of hadron  $h$  in  $A$ - $A$  normalized to the binary-collision scaled yield in  $p$ - $p$ ,  $R_{AA}^h = N_{AA}^h / (N_{coll} N_{pp}^h)$ . For (suppressed) primordial  $J/\psi$  production, the dependence on the initial production thus drops out (to the extent that primordial production follows binary collision scaling). This is *not* the case for the (absolutely normalized) regeneration component,

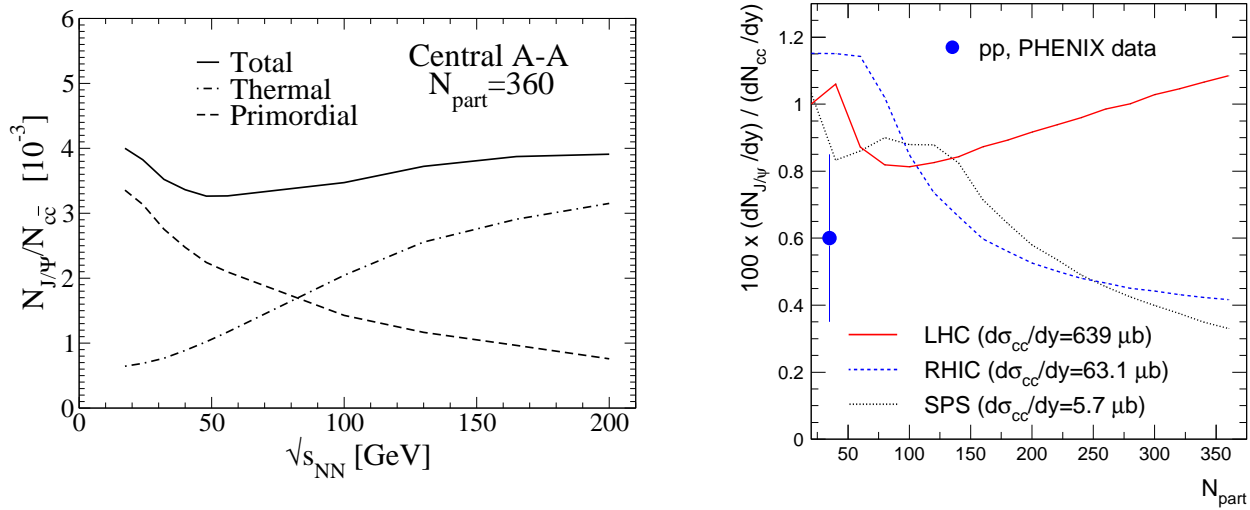


Figure 41: Collision-energy dependence of  $J/\psi$  production, normalized to the number of  $c\bar{c}$  pairs, in ultrarelativistic heavy-ion collisions. Left panel: original predictions of the 2-component model [44, 92] for central  $A$ - $A$  collisions from SPS to RHIC energies (using 2 thermal fireballs). Right panel: predictions within the statistical hadronization model for the centrality dependence at SPS, RHIC and LHC (for  $\Delta y=1$ ) including corona effects for primordial production [162]; the data point is obtained from PHENIX  $p$ - $p$  measurements [169, 259].

which in  $R_{AA}$  plots is therefore beset with additional uncertainty due to the input cross section from  $p$ - $p$  collisions (at RHIC the pertinent experimental uncertainty currently amounts to  $\sim 20$ - $25\%$  [259]).

The right panel of Fig. 41 shows calculations of the statistical hadronization model (augmented by primordial production from a corona region) for the centrality dependence of  $J/\psi$  over open-charm numbers at midrapidity for top SPS, RHIC and LHC energies [162]. The open-charm production cross section is taken from pQCD (using  $N_{coll}$ -scaling for  $A$ - $A$ ) along with assuming a fixed value of  $N_{J/\psi}/N_{c\bar{c}}=1\%$  in  $p$ - $p$ . The increasing trend toward more peripheral collisions at SPS and RHIC is largely induced by the canonical suppression factor (for central collisions, the results are in fair agreement with the excitation function in the left panel of Fig. 41). At LHC, however, the transition to the grand-canonical ensemble is essentially completed at  $N_{part} \simeq 100$ , so that for larger centralities a distinct increase of  $N_{J/\psi}/N_{c\bar{c}}$  occurs, signaling the dominance of the recombination of uncorrelated  $c$  and  $\bar{c}$  quarks into  $J/\psi$ 's.

### 3.3.5 Excited Charmonia

In all phenomenological applications discussed in this section thus far the number of  $J/\psi$ 's refers to inclusive production, i.e., contains the feed-down contributions of excited charmonia ( $\sim 30(10)\%$  from  $\chi_c(\psi')$  in  $p$ - $p$  reactions). E.g., a comprehensive interpretation of SPS and RHIC data in terms of a schematic “sequential melting” scenario has recently been presented in Ref. [260]. In addition to their role in  $J/\psi$  production, excited charmonia provide complementary information on the produced medium as their (in-medium) binding energies, dissociation widths and dissolution temperatures (are expected to) differ significantly from the  $J/\psi$ . Consequently, future experimental programs put a large emphasis on direct measurements of  $\chi_c$  and  $\psi'$ , as elaborated in Sec. 4. E.g., ratios of different charmonia can be used to test the occurrence of relative chemical equilibrium.

NA50 data for the  $\psi'/(J/\psi)$  ratio in Pb-Pb collisions at SPS exhibit a pronounced decrease with centrality up to a factor of  $\sim 3$ , see left panel of Fig. 42 [261]. It has been suggested [262] that a dropping  $\sigma$ -meson mass (as a consequence of (partial) chiral symmetry restoration) accelerates the

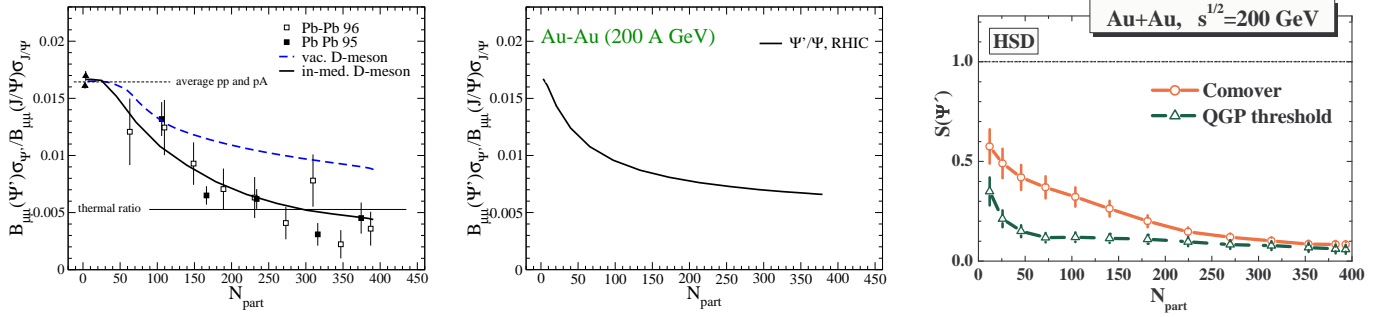


Figure 42:  $\psi'$  production in ultrarelativistic heavy-ion collisions. Left and middle panel:  $\psi'/(J/\psi)$  ratio as computed in the thermal rate-equation approach with quasifree dissociation in the QGP and hadronic dissociation with (solid lines) and without (dashed lines) in-medium  $D$ -meson masses at SPS (left; data from Ref. [261]) [38] and RHIC (middle). Right panel:  $\psi'$  suppression (nuclear modification) factor in the HSD transport approach in the comover-interaction (circles) and QGP threshold-suppression (triangles) scenarios [263]; upon dividing the  $\psi'$  suppression factor by the one for the  $J/\psi$  (see Fig. 9 in Ref. [263]), the comover result is rather compatible with the rate-equation curve in the middle panel.

transition rate for  $\psi' \leftrightarrow J/\psi + \sigma$  close to  $T_c$  and can account for the  $\psi'/(J/\psi)$  data. For semi-/central Pb-Pb collisions the data can also be explained within the statistical hadronization model [41], although here the underlying mechanism is different, i.e., a QGP converting into a hadron gas in thermal and (relative) chemical equilibrium (with conserved charm- and anticharm-quark number). In the thermal rate-equation approach of Ref. [38], regeneration at SPS energies is a small effect, and the QGP phase is too short to provide sufficient  $\psi'$  suppression to describe the NA50 data for the  $\psi'/(J/\psi)$  ratio (dashed line in the left panel of Fig. 42). However, if effects of (partial) chiral restoration are implemented via an in-medium reduction of  $D$ -mesons masses (associated with their light-quark content), the direct  $\psi' \rightarrow D\bar{D}$  channel opens and increases the  $\psi'$  dissociation rate in the hadronic phase close to  $T_c$  (in the vacuum, the  $\psi'$  mass is only  $\sim 50$  MeV below the  $D\bar{D}$  threshold). This allows for a good description of the NA50  $\psi'$  data (solid line in the left panel of Fig. 42). Alternatively, a broadening of the in-medium  $D$ -meson spectral function can induce a similar effect as reduced masses, since it also opens phase space for direct  $\psi' \rightarrow D\bar{D}$  decays. Either mechanism is not mutually exclusive to a relative equilibration via  $J/\psi + \sigma \leftrightarrow \psi'$  (neither is statistical hadronization, which, however, requires the prevalence of regeneration). At full RHIC energy, both the thermal rate-equation approach (middle panel in Fig. 42) and HSD transport calculations using pre-hadronic and comover interactions with regeneration (right panel in Fig. 42) predict a  $\psi'/(J/\psi)$  ratio which is very similar to SPS energies. On the other hand, threshold-melting scenarios predict significantly sharper suppression patterns in the centrality dependence. The  $\chi_c/(J/\psi)$  ratio is expected to drop with centrality in both rate-equation and comover approaches, and to decrease more sharply for threshold-melting scenarios.

### 3.3.6 Bottomonia

Bottomonium observables add at least two aspects, relative to charmonia, to the study of the medium in heavy-ion collisions at RHIC and LHC: (i) larger binding energies (parametrically, for Coulombic wave functions,  $\varepsilon_B^{Q\bar{Q}} \propto \alpha_s^2 m_Q$ ), implying larger dissociation temperatures and thus different dissociation patterns; (ii) a larger mass of the bottom quark, reducing its primordial production (e.g.,  $N_{b\bar{b}} \approx 0.1$  per central Au-Au at RHIC [264]), which suggests that recombination effects are suppressed. The latter assertion, however, has to be taken with care since primordial  $\Upsilon$  production is also relatively small (typically  $N_\Upsilon/N_{b\bar{b}} \simeq 0.1\%$  [264, 265] compared to 1% for charm/onium), and bottom-quark fugacities can be rather large.

Early studies of bottomonium production in heavy-ion collisions have focused on suppression ef-

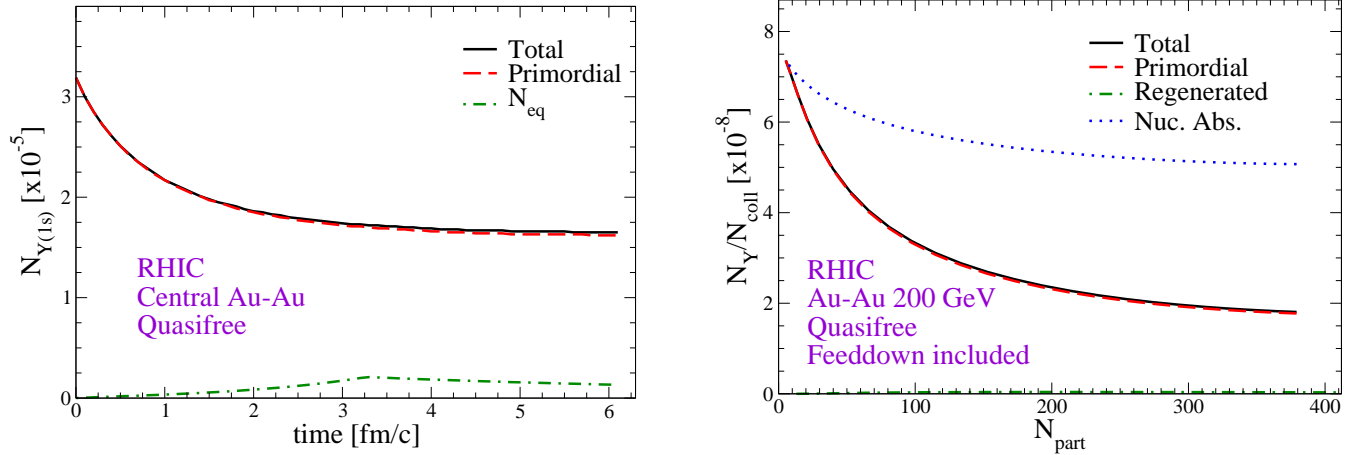


Figure 43: Predictions for  $\Upsilon$  production at RHIC within the thermal rate-equation approach using quasifree dissociation with in-medium binding [99] in an expanding fireball. Left panel: time evolution of  $\Upsilon$  abundance in central Au-Au; right panel: centrality dependence of inclusive  $\Upsilon$  yield.

fects [154, 180]. Similarly, in Ref. [266], the threshold-melting scenario, combined with formation-time effects, has been utilized to compute the  $p_T$  dependence of suppression factors,  $S(p_T) \equiv R_{AA}(p_T)$ , at the LHC. Assuming initial temperatures of  $T_0 \simeq 0.8\text{--}1.2\text{ GeV}$ , a large suppression for all states has been predicted at low  $p_T$ , which, however, gradually disappears in the range of  $p_T \simeq 5\text{--}30\text{ GeV}$  (qualitatively similar to the right panel in Fig. 38), depending on the Debye mass and surface effects in the fireball. An extension of the threshold-melting scenario to RHIC [248] suggests that directly produced  $\Upsilon$ 's do not undergo any suppression, while inclusive  $\Upsilon$ 's (which receive about 40-50% feed-down from  $\chi_b$  and  $\Upsilon'$ ) are suppressed by up to 45% at low  $p_T$  due to an almost complete melting of the excited states. As mentioned above, the threshold-melting picture represents a sharp transition between stable and dissolved quarkonia, i.e., a sudden “jump” of the inelastic width from zero to infinity. This is a simplification of a more realistic situation where the width increases with temperature more gradually, as found in microscopic calculations discussed in Sec. 2.3 (in the context of Fig. 19). On the other hand, a rather abrupt dissolution of a quarkonium bound-state as a function of temperature may be justified by potential-model calculations of spectral functions, recall Sec. 2.2. The reason is that, once the binding approaches zero, the  $Q\bar{Q}$  state in the QGP moves into the continuum and the structureless potential can no longer support resonance states. In addition, a rapid increase of the dissociation width is expected once the direct decay channel opens,  $\Upsilon \rightarrow b + \bar{b}$  or  $\Psi \rightarrow c + \bar{c}$ , i.e., above the quark-antiquark threshold in the QGP.

Quantitative studies of bottomonium suppression and regeneration have been performed in Ref. [99] within the thermal rate equation (23), solved in an expanding fireball background. When assuming vacuum binding energies for the  $\Upsilon$  throughout the QGP evolution at RHIC (with an initial temperature of  $T_0=370\text{ MeV}$ , dropping to  $300\text{ MeV}$  within the first  $0.5\text{ fm/c}$ ), the results of Ref. [248] have been confirmed in that no significant suppression of direct  $\Upsilon$ 's (i.e. those not from feed-down) occurs (nor regeneration). This is understandable due to its long lifetime of several tens of  $\text{fm/c}$  for temperatures below  $300\text{ MeV}$  (recall left panel in Fig. 19). The situation changes appreciably when in-medium reductions of the bottomonium binding energies are included (based on the in-medium rates displayed in the left panel of Fig. 19). In central Au-Au at RHIC, direct  $\Upsilon$ 's are suppressed by  $\sim 40\%$ , with most of the suppression occurring in the first  $1\text{ fm/c}$ , i.e., for temperatures above  $250\text{ MeV}$  (cf. left panel of Fig. 43). In the centrality dependence of inclusive  $\Upsilon$  production (right panel in Fig. 43) the suppression is further amplified, due to  $\sim 50\%$  feed-down contributions [267] from excited  $\chi_b$  ( $\sim 30\% \chi_{b1}$ ,  $\sim 10\% \chi_{b2}$ ) and  $\Upsilon'$  ( $\sim 10\%$ ) states; regeneration contributions are (very) small. An important point here is that direct  $\Upsilon$  suppression at RHIC is a rather direct measure of the Debye screening in the heavy-quark potential, especially since regeneration is absent. The binding energies figuring into the calculations of

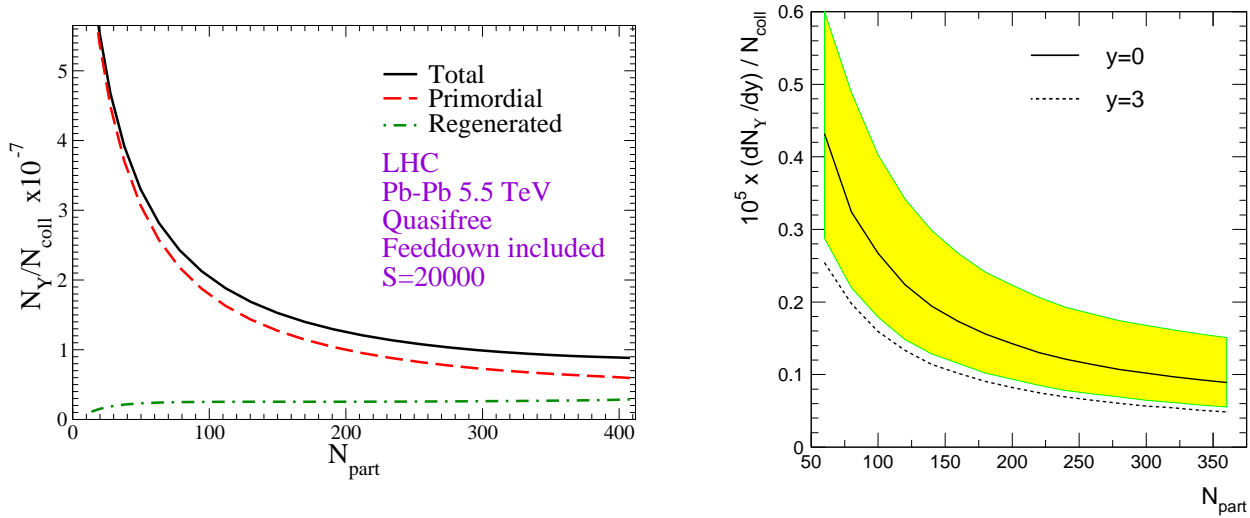


Figure 44: Predictions for the centrality dependence of inclusive  $\Upsilon$  production at LHC. Left panel: thermal rate-equation approach [99] displaying the final yield,  $N_\Upsilon$ , within a thermal fireball of rapidity width  $\Delta y = 1.8$  (the total fireball entropy of  $S = 20000$  in central Pb-Pb converts into  $dN_{ch}/dy \simeq 1600$ ). Right panel: statistical hadronization model [162] (based on  $dN_{ch}/dy \simeq 1800$ ); the yellow uncertainty band reflects a variation of the input pQCD  $b\bar{b}$  cross section by a factor of 1.5 up and down.

Ref. [99] are somewhat smaller than potential models based on the internal energy (but significantly larger than those based on the free energy), as discussed in Sec. 2.2. In either case, one could envisage a situation where the production of  $\Upsilon$  is as (or even more) suppressed as for  $J/\psi$ . This would be a rather unique QGP signature [99], and provide indisputable evidence of charmonium regeneration and color-Debye screening.

At the LHC, the situation becomes more involved. The rate-equation approach (left panel in Fig. 44) [99] predicts a suppression of up to a factor of  $\sim 10$  stronger than the statistical hadronization model (right panel in Fig. 44) [162] in central Pb-Pb collisions. Besides moderate differences in input cross sections (e.g., a factor of 0.8 shadowing correction in Ref. [99]), there are several sources of this difference: (a) the equilibrium limit in the rate equation is computed in the QGP with (in-medium) bottom-quark masses (rather than bottom hadrons), leading to smaller bottom-quark fugacities; the resulting equilibrium number is up to a factor of 3-6 smaller, depending on the (not very well known) spectrum of bottom hadrons. (b) the equilibrium limit in the rate equation is reduced by a schematic thermal relaxation-time factor,  $\mathcal{R}(\tau) < 1$ , to mimic incomplete  $b$ -quark thermalization; at the end of the QGP phase this factor has reached to about 0.3-0.5 (it is smaller earlier in the evolution). However, close to  $T_c$ , the inelastic reaction rates for the bottomonia are already rather small; (c) as mentioned for charmonia at SPS, there is a question over which range in rapidity the thermal ensemble of bottom quarks should be defined (e.g.,  $\Delta y = 1.8$  and 1 in Refs. [99] and [162], respectively). More work is needed to clarify these questions.

## 4 Future experiments

This chapter is devoted to the presentation of future opportunities of quarkonia measurements in heavy-ion collisions. Detectors are currently being designed, built, installed, commissioned or upgraded around three accelerators which will deliver heavy-ion beams in three different energy domains:

- RHIC-II (starting time scheduled for 2013) is an upgrade program of the existing RHIC (Relativistic Heavy Ion Collider) at Brookhaven National Laboratory, USA, which delivers beams up to  $\sqrt{s_{NN}} = 200$  GeV for Au. The upgrade of the machine consists of an increase of the present luminosity by an order of magnitude as well as a low-energy program ( $\sqrt{s_{NN}} = 5$ -15 GeV). Whereas the low-energy physics program will mainly focus on evidence for the critical point, the high-luminosity high-energy physics program aims at completing existing measurements with a strong emphasis on the heavy-flavor sector. To achieve this goal, an upgrade program of two detectors (PHENIX and STAR) is underway;
- The LHC (Large Hadron Collider) at CERN will provide, from 2009 on, the largest energy ever delivered by an accelerator with proton beams up to  $\sqrt{s} = 14$  TeV and Pb beams up to  $\sqrt{s_{NN}} = 5.5$  TeV. Three of the four LHC experiments (ALICE, ATLAS and CMS) will take heavy-ion data with an important part of their physics program devoted to quarkonia measurements. Whereas ATLAS and CMS are designed for proton-proton physics, ALICE is dedicated to the study of heavy-ion collisions;
- The SIS-300, located at the FAIR (Facility for Antiproton and Ion Research) at GSI, Darmstadt, will deliver, from 2015 on, heavy ion beams in fixed target mode with beam energy from 10 AGeV to 45 AGeV ( $\sqrt{s_{NN}} = 4.5$ -9.3 GeV). The Compressed Baryonic Matter (CBM) detector will allow to explore, with high-statistics measurements of rare signals like quarkonia, the moderate temperature and large baryon chemical potential region of the QCD phase diagram.

In two of these energy ranges (LHC and SIS-300) heavy quark resonances will be measured for the first time. This ensures a rich and exciting future physics program. In the following, we present the motivations for studying quarkonium production in these three energy ranges as well as a short overview of the detector capabilities needed to achieve this goal. All detectors have in common the goal of performing quarkonium measurements as a function of centrality and reaction plane, in a broad acceptance, with large statistics and low background, to ensure a mass resolution good enough to separate all vector resonances and to identify feed-down from excited states. For more details we refer to [268], to [269, 270, 271, 272] and to [273] for the RHIC-II, the LHC and the SIS-300 experimental programs, respectively.

## 4.1 Quarkonia in heavy-ion collisions at the RHIC-II

The RHIC has started delivering heavy-ion beams in 2000. Since then, the four heavy-ion experiments (BRAHMS, PHENIX, PHOBOS and STAR) have collected a large set of data for various systems at energies  $\sqrt{s_{NN}} = 20 - 200$  GeV. The status of information gathered up to 2004 has been summarized both from the theoretical side [274] and from the experimental side [275]. Hard probe precision measurements have become accessible at RHIC with the high statistics runs performed since 2004. The measurements, done by the PHENIX and STAR collaborations, have revealed some of the most exciting aspects of the hot and dense matter produced at RHIC. A particularly striking and unexpected observation in the quarkonium sector is the  $J/\psi$  suppression whose magnitude in mid-central and central heavy-ion collisions is similar to that measured at SPS energy for the Pb-Pb system (recall Figs. 35 and 37). As a consequence, several models which offer a successful quantitative description of  $J/\psi$  suppression at SPS energy (assuming that the suppression is driven by the system temperature or its energy density) over-predict the suppression observed at RHIC. Furthermore, the observed  $J/\psi$  suppression is larger in the forward region than in the central region (Fig. 40). This observation is again striking as most of the suppression models predict an opposite effect, i.e., the higher the energy density the larger the suppression. The interpretation of these observations has been discussed in Secs. 3.2 and 3.3.

Further detailed measurements are mandatory in order to disentangle the different theoretical interpretations and to achieve a comprehensive understanding of quarkonia production in heavy-ion collisions at RHIC. Indeed, direct evidence for resonance dissociation by color screening requires the centrality dependence of  $J/\psi$ ,  $\chi_c$  and  $\psi'$  to be measured simultaneously. Regeneration models can be constrained from the inspection of  $J/\psi$  rapidity distributions which are expected to narrow [162, 168] (recall Fig. 40), as well as from a precise measurement of the (open) charm production cross-section. Trends in the excitation function of  $J/\psi$  suppression could also reveal the relative importance of the regeneration process as it should increase with the multiplicity of  $c\bar{c}$  pairs [44]. More stringent tests include measurements of  $J/\psi$  elliptic flow since, as open charm shows non-zero flow<sup>13</sup>,  $J/\psi$ , if produced by regeneration, should inherit this flow (recall Fig. 39). In addition, both  $J/\psi$  flow and suppression should exhibit a specific  $p_T$  dependence marked by QGP effects at relatively low  $p_T$  whereas the high  $p_T$  region should be mostly populated by  $J/\psi$  which could escape the medium unaffected. In this respect it is also important to be able to identify secondary  $J/\psi$  from bottom decay whose yield might be sizable at high  $p_T$ . Furthermore, detailed measurements in  $p$ (-like)- $A$  collisions are mandatory in order to disentangle cold and hot nuclear effects. We finally note the possibility to identify the presence of the deconfined medium from the measurement of  $J/\psi$  polarization [276]. In addition to the above observables based on charmonia, the measurement of bottomonium states should provide additional insights. The temperature of the medium at RHIC is expected to be large enough to induce the break-up of  $\Upsilon(2S)$  and  $\Upsilon(3S)$  whereas the  $\Upsilon(1S)$  is supposed to melt at higher temperatures (it might still be affected by inelastic reactions with partons in the QGP, as discussed in Secs. 2.3 and 3.3.6).

The previously exposed physics program can partially be covered in the next years with the existing RHIC machine and detectors. However, it is clear that the full physics program requires high statistics and excellent data quality. This quality will be achieved by means of an upgrade of the machine luminosity and of the detectors.

#### 4.1.1 Experimental conditions

With the luminosity upgrade of the machine, the integrated luminosity per week is expected to be  $2500 \mu\text{b}^{-1}$  and  $33 \text{pb}^{-1}$  for Au-Au and  $p$ - $p$  collisions at  $\sqrt{s_{NN}} = 200 \text{ GeV}$ , respectively. A typical run at RHIC consists of 24 weeks of data taking. This is significantly longer than a LHC run in the heavy-ion mode (see below). As a consequence, although the heavy flavor production cross sections are much bigger at the LHC, the lower cross sections at RHIC-II are compensated by the integrated luminosity so that the heavy-flavor yields for one year of running are expected to be similar at RHIC-II and at the LHC.

#### 4.1.2 The PHENIX experiment

The PHENIX experiment is made of four spectrometers and a set of specialized detectors to determine the collision centrality and to provide triggers (Fig. 45 left). In the central region, two arms allow to detect electrons, photons and charged hadrons. They consist of a complex arrangement of drift chambers, pad chambers, Time Expansion Chambers (TEC) operated as transition detectors, time-of-flight (ToF) detectors, RICH detectors, aerogel detectors and electromagnetic calorimeters (EMCs). A magnet supplying a field parallel to the beam is placed around the interaction vertex. In the forward and backward regions, two spectrometers allow muon measurements in the rapidity range  $-2.25 < y < -1.15$  and  $1.15 < y < 2.44$ . They consist of a muon tracker (three stations of multi-plane drift chambers)

---

<sup>13</sup>In contrast to light-flavor hadrons, the heavy-flavor flow is, so far, not measured experimentally through identified hadrons, but in an inclusive way via the flow of non-photonic electrons. The latter is obtained from full distributions of electrons after subtraction of Dalitz-decay electrons from light hadrons and photon-conversion electrons.

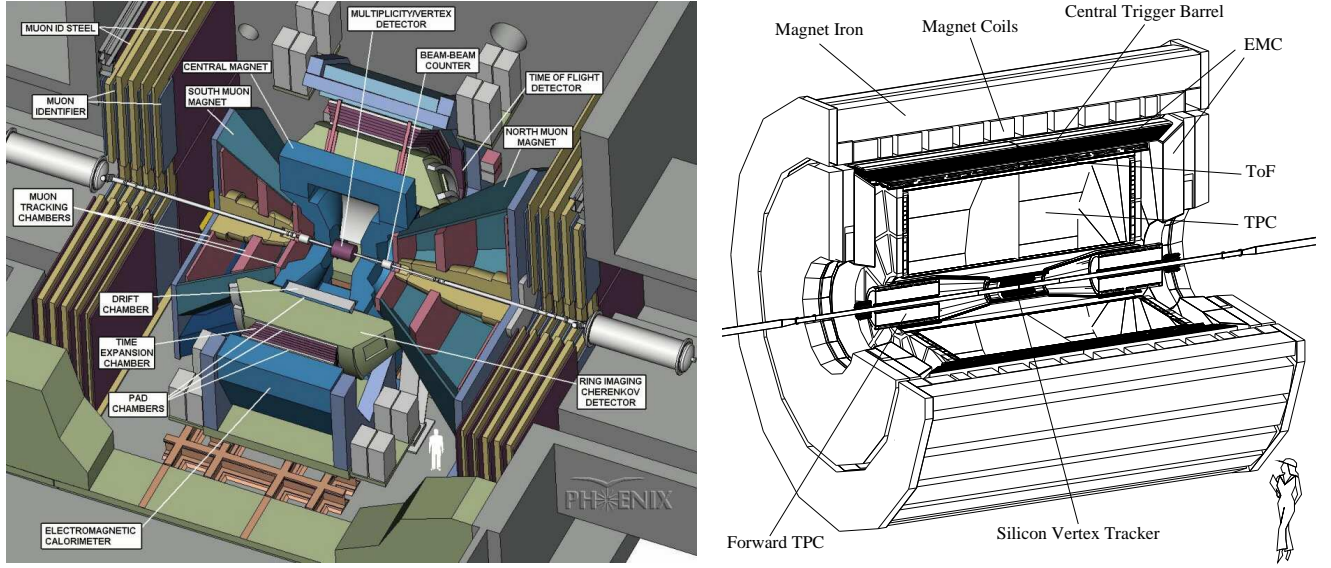


Figure 45: Longitudinal view of the PHENIX (left) and STAR (right) detectors.

placed inside a radial magnetic field, followed by a muon identifier (alternating layers of steel absorbers and streamer tubes for tracking) both with full azimuthal coverage.

The upgrade program of PHENIX [268] consists of a barrel and two endcaps Silicon Vertex Detectors (SVDs), two Nose Cone Calorimeters (NCCs) and an upgrade of the muon trigger. The SVD will provide inner tracking with full azimuthal coverage for  $|\eta| < 2.5$ . This will improve the dilepton mass resolution and reduce the background both in the electron and in the muon channels. It will further allow to measure displaced vertices which is mandatory for identification of secondary  $J/\psi$ 's from  $B$ -meson decay. The NCCs contain electromagnetic and hadronic sections covering the acceptance  $0.9 < |\eta| < 3.5$ . These are key detectors for measuring  $\chi_c \rightarrow J/\psi + \gamma$  decays. The muon trigger upgrade consists of adding three layers of RPC detectors in each muon arm together with associated front-end electronics and trigger logic. This will improve the level-1 trigger selection for both single and di-muons.

Typical expected yields with the upgraded PHENIX detector for a 12-week physics run with Au beams at RHIC-II are 45000 (395000)  $J/\psi$  and 400 (1040)  $\Upsilon$  in the electron (muon) channel.

#### 4.1.3 The STAR experiment

The different sub-systems of the STAR experiment (Fig. 45 right) are placed in a solenoidal magnet operating at 0.5 T. The main detectors are (i) a large azimuthally symmetric Time Projection Chamber (TPC) providing charged particle tracking within  $|\eta| < 1.8$ , (ii) the Silicon Vertex Tracker (SVT) and Silicon Strip Detector (SSD) for charge particle tracking close to the interaction point and vertexing, (iii) the Forward TPCs (FTPCs) covering  $2.8 < |\eta| < 3.8$  to track particles at forward and backward rapidities, (iv) the ToF system providing additional particle identification in the acceptance of the central detectors and (v) the EMC (both in the central region and at forward angles) which ensures neutral particle measurements. Additional specialized detectors complement the setup for centrality measurements and trigger.

The upgrade program of STAR [268] includes a ToF system covering the full acceptance of the central barrel, new front-end electronics for the existing TPC, an upgrade of the data acquisition system and a new inner tracking system based on two layers of silicon pixel sensors and three layers of silicon strip detectors. The ToF will extend the momentum range for hadron identification and, in conjunction with the electromagnetic calorimeter, provide a level-2 trigger for  $J/\psi \rightarrow e^+e^-$  measurements. The

new inner tracking system will make displaced vertex measurements accessible. As for the PHENIX experiment, this will be used to tag  $J/\psi$  from  $B$  hadron decays, to reconstruct charm hadron in their hadronic decay channels and will allow open heavy flavor measurements from single electrons. Finally, the DAQ upgrade will allow to collect rare signals with large statistics.

Simulations indicate that up to  $220 \cdot 10^3 J/\psi$  and 11200  $\Upsilon$  could be reconstructed in STAR during a 12 week physics run at RHIC-II in Au-Au collisions.

## 4.2 Quarkonia in heavy ion collisions at the LHC

With a nucleus-nucleus center-of-mass energy nearly 30 times larger than the one reached at RHIC, the LHC will provide the biggest step in energy in the history of heavy-ion collisions and open a new era for studying the properties of strongly interacting matter under extreme thermodynamical conditions. This new energy regime will lead to a much higher energy density, to faster equilibration and to a longer lifetime of the deconfined system, resulting in an enhanced role of the QGP over final-state hadronic interactions [277]. The high temperature and close to vanishing baryon chemical potential of the system will render it close to the conditions of the primordial universe. In addition, heavy-ion collisions at the LHC access unprecedented small Bjorken- $x$  values where low-momentum gluons are expected to be close to saturation and lead to a significant shadowing effect. As a consequence high-density parton distributions could be responsible for a large fraction of particle production [278]. Another exciting aspect of this new energy regime is the massive production rate of hard processes. They will provide an ideal tool for a detailed characterization of the deconfined medium. The heavy-flavor sector at LHC energy is also subject to significant differences with respect to SPS and RHIC energies. First, the large production rate offers the possibility to use new and a large variety of observables<sup>14</sup>. The magnitude of most of the in-medium effects is therefore anticipated to be dramatically enhanced. Some of these aspects are discussed in the following.

**New observables.** The  $\Upsilon(1S)$  state is expected to dissolve significantly above the critical temperature, at  $\sim 3\text{--}4 T_c$  [62, 71, 78], which presumably comes into reach only with the LHC. The spectroscopy of the  $\Upsilon$  family at LHC should then reveal unique characteristics of the QGP. In particular, the  $p_T$  dependence of the  $\Upsilon(2S)/\Upsilon(1S)$  ratio presents significant sensitivity to the dissociation temperatures [266] (see Refs. [99, 280] for updates). Measuring the  $\Upsilon(2S)$  is also particularly interesting in order to unravel  $J/\psi$  suppression versus regeneration: the  $\Upsilon(2S)$  and  $J/\psi$  dissociation temperatures are predicted to be similar [62] whereas, in contrast to charmonia, bottomonia are expected to be little affected by regeneration processes [99]. Electroweak  $Z^0$  and  $W^\pm$  bosons will be available with large statistics and can serve as reference processes for quarkonium suppression studies.

**Large resonance dissociation rate.** In addition to comoving hadrons and color screening, quarkonia can be destroyed by parton ionization [281]. This mechanism, induced by thermal partons in the QGP, starts being effective for temperatures above the critical temperature but below the temperature of resonance dissociation by color screening (cf. Sec. 2.3). Recall, however, the interplay between the two mechanisms on the final quarkonium yields: a large dissociation by color screening implies a low binding which facilitates a large break-up rate by parton ionization. Recent estimates [279] (see Ref. [91] for an update) of the quarkonium dissociation cross sections show that none of directly produced the  $J/\psi$  survives the deconfined phase at LHC, and that about 20% of the  $\Upsilon$  are destroyed, possibly more if color-screening is strong, cf. Fig. 44 [99].

---

<sup>14</sup>From RHIC to LHC, it is expected that the number of  $c\bar{c}$  ( $b\bar{b}$ ) pairs produced in central nucleus-nucleus collisions will increase by a factor 10 (100) [270]: up to 115  $c\bar{c}$  (5  $b\bar{b}$ ) pairs are expected to be produced in 5 % central Pb-Pb collisions at 5.5 TeV. This estimate is based on next-to-leading order pQCD calculations and includes shadowing; see Refs. [270, 279] for more details.

**Large secondary charmonium production.** Secondary charmonia yields can arise due to statistical hadronization [282] and/or kinetic recombination [42]. These processes result in an increase of  $J/\psi$  yield with collision centrality roughly proportional to  $N_{c\bar{c}}^2$  (grand-canonical limit). Again, this effect is expected to entail dramatic consequences at the LHC. Due to the large number of  $c\bar{c}$  pairs produced in heavy-ion collisions at LHC, models predict a qualitatively different centrality dependence of the  $J/\psi$  yield [279, 283], recall right panel of Fig. 41.

**Large charmonium rate from  $B$  hadron decay.** Another source of non-direct charmonia arises from the decay of  $B$  mesons. The ratio  $N(B \rightarrow J/\psi)/N(\text{direct } J/\psi)$  can be determined as follows. The number of directly produced  $J/\psi$  in central (5%) Pb-Pb collisions at 5.5 TeV is 0.5 [279]<sup>15</sup>. The corresponding number of  $b\bar{b}$  pairs (with shadowing) amounts to 4.6 [279]. The  $B \rightarrow J/\psi X$  branching ratio is  $1.16 \pm 0.10\%$  [284]. Therefore  $N(B \rightarrow J/\psi)/N(\text{direct } J/\psi) = 20\%$  in  $4\pi$ <sup>16</sup>. The secondary  $J/\psi$  from  $B$ -meson decay must be subtracted from the primary  $J/\psi$  yield prior to  $J/\psi$  suppression studies. They can further be used in order to measure the  $B$ -meson production cross section in  $p$ - $p$  collisions [226], to estimate shadowing in  $p$ - $A$  collisions and to probe the medium-induced  $b$ -quark energy loss in  $A$ - $A$  collisions. Indeed, it has been shown [285] that the  $p_T$  and  $\eta$  distributions of those  $J/\psi$  exhibit pronounced sensitivity to  $b$ -quark energy loss.

#### 4.2.1 Experimental conditions

The LHC will be operated seven months per year in the  $p$ - $p$  mode and one month per year in the heavy-ion mode. The corresponding estimated effective running time is  $10^7$  s and  $10^6$  s for  $p$ - $p$  collisions and  $A$ - $A$  collisions, respectively. The expected luminosity for Pb-Pb collisions is about  $5 \cdot 10^{26} \text{ cm}^{-2}\text{s}^{-1}$  which results in a minimum-bias interaction rate of 4 kHz. As described in Ref. [269], the heavy- (and light-) ion runs include, over the first five years of operation, one Pb-Pb run at low luminosity, two Pb-Pb runs at high luminosity, one  $p$ - $A$  run and one light ion-ion run. In the following years different options are considered depending on the first results.

#### 4.2.2 The ALICE experiment

ALICE (A Large Ion Collider Experiment) is the only LHC experiment dedicated to the study of nucleus-nucleus collisions [269, 270]. The ALICE physics program also includes the study of  $p$ - $p$  collisions which will provide the reference for heavy-ion data. The ALICE experiment is designed to perform high-precision measurements of numerous observables based on hadrons, leptons and photons, in a broad acceptance.

The detector (Fig. 46) consists of a central part, a forward muon spectrometer and forward/backward small acceptance detectors. The central part of ALICE consists of four layers of detectors placed in the solenoidal field ( $B \leq 0.5$  T) provided by the L3 magnet previously used at the Large Electron Positron collider (LEP). From inside out, these detectors are (i) the Inner Tracker System (ITS) consisting of six layers of silicon detectors, (ii) the TPC, (iii) the Transition Radiation Detector (TRD) and (iv) the ToF system based on multi-gap resistive plate chambers. They provide charged particle reconstruction and identification in the pseudo-rapidity range  $|\eta| < 0.9$ , with full azimuthal coverage and a broad  $p_T$  acceptance. The ALICE central barrel will later be equipped with a large acceptance ( $|\eta| < 1.4$ ,  $\Delta\Phi = 110^\circ$ ) EMC (not shown in Fig. 46). These large area devices are complemented by two

<sup>15</sup>Including shadowing and feed-down from higher states.

<sup>16</sup>This ratio is subject to large uncertainties since (i) the predictions from the color-evaporation model (CEM) on  $J/\psi$  cross sections differ by up to a factor of 2 at LHC energies [279], and (ii) the total  $b\bar{b}$  production cross section in  $p$ - $p$  collisions at LHC is predicted within a factor of 2-3 uncertainty resulting from the choice of the quark mass, the renormalization and factorization scales and the parton distribution function. In addition, resonance suppression and/or regeneration, heavy-quark energy loss and other effects not taken into account here could play a significant role.

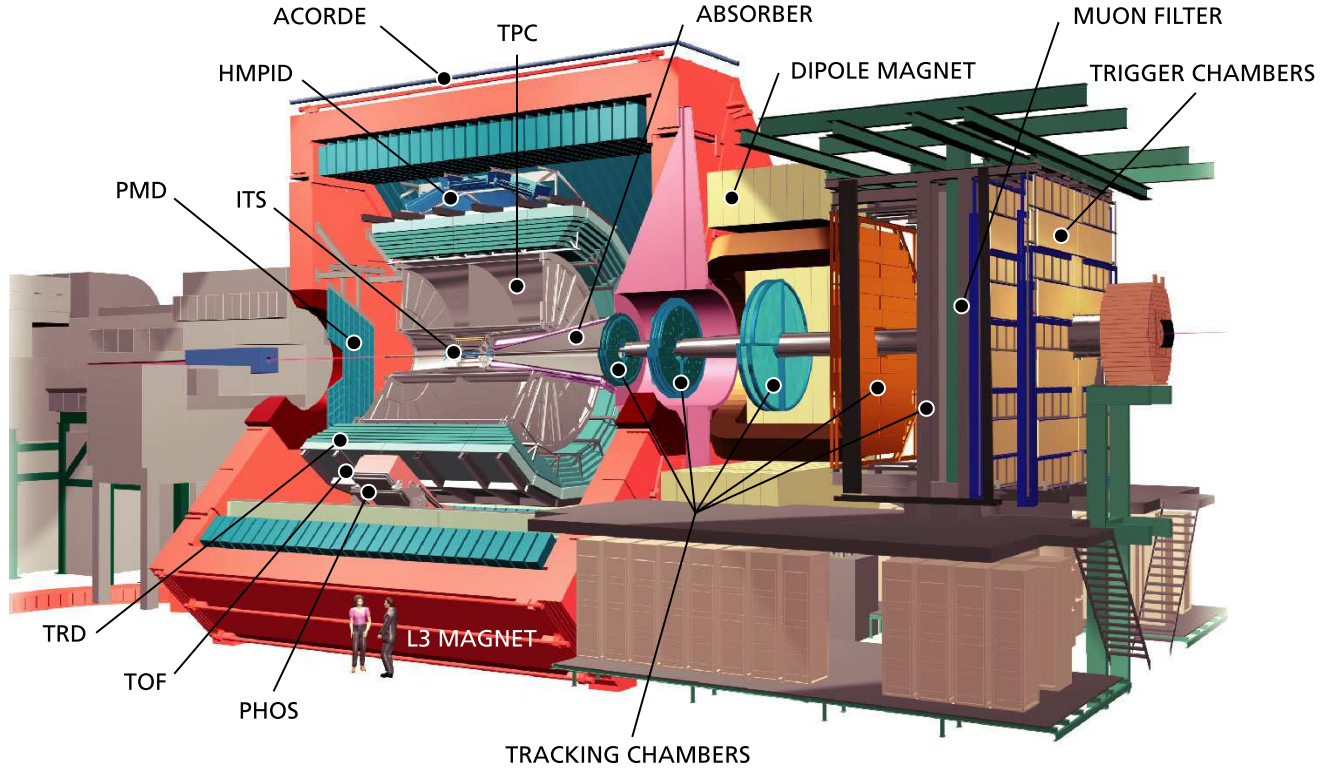


Figure 46: Longitudinal view of the ALICE detector.

smaller acceptance detectors: the High Momentum Particle IDentification (HMPID) and the PHOTon Spectrometer (PHOS). In the forward/backward region, additional detectors (T0, V0 and FMD, not shown in Fig. 46) enable a fast characterization and selection of the events, as well as charged-particle measurements in the pseudo-rapidity range  $-3.4 < \eta < 5.1$ . At large rapidities, photon multiplicity and spectator nucleons in heavy-ion collisions will be measured by the Photon Multiplicity Detector (PMD) and the Zero-Degree Calorimeters (ZDC; not shown in Fig. 46), respectively. A forward muon spectrometer covering the pseudo-rapidity range  $-4 < \eta < -2.5$  complements the central part. It consists of a front absorber, a dipole magnet, ten high-granularity tracking chambers, a muon filter and four large area trigger chambers.

The performance of the ALICE detector in the quarkonium sector is summarized in Fig. 47. Quarkonium states will be measured in both electron ( $|\eta| < 0.9$ ) and muon channels ( $-4 < \eta < -2.5$ ). The acceptance will allow reconstruction of differential distributions down to very low transverse momentum in most cases. The resolution of the apparatus, better than  $100 \text{ MeV}/c^2$  for invariant masses around  $10 \text{ GeV}/c^2$ , allows for a separation of all quarkonium vector resonance states. The expected number of reconstructed  $J/\psi$  and  $\Upsilon$  during one month of data taking is  $677 \cdot 10^3$  and 9600, respectively, in the muon channel for minimum-bias Pb-Pb collisions. The corresponding numbers in the electron channel for central (10%) collisions are  $121 \cdot 10^3$  and 1800.

#### 4.2.3 The CMS experiment

CMS (Compact Muon Solenoid) is a general-purpose detector (Fig. 48 left) designed to measure muons, electrons, photons and jets. Although the detector is optimized for  $p$ - $p$  collisions, a strong heavy-ion program has been developed [271]. CMS is composed, from the interaction point to the outer side, of a tracking system, an EMC, a hadronic calorimeter and muon chambers arranged in a central barrel and two endcaps. The central element of CMS is a 13 m long, 3 m diameter magnet which delivers

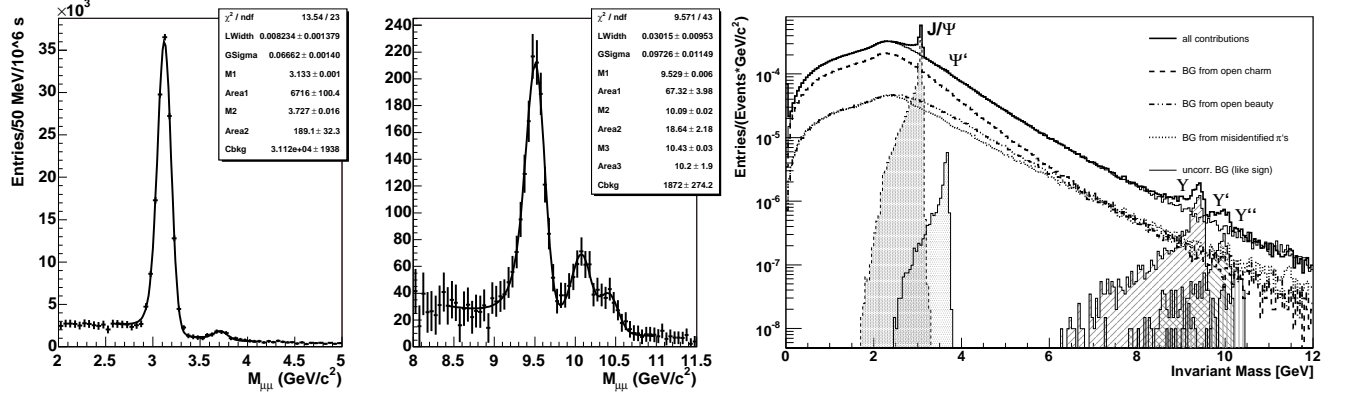


Figure 47: Invariant-mass spectra of low-mass dimuons (left), high-mass dimuons (middle), and dielectrons (right), expected to be measured with the ALICE detector within one month of Pb beam running (extracted from Ref. [270]). In the left and middle plots, the non-correlated background is subtracted from the total spectrum assuming a perfect subtraction, i.e., the statistical error of the “full” spectrum is assigned to the remaining spectrum of the sum of the correlated sources.

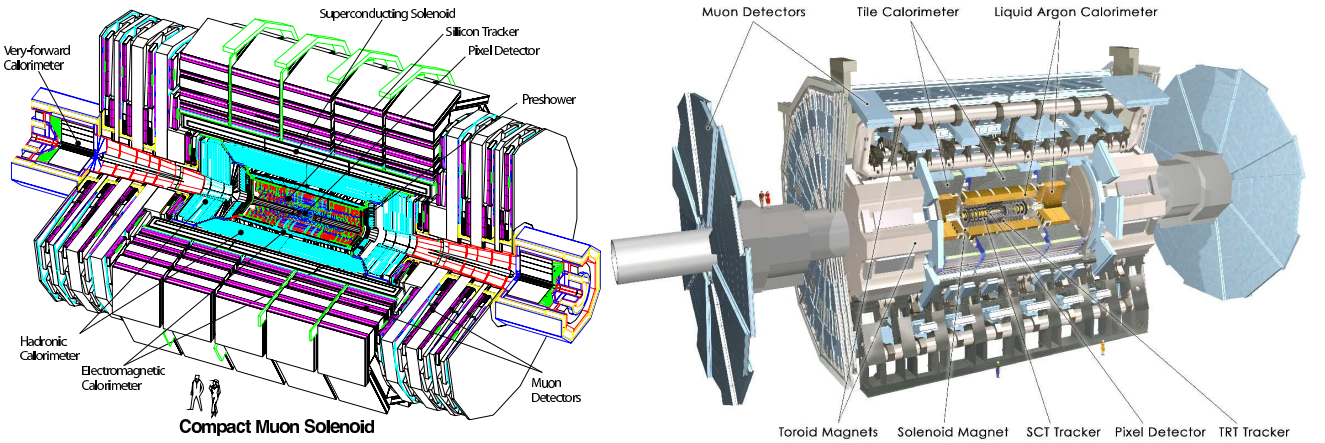


Figure 48: Longitudinal view of the CMS (left) and of the ATLAS (right) detectors.

a  $B = 4$  T solenoidal field surrounding the tracking and calorimetric systems. The tracker is based on several layers of silicon pixel and strip counters and covers the pseudo-rapidity region  $|\eta| < 2.5$ . The EMC, made of lead-tungstenate crystals, covers the pseudo-rapidity region  $|\eta| < 1.5$  in the central barrel. This coverage is extended to  $|\eta| < 3$  with the endcaps. The hadronic calorimeter is made of copper plates and plastic scintillator sandwiches. Its acceptance is  $|\eta| < 2$  in the central barrel and reaches  $|\eta| < 5.3$  with the endcaps. Two additional very forward calorimeters ensure coverage in the pseudo-rapidity range  $3 < |\eta| < 5$ . The muon system is located outside the central magnet. It consists of four layers of detectors (three for tracking and one for trigger) covering the pseudo-rapidity range  $|\eta| < 2.4$  ( $|\eta| < 1.5$  in the barrel). Very forward calorimeters, including two ZDCs ( $3 < |\eta| < 5.2$ ) and a quartz fiber calorimeter ( $5.3 < |\eta| < 6.7$ ) allow measurements of the collision centrality and electromagnetic energy (these detectors are not shown in Fig. 48).

Figure 49 shows the dimuon invariant-mass spectra expected to be measured for charmonia (left) and bottomonia (middle). The muon acceptance ranges in  $\eta$  from  $-0.8$  to  $+0.8$  in the central barrel and from  $\pm 0.8$  to  $\pm 2.4$  in the endcaps. The excellent mass resolution of the apparatus will allow a very clean separation of quarkonia from the  $J/\psi$  to the  $\Upsilon(3S)$ . In the acceptance of the central barrel,  $J/\psi$

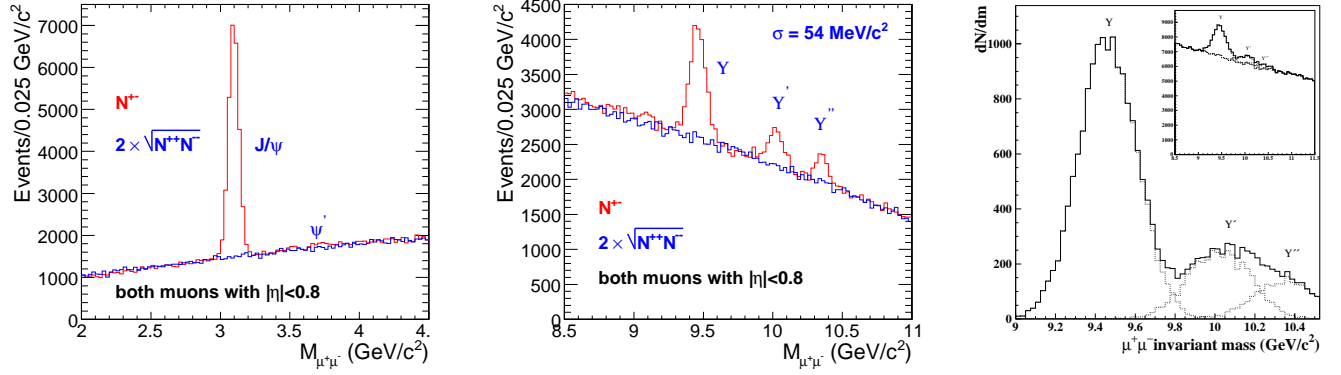


Figure 49: Invariant-mass spectra of opposite-sign and like-sign muon pairs in the  $J/\psi$  (left) and  $\Upsilon$  (middle) mass regions expected to be measured with the central barrel of the CMS detector within one month of Pb-Pb collisions [271]. Right: corresponding invariant-mass spectrum of high-mass opposite-sign muon pairs reconstructed with the ATLAS detector [272].

measurements will be limited to  $p_T > 4 \text{ GeV}/c$  due to a high  $p_T$  threshold induced by the calorimeters on single muons. This can be extended to lower  $p_T$  when detecting muons in the endcaps thanks to the extra longitudinal Lorentz boost. Due to its higher mass, bottomonium will be measured down to zero  $p_T$  in the whole  $\eta$  acceptance. Simulation results indicate that the typical number of reconstructed  $J/\psi$  and  $\Upsilon$  will be  $184 \cdot 10^3$  and  $37.7 \cdot 10^3$  in minimum-bias Pb-Pb collisions for one month of data taking.

#### 4.2.4 The ATLAS experiment

Like CMS, ATLAS (A Toroidal LHC ApparatuS) is designed for  $p-p$  physics. The detector capabilities for heavy ion physics have been recently investigated [272]. The design of the detector (Fig. 48 right) is similar to that of CMS with a tracking system, an EMC, a hadronic calorimeter and muon chambers placed in a barrel and two endcaps. The tracking system of ATLAS is composed of silicon pixel detectors, the SemiConductor Tracker (SCT) made of silicon strip detectors, and the Transition Radiation Tracker (TRT). It is placed inside a  $B = 2 \text{ T}$  solenoidal magnet and covers the pseudo-rapidity range  $|\eta| < 2.5$ . The electromagnetic calorimeter is a liquid-argon device covering  $|\eta| < 4.9$ . It is surrounded by the hadronic calorimeter which consists of lead scintillators in the barrel ( $|\eta| < 1.7$ ) and liquid argon in the endcaps ( $1.5 < |\eta| < 3.2$ ). Two additional (electromagnetic and hadronic) calorimeters cover the very forward region ( $3.2 < |\eta| < 4.9$ ). The muon spectrometer consists of a toroidal magnet providing a  $B = 4 \text{ T}$  field and several muon chambers with different technologies in the barrel and in the endcaps. The acceptance of the muon spectrometer covers  $|\eta| < 1.0$  in the barrel and extends to  $\eta = \pm 2.5$  in the endcaps.

As an illustration of the ATLAS performance for measuring quarkonium signals, the right panel of Fig. 49 shows the invariant-mass spectrum of high-mass muon pairs. In the full  $\eta$  acceptance, the mass resolution is  $145 \text{ MeV}/c^2$  at around  $10 \text{ GeV}/c^2$ . The expected statistics for  $\Upsilon$  for one month of Pb-Pb minimum-bias collisions is  $10\text{-}15 \cdot 10^3$  (with a muon- $p_T$  threshold of  $3 \text{ GeV}/c$ ). The number of reconstructed  $J/\psi$  ranges from 8000 to  $216 \cdot 10^3$  depending on the trigger threshold.

### 4.3 Quarkonia in heavy-ion collisions at the SIS-300

While the future heavy-ion experiments at RHIC-II and at the LHC will focus on the study of the QCD phase diagram at large temperatures and small chemical potential, the SIS-300 accelerator at FAIR aims at exploring the region of moderate temperatures and large baryon chemical potentials. In this region

of the phase diagram, IQCD calculations predict a critical endpoint whose location is not precisely known. Beyond this critical endpoint, for higher baryon chemical potentials and lower temperatures, one expects a first order phase transition from hadronic to partonic matter. This regime has been very little explored experimentally so far. The corresponding beam energy range (from  $\sim 10$ -45 AGeV) has only been partially covered in the past by pioneering experiments at the AGS in Brookhaven and, more recently, by experiments at CERN-SPS. A non-monotonous behavior was observed in the excitation function of several observables, such as the  $\langle K^+ \rangle / \langle \pi^+ \rangle$  ratio, at a beam energy of around 30 AGeV [286]. An interpretation of this intriguing finding as a signal for the onset of deconfinement is still under debate. A large low-mass dielectron enhancement was observed at 40 AGeV by the CERES experiment [287], corroborating the trend in the  $\langle K^+ \rangle / \langle \pi^+ \rangle$  excitation function. In fact, experimental limitations, both from the accelerators (beam intensities) and from the detectors (capabilities to measure rare signals) prevented comprehensive measurements to be performed at such low beam energies. Consequently, charm hadrons (and charmonia) have never been measured in this energy range. Such measurements could be especially interesting as this beam-energy range is close to the production threshold for  $c\bar{c}$  pairs. Therefore, the characteristics of the produced charm hadrons are expected to be particularly sensitive to the properties of the medium in the early stage of the collision. We further note that this region of the phase diagram is well suited for investigating properties of hadrons in a dense baryonic medium. This is based on the increasing gap between the putative phase boundary and the chemical freeze-out line when decreasing the beam energy from RHIC and top-SPS to FAIR. It furthermore suggests that at FAIR energies, contrary to RHIC and top-SPS, the produced system spends a relatively long time in a dense baryonic phase<sup>17</sup>.

### 4.3.1 Experimental conditions

The SIS-300 synchrotron at the FAIR facility will deliver heavy-ion beams from 10-35 AGeV for uranium and up to 45 AGeV for lighter ions with  $Z/A = 0.5$ . Proton beams will be available up to 90 GeV. Thanks to the unprecedented high beam intensities of  $2 \cdot 10^9$ /s, rare probes such as  $J/\psi$ , whose typical production rate is  $2 \cdot 10^{-5}$  per central Au-Au collision at 25 AGeV, will become available. Detection of such a small signal in such a high-intensity environment, and among about 1000 charged tracks per event, is highly challenging. It requires excellent detector performance in terms of radiation hardness, read-out speed, online-event selection, particle identification and data processing. The CBM detector is currently being designed to meet these requirements.

### 4.3.2 The CBM experiment

The CBM experiment is a next generation fixed-target universal detector capable of measuring hadronic, leptonic and photonic probes in a large geometrical acceptance with good vertexing. Its modular configuration (Fig. 50) will allow quarkonia measurements both in the electron and muon channels. Hadron-track reconstruction and momentum measurements will be performed by the Silicon Tracking System (STS) which consists of several stations of radiation hard silicon strips located inside the aperture of a 1 Tm bending dipole magnet. Displaced vertices will be measured with high precision by means of a Micro Vertex Detector (MVD) based on monolithic active pixel sensors operated in vacuum close to the target. Electrons will be identified by a combination of RICH and TRD detectors placed downstream. For muon measurements, the RICH detector will be replaced by an active absorber system (MUCH) made of sandwiches of detection planes and iron layers. The setup is completed by a RPC-based ToF system for charged-hadron measurements and by an EMC for neutral particle measurements.

Figure 51 shows the  $J/\psi$  signal extracted from  $4 \cdot 10^{10}$  central Au-Au collisions at 25 AGeV. The corresponding expected data taking time is 11 hours in the muon channel and 55 hours in the electron

---

<sup>17</sup>Note, however, that the uncertainty from IQCD calculations on the phase boundary is still large.

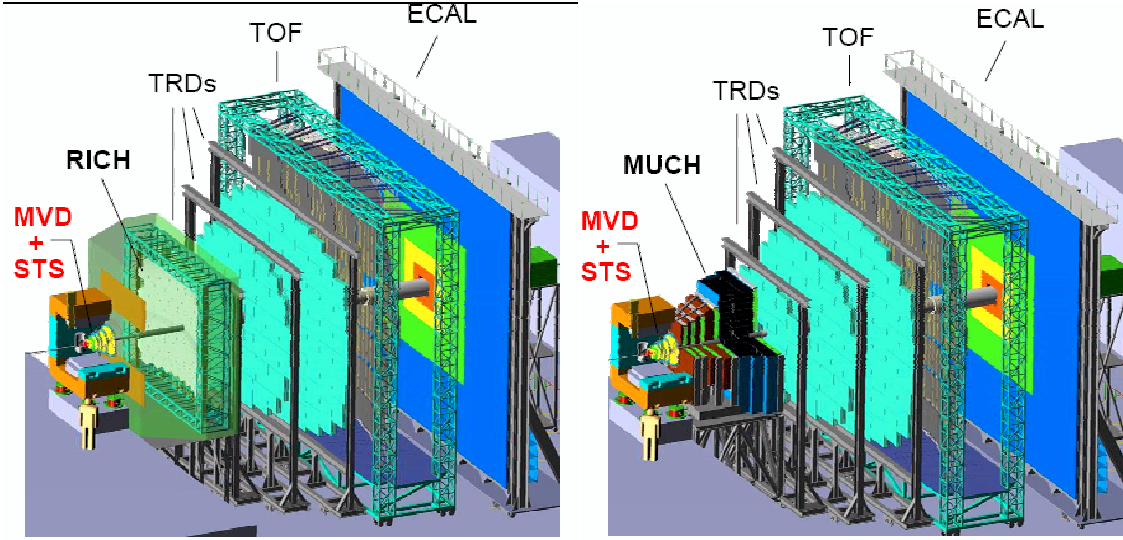


Figure 50: Longitudinal view of the CBM detector. Left: configuration for electron and hadron measurements. Right: configuration for muon measurements.

channel. The simulation assumes a  $\pi^\pm$  suppression of  $10^4$  from the RICH, TRD and ToF systems in the electron channel and a very good suppression of muons from  $\pi^\pm, K^\pm$  decay in the muon channel thanks to kink detection with the STS. The obtained reconstruction performance is comparable in both channels.

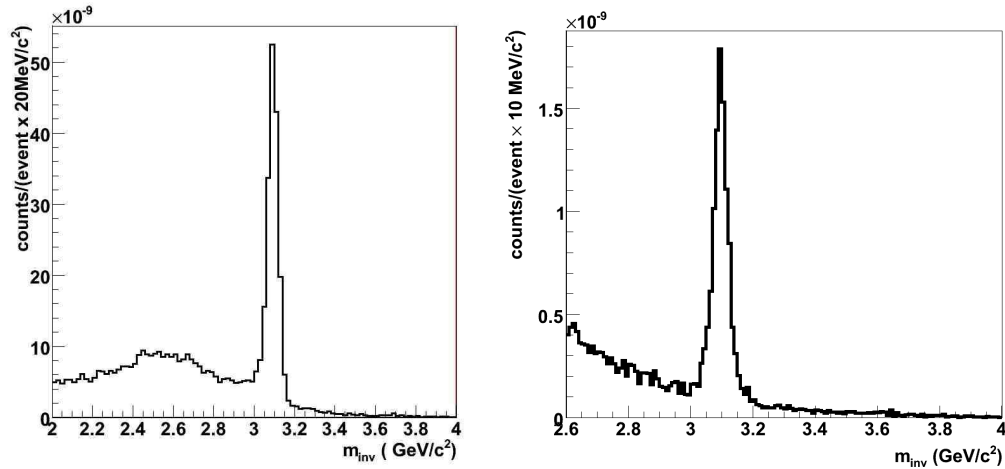


Figure 51: Invariant-mass spectrum showing  $J/\psi$  reconstruction in central Au-Au collisions at 25 AGeV with the CBM detector in the electron (left) and muon (right) channels [288].

## 5 Summary

The description of quarkonium production in ultrarelativistic heavy-ion collisions remains a challenging task, but new insights keep emerging on the three major frontiers, i.e., theoretical, phenomenological and experimental. In this review we have mostly focused on recent developments and have attempted to combine the current knowledge toward developing a consistent framework which can be checked against lattice QCD (lQCD) “data” and realistically applied to experimental data. In each of the following

paragraphs, we briefly summarize the main points for the three frontiers and subsequently identify directions of future work.

First principle IQCD computations of quarkonium correlation functions at finite temperature, now also available including dynamical light quarks, have consolidated the finding that ground-state charmonia (bottomonia) are little affected up to temperatures of  $\sim 2(3) T_c$ . This translates into the presence of bound (or resonance) states in the pertinent spectral functions when extracted from the correlators using probabilistic methods. On the other hand, IQCD computations of the free energy of a heavy-quark (HQ) pair in a Quark-Gluon Plasma (QGP) clearly exhibit the effect of color screening, increasing with temperature. When these free energies are injected as a potential into a Schrödinger equation, the  $J/\psi$  melts at significantly smaller temperatures than suggested by the correlators, slightly above  $T_c$ . Higher melting temperatures are obtained from potential models when employing the IQCD-based *internal* energies, which apparently agrees better with the spectral function results. However, in both cases, i.e. using free or internal energies, potential models are able to reproduce the approximate constancy of the correlation functions. This has recast some doubt on whether ground-state charmonia really survive well above  $T_c$ . One of the main reasons for this redundancy is that a reduced binding can be compensated by a reduced open-charm threshold, corresponding to a reduced thermal charm-quark mass - an effect which is well established for bound states in electromagnetic plasmas. Furthermore, nonperturbative rescattering effects typically lead to a large enhancement in the continuum part of the quarkonium spectral functions, especially close to the quark-antiquark threshold. Thus a reliable determination of the in-medium charm-quark mass, as well as of finite-width effects (for both charmonia and open-charm states), is needed to improve the evaluation of quarkonium spectral functions. In addition, it will be important to develop better criteria for the applicability of potential models at finite temperature, e.g., by setting up effective field theories if suitable scale separations can be applied.

In-medium binding energies turn out to play an important role in quarkonium dissociation reactions. For strong binding, leading-order gluo-dissociation is the most important process. For weakly bound quarkonia, next-to-leading order processes (“quasifree” destruction) become dominant, especially close to the “melting” temperatures; both thermal quarks and gluons contribute to these reactions. The pertinent inelastic widths of charmonia can reach up to several hundred MeV for temperatures as low as  $1.5 T_c$  (depending on the value of  $\alpha_s$ ), translating into lifetimes (well) below 1 fm/c. For phenomenology in heavy-ion collisions this implies that quarkonium dissociation will be operative well before the pertinent bound states dissolve due to color screening. It also reiterates that a consistent treatment of screening and finite-width effects is mandatory. Furthermore, the spectral properties of open heavy-flavor states are expected to change appreciably in the medium, with direct consequences for quarkonia: while effective HQ (or heavy-meson) masses determine the onset of the open heavy-flavor continuum, finite widths can open additional quarkonium decay channels even below threshold. Taking guidance from well-developed concepts in electromagnetic plasma physics, finite temperature  $T$ -matrix approaches seem to be a suitable tool to incorporate all of these aspects.

Equilibrium properties of quarkonia in medium (masses and widths) are key ingredients to transport theoretical evaluations of quarkonium observables in heavy-ion collisions, especially if carried out in a thermally evolving bulk medium (which appears to be a good approximation at SPS and RHIC). A quantitative understanding of cold-nuclear-matter effects on initial quarkonium spectra is mandatory to extract “anomalous” suppression in the subsequently formed hot and dense medium. Cold-nuclear-matter effects include modifications of the nuclear parton distribution functions (“shadowing”), initial-state energy loss, Cronin effect and nuclear absorption. Experimental evidence is mounting that the relative importance of these effects changes significantly with collision energy and rapidity, and thus empirical constraints from  $p$ - $A$  (or  $d$ - $A$ ) data are indispensable. In addition, secondary charmonium production (“regeneration”) via  $c$ - $\bar{c}$  coalescence (in the QGP or at hadronization) is expected to become increasingly relevant with increasing collision energy. This implies a coupling of charmonium yields and spectra to the abundance and spectra of open charm, which themselves are subject to medium

modifications. This further adds to the complexity of the calculations reinforcing the need of comprehensive analyses of open- and hidden-flavor observables in collision centrality, energy, system size and 3-momentum. The current state of phenomenology suggests that (a) the observed  $J/\psi$  suppression at the SPS mostly occurs in a hot/dense medium at energy densities above the critical one found in lQCD, with initial temperatures of  $T_0 \simeq 220\text{-}250$  MeV; (b) at RHIC energies, a significant regeneration component develops, accounting for roughly 50% of the measured  $J/\psi$  yield in central Au-Au; this assertion is corroborated by the observed narrowing in the rapidity distributions and an approximately constant average transverse momentum with centrality, with regeneration contributions prevalent at low  $p_T$ . If the regeneration yield becomes dominant at the LHC, a qualitatively new (increasing) centrality dependence of the nuclear modification factor may emerge (depending on the open-charm cross section). A more direct probe of color screening is provided by the  $\Upsilon$ : if it retains its vacuum binding energy up to  $\sim 2T_c$ , it will be rather inert under RHIC conditions; however, an in-medium reduction in its binding increases the dissociation rates noticeably which might suppress  $\Upsilon$  production as much as  $J/\psi$  production. Such a signal benefits from the absence of bottomonium regeneration at RHIC. A similar feature could be even more pronounced at the LHC, especially if regeneration of the  $J/\psi$  is large, while it is still expected to be small for  $\Upsilon$ . Transverse-momentum spectra will further illuminate the different mechanisms, and/or reveal new ones. E.g., first RHIC data for  $J/\psi$ 's at high  $p_T \geq 5$  GeV indicate a nuclear modification factor close to one, very different from light-hadron spectra. Elliptic flow could be another good discriminator between direct and secondary production, but only if the regeneration component in semi-central collision persists to sufficiently large  $p_T$ , above at least 2 GeV. Finally, excited  $\Psi$  and  $\Upsilon$  states are of great interest to test suppression patterns as regeneration contributions are usually suppressed due to their larger mass.

The quantitative realization of the above observables requires an advanced experimentation which will become available at RHIC-II and the LHC. While the former appears to operate at an energy suited to study the properties of a strongly coupled, liquid-like QGP, the latter may, for the first time, reach into a weakly coupled gas-like regime. At lower energies, the CBM experiment at FAIR will explore strongly interacting matter at maximum net baryon density; little (nothing) is known theoretically (experimentally) about charmonium properties under these conditions. In view of these developments, and with an adequate theoretical support, quarkonia promise to remain a rich, and eventually quantitative, probe of high-energy density matter in heavy-ion collisions.

## Acknowledgment

We are indebted to our colleagues A. Beraudo for a careful reading of sections 2 and 3, to M. Laine and G. Röpke for valuable comments on section 2, to J.-P. Lansberg for useful comments on section 3.2, and to A. Andronic, R. Averbeck and P. Senger for useful comments on section 4. The work of RR has been supported by the U.S. National Science Foundation (NSF) with a CAREER award under grant no. PHY-0449489, by NSF grant no. PHY-0969394, and by a Bessel Research Award from the A.-v.-Humboldt foundation. The work of DB has been supported in part by the Polish Ministry for Science and Higher Education under grant No. N N 202 0953 33 and by RFBR grant No. 08-02-01003-a.

## References

- [1] T. Matsui and H. Satz, Phys. Lett. B **178** (1986) 416.
- [2] C. Gerschel and J. Hüfner, Ann. Rev. Nucl. Part. Sci. **49** (1999) 255.
- [3] R. Vogt, Phys. Rept. **310** (1999) 197.
- [4] H. Satz, J. Phys. G **32** (2006) R25.
- [5] D. E. Kharzeev, J. Phys. G **34** (2007) S445.

- [6] L. Kluberg, Eur. Phys. J. C **43** (2005) 145.
- [7] C. Amsler *et al.* [Particle Data Group], Phys. Lett. B **667** (2008) 1.
- [8] E. Eichten, K. Gottfried, T. Kinoshita, K. D. Lane and T. M. Yan, Phys. Rev. D **21** (1980) 203.
- [9] N. Brambilla *et al.*, CERN Yellow Rep. 2005-005, [arXiv:hep-ph/0412158].
- [10] G. S. Bali, Phys. Rept. **343** (2001) 1.
- [11] O. Kaczmarek and F. Zantow, Phys. Rev. D **71** (2005) 114510.
- [12] S. S. Adler *et al.* [PHENIX Collaboration], Phys. Rev. Lett. **94** (2005) 082301.
- [13] R. Shahoyan [NA60 Collaboration], J. Phys. G **34** (2007) S1029.
- [14] P. Levai, B. Müller and X.-N. Wang, Phys. Rev. C **51** (1995) 3326.
- [15] E. V. Shuryak, Phys. Lett. B **78** (1978) 150 [Sov. J. Nucl. Phys. **28** (1978) 408 / YAFIA 28 (1978) 796].
- [16] J. Cleymans and C. Vanderzande, Phys. Lett. B **147** (1984) 186.
- [17] N. F. Mott, Rev. Mod. Phys. **40**, 677 (1968).
- [18] R. Redmer, Phys. Rep. **282** (1997) 35.
- [19] C. Baglin *et al.* [NA38 Collaboration], Phys. Lett. B **220** (1989) 471.
- [20] C. Gerschel and J. Hüfner, Phys. Lett. B **207** (1988) 253.
- [21] S. Gavin, M. Gyulassy and A. Jackson, Phys. Lett. B **207** (1988) 257.
- [22] R. Vogt, M. Prakash, P. Koch and T. H. Hansson, Phys. Lett. B **207** (1988) 263.
- [23] J. Badier *et al.* [NA3 Collaboration], Z. Phys. C **20** (1983) 101.
- [24] M. C. Abreu *et al.* [NA38 Collaboration], Phys. Lett. B **444** (1998) 516.
- [25] D. M. Alde *et al.*, Phys. Rev. Lett. **66** (1991) 133.
- [26] C. Baglin *et al.*, Phys. Lett. B **270** (1991) 105.
- [27] C. Gerschel and J. Hüfner, Z. Phys. C **56** (1992) 171.
- [28] M. Gonin *et al.* [NA50 Collaboration], Nucl. Phys. A **610** (1996) 404c.
- [29] M. C. Abreu *et al.* [NA50 Collaboration], Phys. Lett. B **410** (1997) 337.
- [30] J. P. Blaizot and J. Y. Ollitrault, Phys. Rev. Lett. **77** (1996) 1703.
- [31] D. Kharzeev, C. Lourenco, M. Nardi and H. Satz, Z. Phys. C **74** (1997) 307.
- [32] B. Alessandro *et al.* [NA50 Collaboration], Eur. Phys. J. C **39** (2005) 335.
- [33] R. Arnaldi *et al.* [NA60 Collaboration], Nucl. Phys. A **774** (2006) 711.
- [34] R. Arnaldi *et al.* [NA60 Collaboration], Nucl. Phys. A **783** (2007) 261.
- [35] M.C. Abreu *et al.* [NA50 Collaboration], Phys. Lett. B **477** (2000) 28.
- [36] S.S. Adler *et al.* [PHENIX Collaboration], Phys. Rev. C **69** (2004) 014901.
- [37] A. Adare *et al.* [PHENIX Collaboration], Phys. Rev. Lett. **98** (2007) 232301.
- [38] L. Grandchamp, R. Rapp and G. E. Brown, Phys. Rev. Lett. **92** (2004) 212301.
- [39] R. L. Thews, Eur. Phys. J. C **43** (2005) 97.
- [40] M. J. Leitch, AIP Conf. Proc. **892** (2007) 404.
- [41] P. Braun-Munzinger and J. Stachel, Phys. Lett. B **490** (2000) 196.

- [42] R. L. Thews, M. Schroedter and J. Rafelski, Phys. Rev. C **63** (2001) 054905.
- [43] M. I. Gorenstein, A. P. Kostyuk, H. Stöcker and W. Greiner, Phys. Lett. B **509** (2001) 277.
- [44] L. Grandchamp and R. Rapp, Phys. Lett. B **523** (2001) 60.
- [45] C. E. DeTar and J. B. Kogut, Phys. Rev. D **36** (1987) 2828.
- [46] K. D. Born, S. Gupta, A. Irbäck, F. Karsch, E. Laermann, B. Petersson and H. Satz [MT(c) Collaboration], Phys. Rev. Lett. **67** (1991) 302.
- [47] M. Asakawa, T. Hatsuda and Y. Nakahara, Prog. Part. Nucl. Phys. **46** (2001) 459.
- [48] M. Asakawa and T. Hatsuda, Phys. Rev. Lett. **92** (2004) 012001.
- [49] S. Datta, F. Karsch, P. Petreczky and I. Wetzorke, Phys. Rev. D **69** (2004) 094507.
- [50] R. Morrin, A. P. O Cais, M. B. Oktay, M. J. Peardon, J. I. Skullerud, G. Aarts and C. R. Allton, PoS **LAT2005** (2006) 176.
- [51] A. Jakovac, P. Petreczky, K. Petrov and A. Velytsky, Phys. Rev. D **75** (2007) 014506.
- [52] G. Aarts, C. Allton, M. B. Oktay, M. Peardon and J. I. Skullerud, Phys. Rev. D **76** (2007) 094513; M. B. Oktay, M. J. Peardon, J. I. Skullerud, G. Aarts and C. R. Allton, PoS LAT2007 (2007) 227.
- [53] K. Petrov, A. Jakovac, P. Petreczky and A. Velytsky, PoS **LAT2005** (2006) 153.
- [54] L. D. McLerran and B. Svetitsky, Phys. Lett. B **98** (1981) 195.
- [55] O. Philipsen, Nucl. Phys. A **820** (2009) 33C.
- [56] O. Kaczmarek, F. Karsch, P. Petreczky and F. Zantow, Phys. Lett. B **543** (2002) 41.
- [57] P. Petreczky and K. Petrov, Phys. Rev. D **70** (2004) 054503.
- [58] M. A. Escobedo and J. Soto, arXiv:0804.0691 [hep-ph].
- [59] N. Brambilla, J. Ghiglieri, A. Vairo and P. Petreczky, Phys. Rev. D **78** (2008) 014017.
- [60] F. Karsch, M.T. Mehr and H. Satz, Z. Phys. C **37** (1988) 617.
- [61] O. Kaczmarek, F. Karsch, F. Zantow and P. Petreczky, Phys. Rev. D **70** (2004) 074505 [Erratum-ibid. D **72** (2005) 059903].
- [62] S. Digal, P. Petreczky and H. Satz, Phys. Rev. D **64** (2001) 094015.
- [63] E.V. Shuryak and I. Zahed, Phys. Rev. D **70** (2004) 054507.
- [64] C.Y. Wong, Phys. Rev. C **72** (2005) 034906.
- [65] W.M. Alberico, A. Beraudo, A. De Pace and A. Molinari, Phys. Rev. D **72** (2005) 114011.
- [66] M. Mannarelli and R. Rapp, Phys. Rev. C **72** (2005) 064905.
- [67] H. Satz, J. Phys. G **36** (2009) 064011.
- [68] R. Rapp, Eur. Phys. J A **18** (2003) 459.
- [69] A. Mocsy and P. Petreczky, Phys. Rev. D **73** (2006) 074007.
- [70] W.M. Alberico, A. Beraudo, A. De Pace and A. Molinari, Phys. Rev. D **75** (2007) 074009.
- [71] D. Cabrera and R. Rapp, Phys. Rev. D **76** (2007) 114506.
- [72] W. Ebeling, W.-D. Kraeft, D. Kremp, G. Röpke, *Quantum Statistics of Charged Many-Particle Systems*, Plenum, New York (1986).
- [73] R. Machleidt, Adv. Nucl. Phys. **19** (1989) 189.
- [74] O. Kaczmarek and F. Zantow, arXiv:hep-lat/0506019.

- [75] R. Rapp, D. Cabrera, V. Greco, M. Mannarelli and H. van Hees, arXiv:0806.3341 [hep-ph].
- [76] T. Umeda, Phys. Rev. D **75** (2007) 094502.
- [77] P. Petreczky and D. Teaney, Phys. Rev. D **73** (2006) 014508.
- [78] A. Mocsy and P. Petreczky, Phys. Rev. Lett. **99** (2007) 211602; Phys. Rev. D **77** (2008) 014501.
- [79] W.M. Alberico, A. Beraudo, A. De Pace and A. Molinari, Phys. Rev. D **77** (2008) 017502.
- [80] S. Datta, A. Jakovac, F. Karsch and P. Petreczky, AIP Conf. Proc. **842** (2006) 35.
- [81] M. Laine, O. Philipsen, P. Romatschke and M. Tassler, JHEP **0703** (2007) 054.
- [82] A. Beraudo, J.P. Blaizot and C. Ratti, Nucl. Phys. A **806** (2008) 312.
- [83] M. Laine, O. Philipsen and M. Tassler, JHEP **0709** (2007) 066.
- [84] M. Laine, JHEP **0705** (2007) 028.
- [85] Y. Burnier, M. Laine and M. Vepsalainen, JHEP **0801** (2008) 043.
- [86] P. Petreczky, Eur. Phys. J. C **62** (2009) 85.
- [87] C. Y. Wong and H. W. Crater, Phys. Rev. D **75** (2007) 034505.
- [88] G. Bhanot and M. E. Peskin, Nucl. Phys. B **156** (1979) 391.
- [89] M. E. Peskin, Nucl. Phys. B **156** (1979) 365.
- [90] F. Arleo, J. Cugnon and Y. Kalinovsky, Phys. Lett. B **614** (2005) 44.
- [91] D. Blaschke, Y. Kalinovsky and V. Yudichev, Lect. Notes Phys. **647** (2004) 366.
- [92] L. Grandchamp and R. Rapp, Nucl. Phys. A **709** (2002) 415.
- [93] G. Röpke, D. Blaschke and H. Schulz, Phys. Rev. D **38** (1988) 3589.
- [94] D. Kharzeev, L. D. McLerran and H. Satz, Phys. Lett. B **356** (1995) 349.
- [95] Y. Park, K.I. Kim, T. Song, S.H. Lee and C.Y. Wong, Phys. Rev. C **76** (2007) 044907.
- [96] T. Song, Y. Park, S.H. Lee and C.Y. Wong, Phys. Lett. B **659** (2008) 621.
- [97] X. Zhao and R. Rapp, Phys. Lett. B **664** (2008) 253.
- [98] B. L. Combridge, Nucl. Phys. B **151** (1979) 429.
- [99] L. Grandchamp, S. Lumpkins, D. Sun, H. van Hees and R. Rapp, Phys. Rev. C **73** (2006) 064906.
- [100] A. Dumitru, Y. Guo and M. Strickland, Phys. Lett. B **662**, 37 (2008)
- [101] Y. Burnier, M. Laine and M. Vepsalainen, Phys. Lett. B **678**, 86 (2009)
- [102] O. Philipsen and M. Tassler, arXiv:0908.1746 [hep-ph].
- [103] F. Riek and R. Rapp, arXiv:1005.0769 [hep-ph].
- [104] K. Morita and S. H. Lee, Phys. Rev. C **77**, 064904 (2008) [arXiv:0711.3998 [hep-ph]].
- [105] D. Blaschke, G. Burau, Yu. Kalinovsky and T. Barnes, Eur. Phys. J. A **18** (2003) 547.
- [106] T. Barnes, E.S. Swanson, C.Y. Wong and X.M. Xu, Phys. Rev. C **68** (2003) 014903.
- [107] M. A. Ivanov, J. G. Körner and P. Santorelli, Phys. Rev. D **70** (2004) 014005.
- [108] A. Bourque, C. Gale and K.L. Haglin, Phys. Rev. C **70** (2004) 055203.
- [109] A. Bourque and C. Gale, Phys. Rev. C **78** (2008) 035206. [arXiv:0802.2738 [hep-ph]].
- [110] Y. Oh, W. Liu and C.M. Ko, Phys. Rev. C **75** (2007) 064903. [arXiv:nucl-th/0702077].

- [111] F.S. Navarra, M. Nielsen and M. R. Robilotta, Phys. Rev. C **64** (2001) 021901. [arXiv:nucl-th/0103051].
- [112] A. Bourque and C. Gale, Phys. Rev. C **80** (2009) 015204.
- [113] S. G. Matinyan and B. Müller, Phys. Rev. C **58** (1998) 2994.
- [114] K.L. Haglin, Phys. Rev. C **61** (2000) 031902. [arXiv:nucl-th/9907034].
- [115] T. Song and S. H. Lee, Phys. Rev. D **72** (2005) 034002.
- [116] C.Y. Wong, E.S. Swanson and T. Barnes, Phys. Rev. C **62** (2000) 045201.
- [117] K. Martins, D. Blaschke and E. Quack, Phys. Rev. C **51** (1995) 2723.
- [118] J.P. Hilbert, N. Black, T. Barnes and E.S. Swanson, Phys. Rev. C **75** (2007) 064907
- [119] D. Prorok, L. Turko and D. Blaschke, AIP Conf. Proc. **1038** (2008) 73.
- [120] D. B. Blaschke, G. R. G. Burau, M. A. Ivanov, Yu. L. Kalinovsky and P. C. Tandy, arXiv:hep-ph/0002047.
- [121] D.B. Blaschke, H. Grigorian and Yu.L. Kalinovsky, arXiv:0808.1705 [hep-ph].
- [122] A. Sibirtsev, K. Tsushima and A.W. Thomas, Phys. Rev. C **63** (2001) 044906.
- [123] A. Sibirtsev, K. Tsushima, K. Saito and A. W. Thomas, Phys. Lett. B **484** (2000) 23.
- [124] K. Tsushima, A. Sibirtsev, K. Saito, A. W. Thomas and D. H. Lu, Nucl. Phys. A **680** (2001) 280.
- [125] G.R.G. Burau, D.B. Blaschke and Y.L. Kalinovsky, Phys. Lett. B **506** (2001) 297.
- [126] B. Friman, S. H. Lee and T. Song, Phys. Lett. B **548** (2002) 153.
- [127] D. Blaschke, G. Burau, Yu. Kalinovsky, V. Yudichev, Prog. Theor. Phys. Suppl. **149** (2003) 182.
- [128] C. Fuchs, B.V. Martemyanov, A. Faessler and M.I. Krivoruchenko, Phys. Rev. C **73** (2006) 035204.
- [129] D. Blaschke, G. Burau and Yu.L. Kalinovsky, arXiv:nucl-th/0006071.
- [130] M. Schlages, Th. Bornath and D. Kremp, Phys. Rev. A **38** (1988) 2174.
- [131] R. Zimmermann, K. Kilimann, W. D. Kraeft, D. Kremp and G. Röpke, Phys. Stat. Sol. (b) **90** (1978) 175.
- [132] G. Röpke *et al.*, Nucl. Phys. A **379** (1982) 536.
- [133] G. Röpke *et al.*, Nucl. Phys. A **399** (1983) 587.
- [134] C. J. Horowitz, E. J. Moniz and J. W. Negele, Phys. Rev. D **31** (1985) 1689.
- [135] G. Röpke, D. Blaschke and H. Schulz, Phys. Rev. D **34** (1986) 3499.
- [136] G. Baym, Phys. Rev. **127** (1962) 1391.
- [137] W. Ebeling and K. Kilimann, Z. Naturforsch. **44a** (1989) 519.
- [138] F. J. Rogers, H. C. Garboske Jr., and D. J. Harwood, Phys. Rev. A **1** (1970) 1577.
- [139] W. D. Kraeft, D. Kremp, K. Kilimann, and H. E. DeWitt, Phys. Rev. A **42** (1990) 2340.
- [140] G. W. Fehrenbach, W. Schäfer, J. Treusch, and R. G. Ulbrich, Phys. Rev. Lett. **49** (1981) 1281.
- [141] G. Ecker and W. Weitzel, Ann. Phys. (Lpz.) **17** (1956) 126.
- [142] V. V. Dixit, Mod. Phys. Lett. A **5** (1990) 227.
- [143] C. Ratti, M. A. Thaler and W. Weise, Phys. Rev. D **73** 014019 (2006).
- [144] H. Hansen *et al.*, Phys. Rev. D **75** 065004 (2007).

- [145] J. Jankowski, D. Blaschke and H. Grigorian, arXiv:0911.1534 [hep-ph].
- [146] G. Röpke and R. Der, Phys. stat. sol. (b) **92** (1979) 501.
- [147] G. Röpke *et al.*, Nucl. Phys. A **424** (1984) 594.
- [148] D. Kharzeev and H. Satz, Phys. Lett. B **334** (1994) 155.
- [149] F. Arleo, P.B. Gossiaux, T. Gousset and J. Aichelin, Phys. Rev. D **65** (2002) 014005.
- [150] D. Blaschke and V. L. Yudichev, AIP Conf. Proc. **842** (2006) 38.
- [151] H. Satz, arXiv:hep-ph/0602245.
- [152] H. Miyazawa, Phys. Rev. D **20** (1979) 2953.
- [153] D. Blaschke, F. Reinholz, G. Röpke and D. Kremp, Phys. Lett. B **151** (1985) 439.
- [154] G. Röpke, D. Blaschke and H. Schulz, Phys. Lett. B **202** (1988) 479.
- [155] A. Capella, E. G. Ferreira and A. B. Kaidalov, Phys. Rev. Lett. **85** (2000) 2080.
- [156] W. Cassing and C. M. Ko, Phys. Lett. B **396** (1997) 39.
- [157] C. Spieles *et al.*, Phys. Lett. B **458** (1999) 137.
- [158] A.K. Chaudhuri, Phys. Rev. C **68** (2003) 037901.
- [159] C. M. Ko, B. Zhang, X. N. Wang and X. F. Zhang, Phys. Lett. B **444** (1998) 237.
- [160] P. Braun-Munzinger and K. Redlich, Eur. Phys. J. C **16** (2000) 519.
- [161] M. Gazdzicki and M. I. Gorenstein, Phys. Rev. Lett. **83** (1999) 4009.
- [162] A. Andronic, P. Braun-Munzinger, K. Redlich and J. Stachel, Nucl. Phys. A **789** (2007) 334.
- [163] H. van Hees, M. Mannarelli, V. Greco and R. Rapp, Phys. Rev. Lett. **100** (2008) 192301.
- [164] V. Greco, C. M. Ko and R. Rapp, Phys. Lett. B **595** (2004) 202.
- [165] L. Yan, P. Zhuang and N. Xu, Phys. Rev. Lett. **97** (2006) 232301.
- [166] J. Rafelski, J. Letessier and A. Tounsi, Acta Phys. Polon. B **27** (1996) 1037.
- [167] K. A. Bugaev, M. Gazdzicki and M. I. Gorenstein, Phys. Lett. B **523** (2001) 255.
- [168] R. L. Thews and M. L. Mangano, Phys. Rev. C **73** (2006) 014904.
- [169] A. Adare *et al.* [PHENIX Collaboration], Phys. Rev. Lett. **97** (2006) 252002.
- [170] C. Zhong [STAR Collaboration], J. Phys. G **34** (2007) S741.
- [171] S. Frixione, M. L. Mangano, P. Nason and G. Ridolfi, Adv. Ser. Direct. High Energy Phys. **15** (1998) 609.
- [172] C. Lourenco and H. K. Wöhri, Phys. Rept. **433** (2006) 127.
- [173] R. Rapp and L. Grandchamp, J. Phys. G **30** (2004) S305.
- [174] A. Andronic, P. Braun-Munzinger, K. Redlich and J. Stachel, Phys. Lett. B **659** (2008) 149.
- [175] V. Greco, H. van Hees and R. Rapp, arXiv:0709.4452 [hep-ph].
- [176] P. B. Gossiaux, V. Guiho and J. Aichelin, J. Phys. G **31** (2005) S1079.
- [177] F. Karsch and R. Petronzio, Phys. Lett. B **193** (1987) 105.
- [178] J. P. Blaizot and J. Y. Ollitrault, Phys. Lett. B **199** (1987) 499.
- [179] M. C. Chu and T. Matsui, Phys. Rev. D **37** (1988) 1851.
- [180] F. Karsch and H. Satz, Z. Phys. C **51** (1991) 209.

- [181] J. Cugnon and P. B. Gossiaux, Phys. Lett. B **359** (1995) 375.
- [182] B. Zhang, C. M. Ko, B. A. Li, Z. W. Lin and S. Pal, Phys. Rev. C **65** (2002) 054909.
- [183] O. Linnyk, E. L. Bratkovskaya, W. Cassing and H. Stöcker, Nucl. Phys. A **786** (2007) 183.
- [184] O. Linnyk, E. L. Bratkovskaya, W. Cassing and H. Stöcker, Phys. Rev. C **76** (2007) 041901.
- [185] E. L. Bratkovskaya, W. Cassing and H. Stöcker, Phys. Rev. C **67** (2003) 054905.
- [186] A. Capella, L. Bravina, E. G. Ferreira, A. B. Kaidalov, K. Tywoniuk and E. Zabrodin, Eur. Phys. J. C **58** (2008) 437.
- [187] B. Alessandro *et al.* [NA50 Collaboration], Eur. Phys. J. C **33** (2004) 31.
- [188] R. Arnaldi *et al.* [NA60 Collaboration], arXiv:1004.5523 [nucl-ex].
- [189] C. Lourenco, Nucl. Phys. A **783** (2007) 451.
- [190] Y. B. He, J. Hüfner and B. Z. Kopeliovich, Phys. Lett. B **477** (2000) 93.
- [191] J. Hüfner and B. Z. Kopeliovich, Phys. Lett. B **426** (1998) 154.
- [192] T. Matsui, Annals Phys. **196** (1989) 182.
- [193] J. Cugnon and P. B. Gossiaux, Z. Phys. C **58** (1993) 77.
- [194] J. Cugnon and P. B. Gossiaux, Z. Phys. C **58** (1993) 95.
- [195] D. Koudela and C. Volpe, Phys. Rev. C **69** (2004) 054904.
- [196] J. P. Blaizot and J. Y. Ollitrault, Phys. Lett. B **217** (1989) 386.
- [197] S. Gavin, R. Vogt, Nucl. Phys. B **345** (1990) 104.
- [198] F. Arleo, P. B. Gossiaux, T. Gousset and J. Aichelin, Phys. Rev. C **61** (2000) 054906.
- [199] F. Arleo, P. B. Gossiaux and J. Aichelin, Phys. Rev. C **65** (2002) 054911.
- [200] M. J. Leitch *et al.* [FNAL E866/NuSea collaboration], Phys. Rev. Lett. **84** (2000) 3256.
- [201] P. Faccioli [HERA-B Collaboration], AIP Conf. Proc. **814** (2006) 545.
- [202] L. Ramello [NA50 Collaboration], Nucl. Phys. A **774** (2006) 59.
- [203] K. J. Eskola, V. J. Kolhinen and C. A. Salgado, Eur. Phys. J. C **9** (1999) 61.
- [204] K. J. Eskola, V. J. Kolhinen and R. Vogt, Nucl. Phys. A **696** (2001) 729.
- [205] A. Accardi *et al.*, arXiv:hep-ph/0308248.
- [206] D. de Florian and R. Sassot, Phys. Rev. D **69** (2004) 074028.
- [207] A. Adare *et al.* [PHENIX Collaboration], Phys. Rev. C **77** (2008) 024912.
- [208] F. Arleo and V. N. Tram, Eur. Phys. J. C **55** (2008) 449.
- [209] K. J. Eskola, H. Paukkunen and C. A. Salgado, JHEP **0807** (2008) 102.
- [210] I. Arsene *et al.* [BRAHMS Collaboration], Phys. Rev. Lett. **93** (2004) 242303.
- [211] F. Arleo, Phys. Lett. B **666** (2008) 31.
- [212] I. Vitev, Phys. Lett. B **562** (2003) 36.
- [213] H. Habermann and J. P. Lansberg, Phys. Rev. Lett. **100** (2008) 032006.
- [214] P. Artoisenet and E. Braaten, Phys. Rev. D **80**, 034018 (2009).
- [215] S. J. Brodsky and J. P. Lansberg, Phys. Rev. D **81**, 051502 (2010).
- [216] J. P. Lansberg, arXiv:1003.4319 [hep-ph].

- [217] V. A. Khoze, A. D. Martin, M. G. Ryskin and W. J. Stirling, Eur. Phys. J. C **39**, 163 (2005).
- [218] E. G. Ferreira, F. Fleuret, J. P. Lansberg and A. Rakotozafindrabe, Phys. Lett. B **680** (2009) 50.
- [219] S. J. Brodsky and A. H. Mueller, Phys. Lett. B **206** (1988) 685.
- [220] B. Z. Kopeliovich and B. G. Zakharov, Phys. Rev. D **44** (1991) 3466.
- [221] D. Blaschke and J. Hüfner, Phys. Lett. B **281** (1992) 364.
- [222] B.Z. Kopeliovich and J. Raufeisen, Lect. Notes Phys. **647** (2004) 305.
- [223] I. Abt *et al.* [HERA-B Collaboration], Phys. Lett. B **561** (2003) 61.
- [224] I. Abt *et al.* [HERA-B Collaboration], Eur. Phys. J. C **49** (2007) 545.
- [225] M.J. Leitch [PHENIX Collaboration], arXiv:0806.1244 [nucl-ex].
- [226] D. E. Acosta *et al.* [CDF Collaboration], Phys. Rev. D **71** (2005) 032001.
- [227] X. l. Zhu, P. f. Zhuang and N. Xu, Phys. Lett. B **607** (2005) 107.
- [228] F. Karsch, PoS **LAT2007** (2007) 015.
- [229] C. Spieles, R. Vogt, L. Gerland, S. A. Bass, M. Bleicher, H. Stöcker and W. Greiner, Phys. Rev. C **60** (1999) 054901.
- [230] R. Arnaldi *et al.* [NA60 Collaboration], Phys. Rev. Lett. **99** (2007) 132302.
- [231] S. Digal, S. Fortunato and H. Satz, Eur. Phys. J. C **32** (2004) 547.
- [232] R. Rapp, Eur. Phys. J. C **43** (2005) 91.
- [233] A. Capella and E. G. Ferreira, Eur. Phys. J. C **42** (2005) 419.
- [234] R. Arnaldi *et al.* [NA60 Collaboration], J. Phys. G **32** (2006) S51.
- [235] C. Lourenco *et al.* [NA60 Collaboration], PoS **HEP2005** (2006) 133.
- [236] H. Pereira Da Costa [PHENIX Collaboration], Nucl. Phys. A **774** (2006) 747.
- [237] T. Gunji, H. Hamagaki, T. Hatsuda and T. Hirano, Phys. Rev. C **76** (2007) 051901.
- [238] X. Zhao and R. Rapp, in preparation (2010).
- [239] C. Young and E. Shuryak, Phys. Rev. C **79** (2009) 034907.
- [240] P. F. Zhuang and X. L. Zhu, Phys. Rev. C **67** (2003) 067901.
- [241] J. P. Blaizot, J. Y. Ollitrault, Phys. Rev. D **39** (1989) 232.
- [242] L. Gerland, L. Frankfurt, M. Strikman, H. Stöcker and W. Greiner, Phys. Rev. Lett. **81**, 762 (1998)
- [243] J. P. Blaizot and J. Y. Ollitrault, Phys. Lett. B **217** (1989) 392.
- [244] J. Hüfner, Y. Kurihara and H. J. Pirner, Phys. Lett. B **215** (1988) 218. [Acta Phys. Slov. **39** (1989) 281].
- [245] S. Gavin and M. Gyulassy, Phys. Lett. B **214** (1988) 241.
- [246] M. C. Abreu *et al.* [NA50 Collaboration], Phys. Lett. B **499** (2001) 85.
- [247] M. I. Gorenstein, K. A. Bugaev and M. Gazdzicki, Phys. Rev. Lett. **88** (2002) 132301.
- [248] D. Pal, B. K. Patra and D. K. Srivastava, Eur. Phys. J. C **17** (2000) 179.
- [249] Z. Tang [STAR Collaboration], Proc. of 24. Winter Workshop on Nuclear Dynamics, South Padre Island (TX, USA), April 05-12, 2008; arXiv:0804.4846 [nucl-ex].

- [250] X. Zhao and R. Rapp, Proc. of 24. Winter Workshop on Nuclear Dynamics, South Padre Island (TX, USA), April 05-12, 2008; arXiv:0806.1239 [nucl-th].
- [251] X. N. Wang and F. Yuan, Phys. Lett. B **540** (2002) 62.
- [252] Z. W. Lin and D. Molnar, Phys. Rev. C **68** (2003) 044901.
- [253] H. van Hees, V. Greco and R. Rapp, Phys. Rev. C **73** (2006) 034913.
- [254] A. Adare *et al.* [PHENIX Collaboration], Phys. Rev. Lett. **98** (2007) 172301.
- [255] L. Ravagli and R. Rapp, Phys. Lett. B **655** (2007) 126; L. Ravagli, H. van Hees and R. Rapp, Phys. Rev. C **79** (2009) 064902.
- [256] X. Zhao and R. Rapp, Eur. Phys. J. C **62** (2009) 109.
- [257] A. Frawley, talk at int. workshop on “Heavy Quarkonia Production in Heavy-Ion Collisions, ECT\* (Trento, Italy), May 25-29, 2009; and in preparation.
- [258] M. Cacciari, P. Nason and R. Vogt, Phys. Rev. Lett. **95** (2005) 122001.
- [259] A. Adare *et al.* [PHENIX Collaboration], Phys. Rev. Lett. **98** (2007) 232002.
- [260] F. Karsch, D. Kharzeev and H. Satz, Phys. Lett. B **637** (2006) 75.
- [261] M.C. Abreu *et al.* [NA50 Collaboration], Nucl. Phys. A **638** (1998) 261.
- [262] H. Sorge, E. V. Shuryak and I. Zahed, Phys. Rev. Lett. **79** (1997) 2775.
- [263] O. Linnyk, E. L. Bratkovskaya and W. Cassing, Nucl. Phys. A **807** (2008) 79.
- [264] Y. Morino [PHENIX Collaboration], J. Phys. G **35** (2008) 104116.
- [265] M. R. Cosentino [STAR Collaboration], arXiv:0806.0353 [nucl-ex].
- [266] J. F. Gunion and R. Vogt, Nucl. Phys. B **492** (1997) 301.
- [267] A. A. Affolder *et al.* [CDF Collaboration], Phys. Rev. Lett. **84** (2000) 2094.
- [268] A. D. Frawley, T. Ullrich and R. Vogt, Phys. Rept. **462** (2008) 125.
- [269] F. Carminati *et al.* [ALICE Collaboration], J. Phys. G **30** (2004) 1517.
- [270] B. Alessandro *et al.* [ALICE Collaboration], J. Phys. G **32** (2006) 1295.
- [271] D. G. d’Enterria *et al.*, J. Phys. G **34** (2007) 2307.
- [272] ATLAS Collaboration, CERN/LHCC/**2004–009**.
- [273] CBM Collaboration, Technical Status Report (2005), <http://www.gsi.de/fair/experiments/CBM/>
- [274] T.D. Lee, Nucl. Phys. A **750** (2005) 1; T. Ludlam, Nucl. Phys. A **750** (2005) 9; M. Gyulassy and L. McLerran, Nucl. Phys. A **750** (2005) 30; E. Shuryak, Nucl. Phys. A **750** (2005) 64; B. Müller, Nucl. Phys. A **750** (2005) 84; X.-N. Wang, Nucl. Phys. A **750** (2005) 98; H. Stöcker, Nucl. Phys. A **750** (2005) 121; J.-P. Blaizot and F. Gelis, Nucl. Phys. A **750** (2005) 148.
- [275] I. Arsene *et al.* (BRAHMS Collaboration), Nucl. Phys. A **757** (2005) 1; R.R. Betts *et al.* (PHOBOS Collaboration), Nucl. Phys. A **757** (2005) 28; J. Adams *et al.* (STAR Collaboration), Nucl. Phys. A **757** (2005) 102; K. Adcox *et al.* (PHENIX Collaboration), Nucl. Phys. A **757** (2005) 184.
- [276] B. L. Ioffe and D. E. Kharzeev, Phys. Rev. C **68** (2003) 061902.
- [277] J. Schukraft, Nucl. Phys. A **698** (2002) 287.
- [278] D. Kharzeev, E. Levin and M. Nardi, Nucl. Phys. A **747** (2005) 609
- [279] M. Bedjidian *et al.*, arXiv:hep-ph/0311048.
- [280] N. Armesto *et al.*, J. Phys. G **35** (2008) 054001.

- [281] X.M. Xu, D. Kharzeev, H. Satz and X.N. Wang, Phys. Rev. C **53** (1996) 3051.
- [282] P. Braun-Munzinger and J. Stachel, Phys. Lett. B **490** (2000) 196.
- [283] A. Andronic, P. Braun-Munzinger, K. Redlich and J. Stachel, Phys. Lett. B **652** (2007) 259.
- [284] W. M. Yao *et al.* [Particle Data Group], J. Phys. G **33** (2006) 1.
- [285] I. P. Lokhtin and A. M. Snigirev, Eur. Phys. J. C **21** (2001) 155.
- [286] C. Alt *et al.* [NA49 Collaboration], Phys. Rev. C **77** (2008) 024903.
- [287] D. Adamova *et al.* [CERES/NA45 Collaboration], Phys. Rev. Lett. **91** (2003) 042301.
- [288] C. Höhne for the CBM Collaboration, Int. Journ. of Mod. Phys. E **16** (2008) 2419.